ISSN 0974-1267 (Online)
ISSN 0972-4257 (Print)

Journal of METALLURGY AND MATERIALS SCIENCE

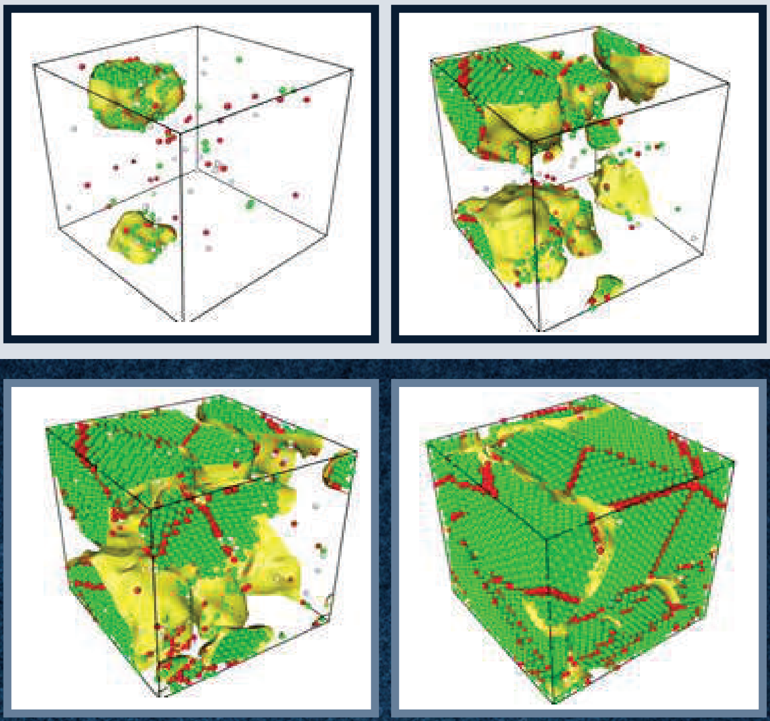

(J. Met. Mater. Sc.)

Vol. 63, No. 3 - 4, July-December 2021

Journal of Metallurgy and Materials Science

ISSN : 0972-4257 (Print version)
ISSN : 0974-1267 (Electronic version)
jmms.nmlindia.org

Editor in Chief

Editorial Advisory Board

Principal Editor

Co-Principal Editor

Editorial Board

Scope of the Journal : Journal of Metallurgy and Material Science (JMMS) publishes original articles, review reports and short communications in the areas of minerals, metals and materials tracing the overall life cycle of structural as well as functional materials. The journal lays special emphasis on fundamental sciences related to metallic materials and their applications.

The scope of JMMS may be enumerated as: Mineral processing; Extractive metallurgy: ferrous and non-ferrous; Processing of metals; Advanced joining of metals; Mechanical behaviour of materials; Materials failure mechanisms including Creep, Fatigue, Fracture and Corrosion; Characterization of materials; Non-Destructive Techniques; Functional materials; Computational materials engineering; Metallurgical waste recycling and utilization of metallurgical and electronic wastes.

Cover : Simulation of crystal growth during solidification of aluminium at cooling rate 1k/ps. White, red, blue and green atoms correspond to amorphous, HCP, BCC and FCC. Journal of Metallurgy and Materials Science (JMMS), 63(3-4), 60-72, 2021.

Copyright : On acceptance of manuscript for publication, the copyright is automatically transferred to publisher by authors. Only unpublished work and the paper not submitted for publication elsewhere will be published. Papers presented in conference where full papers not submitted, work published in reports, reviews, or thesis may be considered. Consent from all co- authors is mandatory prior to submission of the manuscript. On receiving the manuscript, it is presumed that the corresponding author has taken consent from co- authors.

Plagiarism Policy : Authors are requested to submit unique manuscript free form plagiarism. We follow the guideline of UGC for handling plagiarism as per rule published here: https://www.ugc.ac.in/pdfnews/7771545_academic-integrity-Regulation2018.pdf. Manuscripts within 10% similarity will be accepted for review. Authors will be asked to resubmit manuscript if the similarity is above 10 to 40%. For more than 40% similarity, the manuscript will be rejected.

Subscription : Rs 6000 (for 1 year) ; All correspondence regarding subscription should be addressed to Email: kritnml@gmail.com

All articles are freely accessible on the website of the Journal of Metallurgy and Material Science (jmms.nmlindia.org)

Editorial Office
Knowledge Resources and Information Technology
CSIR – National Metallurgical Laboratory, Jamshedpur 831007, India
Telephone: 0657- 2345108/5109, Email: eb.jmms@gmail.com

Published by: Director, CSIR-National Metallurgical Laboratory, Jamshedpur- 831007, India
www.nmlindia.org

ISSN 0974-1267 (Online)
ISSN 0972-4257 (Print)

Journal of Metallurgy and Materials Science
(Formerly NML Tech. Journal)

Vol. 63, No. 3-4, July-December 2021

CONTENTS

Journal of Metallurgy and Materials Science, Vol. 63, No. 3-4, July-December 2021
Printed in India, © NML, ISSN 0972-4257

Effect of Uniaxial Tensile Strain and Heat Treatment on Corrosion Behavior of AISI 304 Stainless Steel

SUJIT KUMAR GUCHHAIT *, **SHAMPA DHAR, P. K.MITRA**
Metallurgical and Material Engineering Department, Jadavpur University, Kolkata-700032, India

Abstract : In this present study, we are attempted to correlate the corrosion behavior of AISI 304 stainless steel (SS) caused by the microstructural changes occurring due to the combined effect of different degrees of uniaxial tensile strain and heat treatment. For this purpose, AISI SS304 samples were prior deformed uniaxially from 10% to 50%. The deformed portion was cut to small rectangular pieces and heat-treated at a temperature of 600^0C for 1 hr in Vaccum (air pressure ~ 10^{-3}mbar). This study reveals that corrosion resistance property has been significantly changed with deformation and sensitized temperature as compare to deformed unsensitized stainless steel. XRD, SEM and hardness testing were carried out to understand the microstructural changes. Potentiodynamic polarization and EIS study were done to characterize the corrosion properties of the strained and unstrained AISI 304SS. It is noted that corrosion current (I_{corr}) increased due to the formation of chromium carbide or deformation band in the structure. Form the EIS study it is also established that polarization resistance at 600 °C temperature and deformation decreased due to formation of tempered martensite along with carbide precipitation.

Keywords : *AISI 304 stainless steel, Tensile strain, Heat treatment, XRD, polarization study, EIS*

1. INTRODUCTION:

Austenitic stainless steel (SS) is the backbone of the modern industry since it finds a huge application in nuclear, chemical, petrochemical, power generation allied industry due to its high ductility, excellent mechanical strength, and corrosion resistance properties [1]. The high chromium (Cr) percent (> 12 %) in these alloys plays an important role to achieve enhanced resistant properties against various uniform corrosions [1-3]. The major drawback related to these steels is their vulnerability to intergranular corrosion (IGC) because of sensitization [4]. The sensitization process involves the precipitation of chromium carbides and the depletion of chromium in the grain boundaries when steel is subjected to heat or slowly cool during the temperature range 1123K to 723K [5 – 13]. The sensitization process depends on several factors like; heating temperature heating, chemical composition, time [5, 14 -16]. Several studies are revealed sensitization can also be influenced by prior deformation or strain [17- 27]. Kain, et al. reported that 304, 304L and 304LN grade SS developed martensite phase after 15% cold working which led to sensitize at 500 ^{0}C temperature [28]. Singh et al. showed that cold deformation improved the degree of sensitization as high as 65 times the undeformed AISI 304 at 500^0C [29]. They are also suggested that with increasing deformation; the carbide precipitation takes place at the grain boundary region. Atanda et al. are observed that SS316L was sensitized when heated to 750 – 850 ^{0}C for 0.5 – 2 hrs before normalizing[30]. Recently, Zhang et al have investigated the effects of pre-strain (up to 20 %) on the degree of sensitization (DOS) and IGC of 304 SS which was thermally aged at 750 °C for one hour [31]. The study revealed that the degree of sensitization and the susceptibility to IGC are proportional to the applied pre-strain in 16 % copper-copper sulphate - sulphuric acid solution. In our early study, we have reported that DOS of 304 SS depended on the extent of deformation as well as sensitization temperatures [32]. Earlier intergranular corrosion due to cold deformation along with low temperature sensitization has been reported at comparatively higher temperature and longer ageing time [18, 29, 31]. Hence in view of the above, the present study is focused on the correlation between the corrosion behavior of AISI 304 stainless steel (SS) caused by the microstructural changes taking place owing to the combined effect of different degrees of uniaxial tensile strain and heat treatment at temperature 600 °C with

Corresponding Author :
Email: sujitguchhait.chem@gmail.com

a soaking time of 1 h. The samples were investigated by X-ray Diffraction technique (XRD), Scanning electron microscope (SEM) and Vickers hardness to understand the microstructural changes due to prior deformation and heat treatment. The electrochemical study was carried out through polarization and impedance spectroscopy in the 1N H_2SO_4 solution. It is observed that corrosion resistance property of the deformed and sensitized stainless steel samples was decreased due to formation of tempered martensite along with carbide precipitation.

2. **EXPERIMENTAL**

The chemical composition of the AISI 304 stainless steel (thickness 3 mm) in this present study is given in Table 1. Two tensile specimens of gauge length 30 mm each were machined and deformed at various uniaxial strain (10%, 20%, 30%, 40%, 50%) using the Instron™ tensile testing instrument at a strain rate of 10^{-3} per second. After that, the gauge length portion of the sample has been cut into five rectangular pieces. One set of samples (i.e. no strain, 10% strain, 20% strain, 30% strain, 40% strain, and 50% strain) was heat-treated at temperature 600 ^{0}C. The heat treatment was carried out under vacuum conditions(air pressure ~ 10^{-3}mbar) (Figure 1) and the soaking time was continued for 1 h followed by furnace cooling.

Table 1. Chemical composition (wt %) of AISI 304 stainless steel

C	Ni	Cr	Mn	Si	S	P	Fe
0.039	8.62	18.89	1.49	0.56	0.009	0.031	Balance

Figure 1.Vacuum-sealed (air pressure ~ 10^{-3} mbar) AISI 304 samples

2.1. Material Characterization:

1The XRD analysis of all the samples was performed by Rigaku X-Ray Diffractometer, Ultima III using Cu Kα (0.154056 nm) radiation in the 2 theta range 30° to 80°. The microstructural analysis of each sample was investigated with scanning electron microscopy (SEM, JEOL JSM-6360). Before microstructural analysis, all the samples were polished with different grade emery papers and washed in DI water then etched by10 % HNO_3 + 30 % HCl + 60 % DI water solution. The hardness of the investigated samples of AISI 304 austenitic stainless was taken in Vicker's hardness tester. The hardness measurements were done using a load value of 30 kg for 5 sec.

2.2. *Electrochemical Characterization:*

Electrochemical studies were done using a standard three-electrode system by Gamry Instrument at room temperature using a 1NH_2SO_4 solution. For the electrochemical measurement, graphite rod and saturated calomel electrode (SCE) were used as counter electrode and reference electrode respectively. The deformed and sensitized AISI 304 samples were used as a working electrode. Prior to each experimental performance, the working electrodes were polished with emery paper progressively up to 2/0 and finally polished by cloth, then degreased with alcohol and washed with running distilled water twice. Potentio dynamic polarization studies of the samples were performed with a scan rate of 1 mV/s in the 1N H_2SO_4 solution. Electrochemical Impedance Spectroscopy

(EIS) study was also carried out in the same instrument in a frequency range from 0.01 Hz up to 100 kHz at 10 mV amplitude in 1N H_2SO_4 solution. Here all electrochemical curves were analyzed by Echem Analyst software and all potentials are reported with respect to SCE.

3. RESULTS AND DISCUSSION:

Figure 2 (a - b) shows the XRD patterns of the non-heat-treated and heat-treated samples after deformation. Figure 2a compares the XRD patterns of strained and unstrained samples. It reveals that as received (unstrained and non-heat treated) sample shows the fcc (γ) phase along with the martensite phase in the matrix [32]. With increasing strain, the intensities of austenite peaks are found to gradually decrease and martensite peaks appeared. However, a change is observed at a 20 % strained sample where α' (110) peaks are vanishing due to the preferred orientation [32]. However,α' (110) peaks re-appears at 30 % strain and intensity gradually increases with the percentage of strain. This deformation-induced martensite(DIM) during tensile deformation may be due to stacking fault energy of AISI 304 SS [29]. At higher temperature, at 600 ^{0}C, α' martensites present in all diffractograms (Figure 2b) and it beg into transform into tempered martensite($\alpha + M_{23}C_6$) having carbide precipitation results in the phase mixture of α and α' [32]. Therefore, at a higher,temperature, a significant enhancement in the peak intensity adjacent to the (111) γ peak is observed.

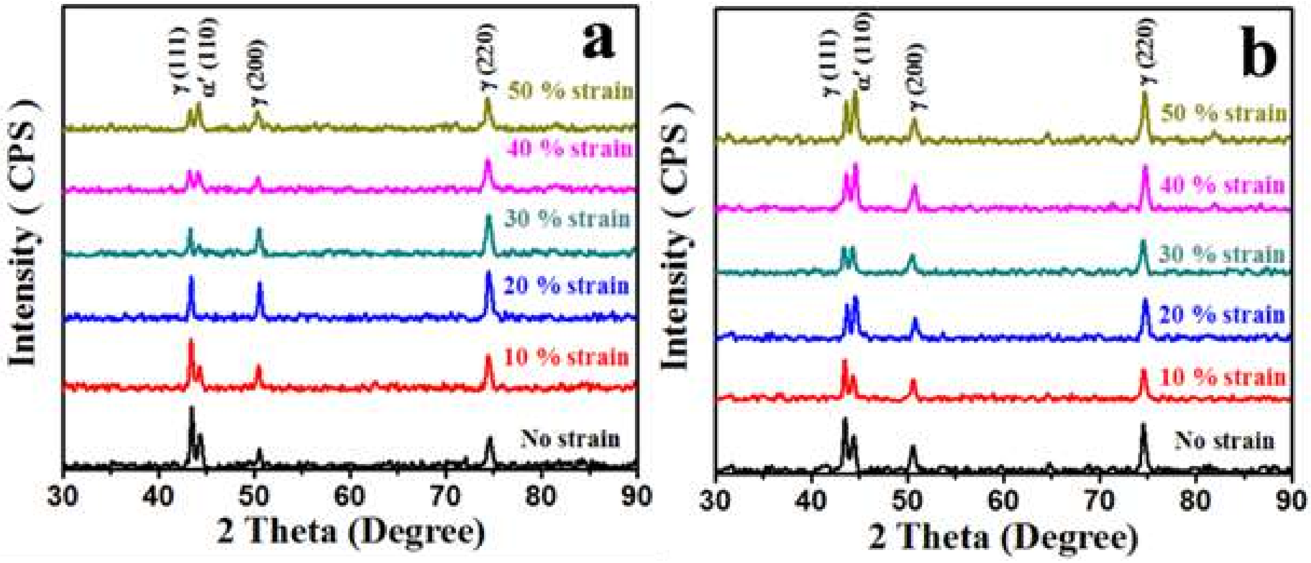

Figure 2. XRD analysis (a) non-heat-treated (b) heat-treated at 600 ^{0}C samples at different strain

Figure 3 (a – f) and Figure 4 (a – f) shows the Scanning Electron Micrographs (SEM) of strained and unstrained samples. Figure 3a reveals that little amount of deformation band is present in the unstrained non heated sample. It was found that with increasing strain significant microstructural change is observed. Populations of deformation bands are predominantly starting forming from 20 % strain (Figure 3(b – f)). Hence it is worth mentioning that, at the grain boundary region, these deformation bands can act as the energetically favorable zone for the precipitation of chromium carbide, resulting in the formation of depletion regions in the near band zones. It is noted that with increasing temperature (600 ^{0}C) these deformation bands are clearly observed (Figure4 (a – f)). Interestingly at higher strain and temperature condition, chromium carbide precipitation took place along the grain boundary and deformation band region are also significantly prominent in the micrographs. It is also being noted that carbide precipitation is a time temperature-dependent process that is determined mostly by carbon diffusion at low temperatures and carbide solubility at elevated temperatures [33].

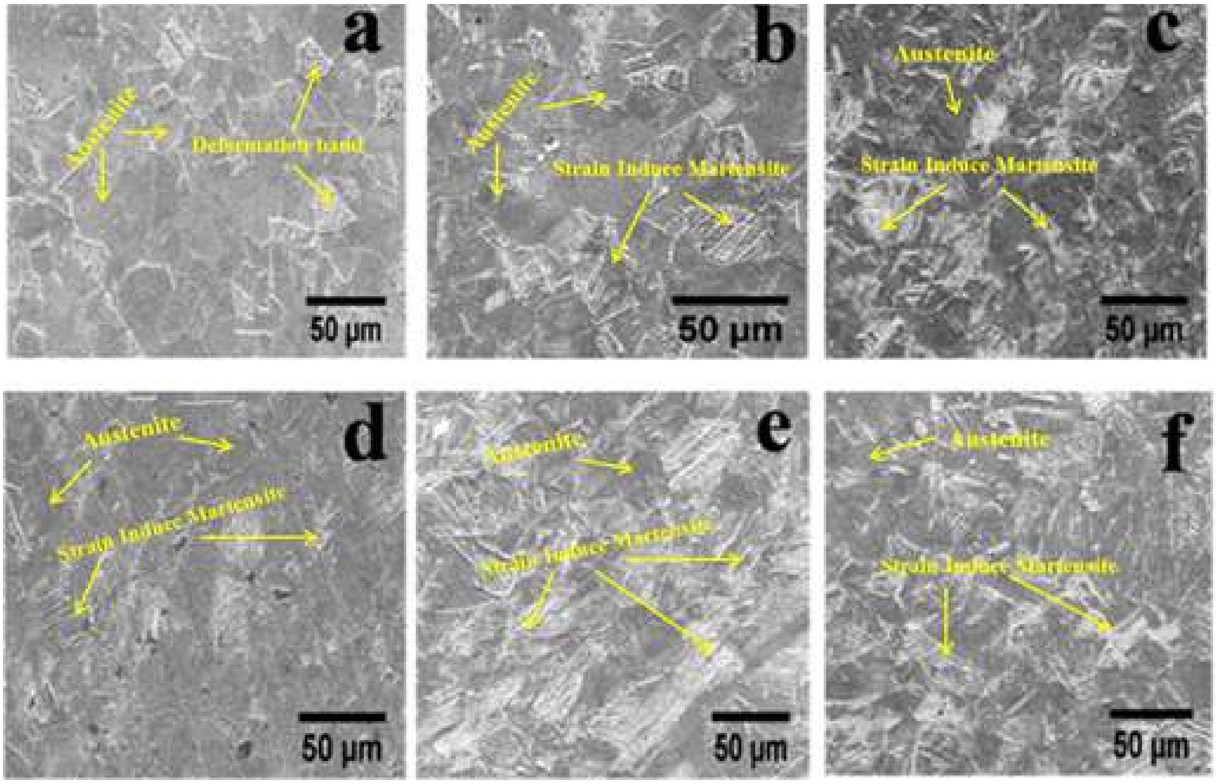

Figure 3.SEM micrographs of non-heat-treated samples (a) un-strain (b) 10% strain (c) 20 % strain (d) 30% strain (e) 40 % strain (f) 50% strain

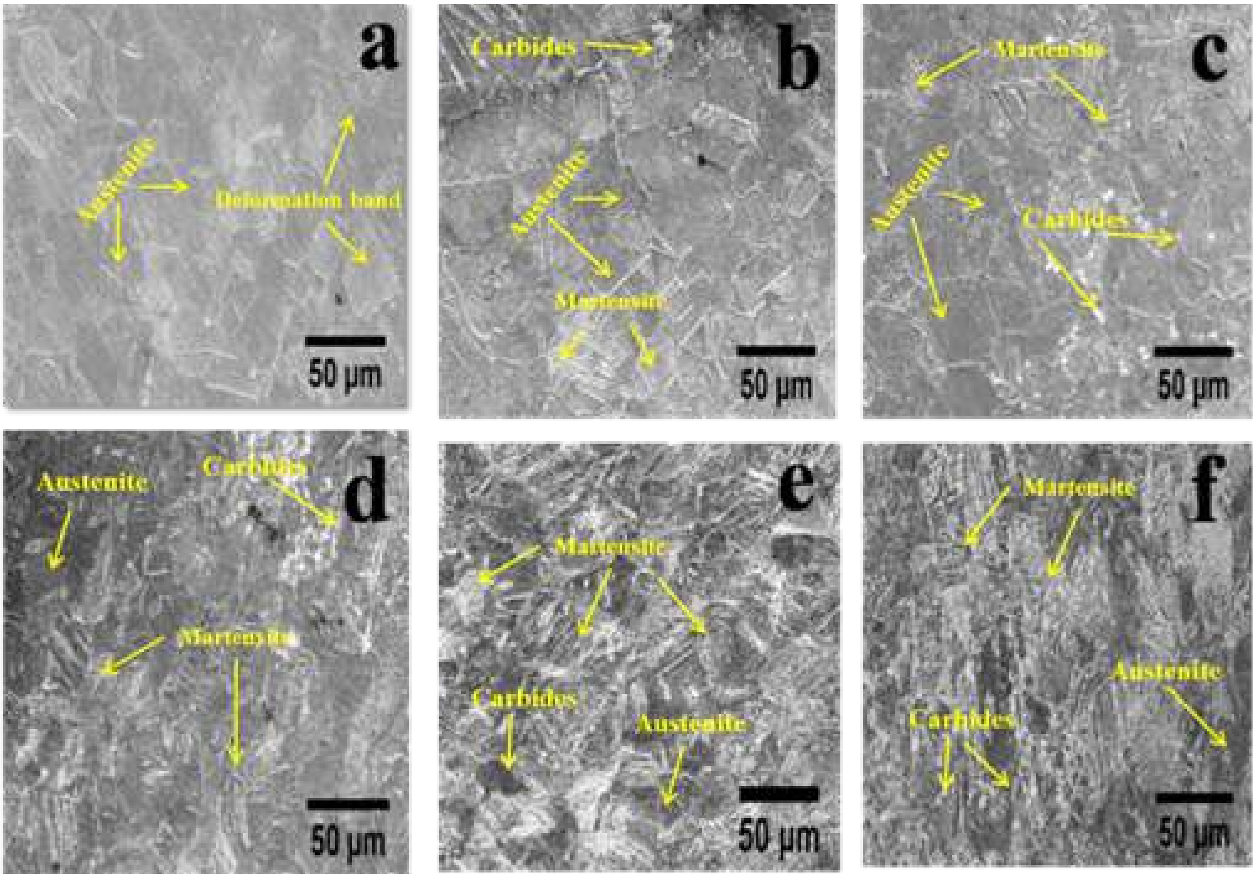

Figure 4.SEM micrographs of 600 ^{0}C heat treat samples (a) unstrain (b) 10% strain (c) 20 % strain (d) 30% strain (e) 40 % strain (f) 50% strain

Vicker's hardness of the samples is given in Figure 5. From XRD and SEM study it was revealed that as received sample contains fcc (γ) phase along with martensite and with increasing strain SIM formation takes place (except 20 % strain). It is reported that the martensite phase is harder than the ferrite or austenite phase [34]. Hence, the hardness of non-heat-treated samples increases with increasing strain. In the case of 600 ^{0}Cheat-treated samples, the hardness of 10% deformed sample decreases as compared to the unstrained sample which may be due to stress relaxation. Nevertheless, after that hardness value increases upto 30 % deformed which is may be due to the formation of martensite phases along with and carbide precipitation (supported by XRD and SEM study) along the grain boundaries. Although hardness value again decreases at higher deformation because of carbon diffused toward grain boundary along with the martensite phase is starting disappearing from the microstructures.

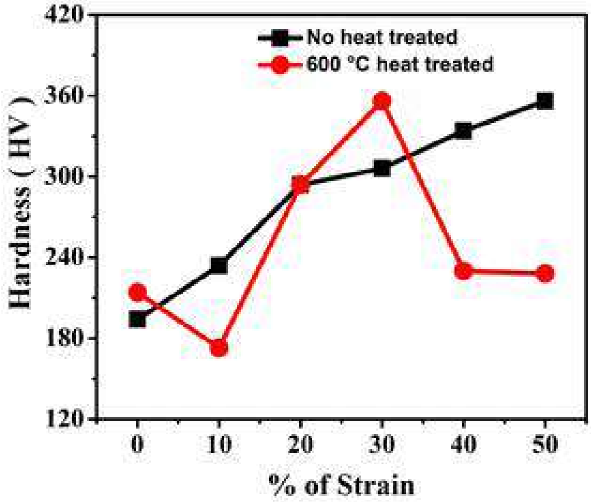

Figure 5.Vickers hardness of the non-heat treated and heat-treated samples

A comparative polarization curve of the non-heat treated unstrained and strained samples in 1 N H_2SO_4 solution is given in Figure 6a. It is found that the corrosion current (I_{corr}) of the as-received unstrain sample is 3.7 μA/cm^2 which gradually decreases upto 20 % strained samples (I_{corr} = 0.31 μA/cm^2) due to suppression of (111) α' phase as discussed in the previous section.

However after that, with increasing strain, corrosion current enhances due to DIM and 50 % strained sample attained maximum Icorr (I_{corr} = 564.5 μA/cm^2) (Table 2). A comparison curve of 600 ^{0}Cheat-treated samples is shown in Figure 6b. 600 ^{0}Cheat-treated samples show reduced Icorr up to 30% strained sample (Table 2). After 30% of deformation I_{corr} increases which is due to the precipitation of chromium carbide at higher deformation and temperature. From Figure 6 (a – b) it is also revealed that deformed non-heat-treated samples give superior nobler properties than deformed 600 °C heat-treated samples (Table 2).

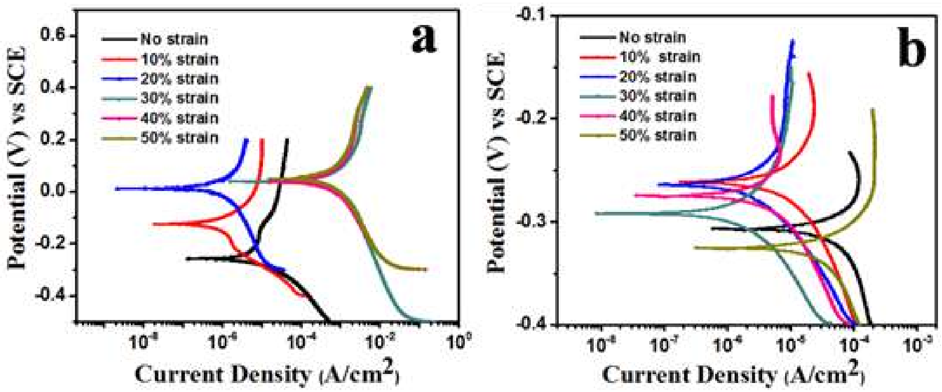

Figure 6.Potentiodynamic polarization study of (a) non-heat-treated (b) heat-treated at 600 ^{0}C samples at different strain

Table 2. Polarization data of the non-heat-treated and heat-treated samples at different strain

Sample	**I_{corr} (µA/cm^2)**		**E_{corr} (mV vs. SCE)**	
	No Heat	**At 600 ^{0}CHeated**	**No Heat**	**At 600 ^{0}CHeated**
No Strain	3.7	36.2	-260.5	-308.9
10% Strain	0.87	6.1	-127.6	-265.0
20% Strain	0.31	2.2	14.8	-265.0
30% Strain	545.2	1.1	20.8	-293.5
40% Strain	548.4	3.1	25.2	-269.7
50% Strain	564.5	38.8	34.1	-334.7

Electrochemical Impedance Spectroscopy (EIS) studies were done for a better understanding of the fundamental feature of electrochemical behavior at the electrolyte - metal interface. The electrochemical process at the surface is a complex phenomenon, which consists of different ions interactions, polarization resistance (R_p), impedance and other parameters due to interaction between electrolyte and electrode. The overall process can be summarized by an equivalent AC electrical circuit which is depicted and discussed in this section. The EIS spectra of all the samples are shown in Figure 7 (a – b) and the EIS data are tabulated in Table 3. All the spectra were fitted in the constant phase element model (CPE) (Figure. 8a) except non-heat-treated samples of 30 %, 40 % and 50 % strained samples. These are fitted in CPE with diffusion model (Figure 8b). Mathematically, simple CPE model can be expressed by:

$$Z_{CPE} = \frac{1}{Y_0(j\omega)\alpha}$$

Where j represents the imaginary function, ω is the angular frequency, Y_0 is CPE constant, α is an exponent of constant phase element ranging from 0 to 1. A high α value is typically for the material which has a strong capacitive nature. A higher polarization resistance (R_p) implies greater corrosion resistance of the material in a given environment. Figure 7a shows the Nyquist plot of the non-heat-treated samples. From these curves, it is clear that un-strained, 10% and 20% strained samples tend to become semicircle. It is found that with increasing strain (upto 20 %) polarization resistance (R_p) increases however after that R_p decreases with deformation due to an increase of DIM in the matrix(Table 3). On the other hand, 600^{0}C heat treatment samples also tend to form semi-circle shows in the Nyquist plot. From Figure 7 (a – b) it is clearly revealed that increasing stain and temperature corrosion resistance properties deteriorated as compared to the non-heat-treated samples due to the formation of carbide precipitation.

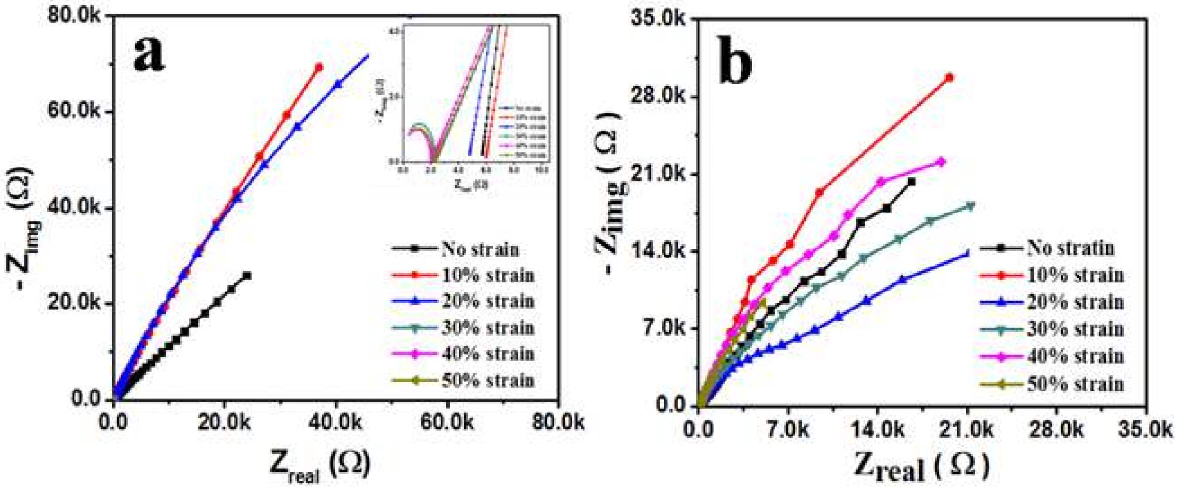

Figure 7.Nyquist plot of (a) nonheat-treated (b)600 ^{0}Cheat-treated samples at different strain

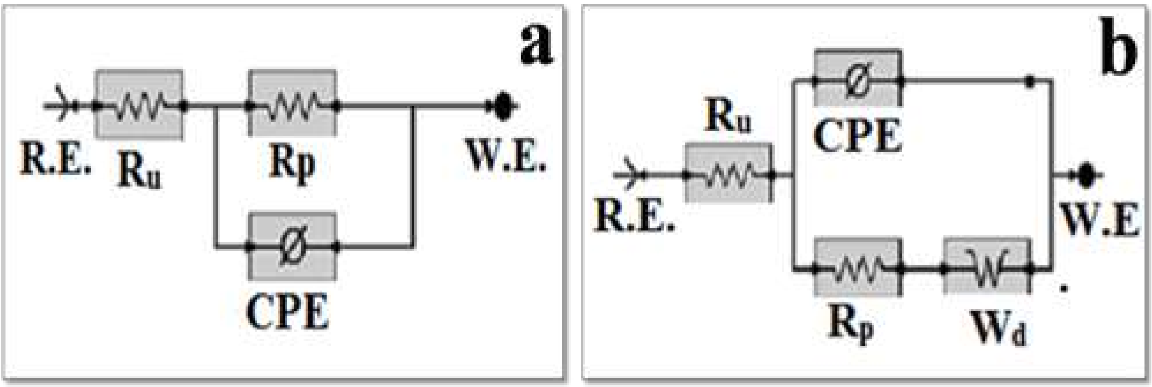

Figure8: Equivalent model circuit for (a) CPE; (b) CPE with diffusion model where, R_u = Solution resistance, CPE = Constant phase element, R_p= Polarization resistance, W_d = Warburg element

Table 3: Electrochemical impedance data of all the samples

Sample	R_u ohms (Ω)		$R_p$ohms (KΩ)		Y_0 ($\times 10^{-6}$) (S*s^a)		A		Wd (S*s$^{\wedge 1/2}$)	
	No Heat	600 °C Heated	No Heat	600 °C Heated	No Heat	600 °C Heated	No Heat	600 °C Heated	No Heat	600 °C Heated
No Strain	4.5	3.2	27.6	60.80	91.85	73.5	0.68	0.73	-	-
10 % strain	5.8	5.3	376.4	326.1	93.12	86.7	0.75	0.74	-	-
20 % strain	4.6	3.4	445.9	27.72	70.56	110.5	0.75	0.73	-	-
30 % strain	0.3×10^{-3}	1.7	0.002	55.20	0.36	86.07	0.95	0.75	0.18	-
40 % strain	0.1×10^{-3}	3.1	0.0019	88.03	0.48	102.4	0.91	0.77	0.24	-
50 % strain	0.8×10^{-3}	2.4	0.0022	87.79	0.8	106.2	0.93	0.76	0.22	-

4. CONCLUSIONS:

From the above results and discussion; a correlation between the corrosion behavior of AISI 304 SS caused by the microstructural changes taking place due to the combined effect of different degrees of uniaxial tensile strain (10 %, 20 %, 30%, 40 %, and 50%) and heat treatment is established. So in conclusion,

a. AISI 304 stainless steel significantly influenced by uni-axial tensile stain and sensitization temperature. The SEM micrographs obtained from the strained and heat-treated samples showed the existence of deformation bands in all the samples. At higher strain and temperature, chromium carbide precipitations along the grain boundary and deformation band region are also significantly prominent.

b. The corrosion resistance properties and solution resistance properties of sensitized and un-sensitized samples are notably affected by marten site and carbide phases. At higher deformation (50 %) and higher heat treatment temperatures complex microstructural changes cause opposing corrosion behavior in the sample. In 1 N H_2SO_4 solution, deformed non-heat-treated samples give superior nobler properties than deformed 600 °C heat-treated samples.

ACKNOWLEDGMENTS

The authors would like to Jadavpur University, Kolkata to carry out this research work. SKG also thanks to Dr. Paramita Mukherjee, Dr. N. Gayathri Bannerjee of Variable Energy Cyclotron Centre (VECC), Kolkata and Dr. P. S. Chowdhury of Jadavpur University, who gives their valuable suggestion for conducting heat-treatment process and material problems.

REFERENCES

[1] G. George, H. Shaikh: 1-Introduction to austenitic stainless steels, Corrosion of austenitic stainless steels, Wood head Publishing, pp1-36, 2002

[2] V. G. Rivlin, G. V. Raynor: 1: Critical evaluation of constitution of chromium-iron-nickel system, Int. Met. Rev. 25, 21-40, 1980

[3] V. P. Kujanpaa, N.Suutala,T. Takalo, T. Moisio: Correlation between solidification cracking and microstructure in austenitic and austenitic-ferritic stainless steel welds, Weld.Res. Inter.,9, 55-75, 1979

[4] C.S. Tedmon, D.A.Vermilyea, J.H. Rosolowski: Intergranular corrosion of austenitic stainless steel, J. Electrochem Soc., 118, 192-202, 1971

[5] R.T. Holt, W. Wallace: Impurities and trace elements in nickel - base super alloys, Int. Met. Rev. 21(1), 1-24, 1976

[6] X. Huang, H. Wang, W. Xue, S. Xiang, H. Huang, L. Meng, G. Ma, A.Ullah, G. Zhang: Study on time-temperature-transformation diagrams of stainless steel using machine-learning approach, Comput. Mater. Sci. 171, 109282, 2020

[7] D. Özyürek: An effect of weld current and weld atmosphere on the resistance spot weld ability of 304L austenitic stainless steel, Mater. Design.29, 597-603, 2008

[8] Z.Y. Xue, S. Zhou, X.C. Wei: Influence of pre-transformed marten site on work-hardening behavior of SUS 304 metastable austenitic stainless steel, J. Iron Steel Res. Int. 17, 51-55, 2010

[9] S. M. Tabatabaeipour, F. Honarvar: A comparative evaluation of ultrasonic testing of AISI 316L welds made by shielded metal arc welding and gas tungsten arc welding processes, J. Mater. Process. Tech., 210, 1043-1050, 2010

[10] P. M. Silva, H.F. de Abreu, V.H. de Albuquerque, P. de LimaNeto, J.M. Tavares: Cold deformation effect on the microstructures and mechanical properties of AISI 301LN and 316L stainless steels, Mater. Design.32, 605-614, 2011

[11] A.J. Sedriks: Corrosion of stainless steel, 2 ed., United States, N. P., Web, 1996

[12] V. Cihal, Intergranular Corrosion of Steels and Alloys, Elsevier, Amsterdam, 1994

[13] A.S. Lima, A.M. Nascimento, H.F. Abreu, N. P. de Lima: Sensitization evaluation of the austenitic stainless steel AISI 304L, 316L, 321 and 347, J. Mate. Sci., 40, 139-144, 2005

[14] M.D. Mathew, G. Sasikala, K.B. Rao, S.L. Mannan: Influence of carbon and nitrogen on the creep properties of type 316 stainless steel at 873 K, Mater.Sci. Eng.A, 148, 253-260, 1991

[15] M. Stalder, S.Vogel, M.A. Bourke, J.G. Maldonado, D.J. Thoma, V.W.Yuan: Retransformation ($\alpha' \rightarrow \gamma$) kinetics of strain induced marten site in 304 stainless steel, Mater. Sci. Eng. A, 280, 270-281, 2000

[16] R. Beltran, J.G. Maldonado, L.E. Murr, W.W. Fisher: Effects of strain and grain size on carbide precipitation and corrosion sensitization behavior in 304 stainless steel, Acta Mater., 45, 4351-4360, 1997

[17] K.H. Lo, D. Zeng, C.T. Kwok: Effects of sensitisation-induced martensitic transformation on the tensile behavior of 304 austenitic stainless steel. Mater.Sci. Eng.A, 528, 1003-1007, 2011

[18] C. S. TedmonJr, D.A. Vermilyea, D.E. Broecker: Technical note Effect of cold work on intergranular corrosion of sensitized stainless steel, Corrosion., 27, 104-106, 1971

[19] H.D. Solomon, The influence of prior deformation on continuous cooling sensitization of type 304 stainless steel, Corrosion., 36, 356-661, 1980

[20] S. Pednekar, S. Smialowska: The effect of prior cold work on the degree of sensitization in type 304 stainless steel, Corrosion., 36, 565-577, 1980

[21] H.D. Solomon, D.C. Lord: Influence of strain during cooling on the sensitization of type 304 stainless steel, Corrosion., 36, 395-399, 1980

[22] C.L. Briant, A.M. Ritter: The effect of marten site on the sensitization of low carbon 304 stainless steel, Metal. Trans. A.,12(5), 910-913, 1981

[23] M.J. Povich, D.E. Broecker : Stress corrosion cracking of austenitic stainless steel alloys in high-temperature air-saturated water, Mater. Perform.,18, 41-48, 1979

[24] S. Pednekar, S. Smialowska: TheEffect of Prior Cold Work on the Degree of Sensitization in Type 304 Stainless Steel, Corrosion., 36, 565-577, 1980

[25] K.A. Johnson, L.E.Murr, K.P. Staudhammer: Comparison of residual microstructures for 304 stainless steel shock loaded in plane and cylindrical geometries: implications for dynamic compaction and forming, Acta Metall., 33, 677-684, 1985

[26] E. Almanza, L.E. Murr: A comparison of sensitization kinetics in 304 and 316 stainless steel, J. Mater. Sci., 35, 3181–3188, 2000

[27] C.L. Briant, A.M. Ritter: The effect of gold work on the sensitization of 304 stainless steel, Scr Metall., 13, 177-181, 1979

[28] V. Kain, K. Chandra, K.N. Adhe, P.K. De: Effect of cold work on low-temperature sensitization behaviour of austenitic stainless steels, J. Nucl. Mater., 334, 115-132, 2004

[29] R. Singh: Influence of cold rolling on sensitization and intergranular stress corrosion cracking of AISI 304 aged at 500° C, J. Mater. Process. Tech., 206, 286-293, 2008

[30] P. Atanda, A. Fatudimu, O.Oluwole: Sensitisation Study of Normalized 316L Stainless Steel, J. Miner. Mater. Char. Eng., 9, 13-23, 2010

[31] X. Zhang, J. Tang, H. Liu, J. Gong: Effects of pre-strain on sensitization and interganular corrosion for 304 stainless steel, Eng. Fail. Anal., 106, 104179, 2019

[32] P.S. Chowdhury, S.K. Guchhait, P.K.Mitra, P. Mukherjee, N.Gayathri,M.K.Mitra: Understanding the effect of uniaxial tensile strain on the early stages of sensitization in AISI 304 austenitic stainless steel, Mater. Chem. Phys., 155, 217-222, 2015

[33] R.K. Dayal, J.B. Gnanamoorthy: Predicting extent of sensitization during continuous cooling from TTS diagram, Corrosion., 36, 104-106, 1980

[34] J. Mola, M. Ren:on the hardness of high carbon ferrous martensite, IOP Conf. Ser.: Mater. Sci. Eng.,373, 012004, 2018

Journal of Metallurgy and Materials Science, Vol. 63, No. 3-4, July-December 2021
Printed in India, © NML, ISSN 0972-4257

Evolution of Nano-crystalline Structures in Aluminium under Rapid Solidification using Molecular Dynamics Simulation

SUNIL KUMAR*, SUCHANDAN KUMAR DAS, AND SHEULI HORE
CSIR-National Metallurgical Laboratory, Jamshedpur 831007, INDIA

Abstract : The molecular dynamics (MD) simulation has used to explore the effect of cooling rate on the crystal nucleation and its growth. Themodynamic analysis (potential energy), atomic mean square displacement and diffusion coefficient have considered to characterize the thermal motion of aluminium. The proportions of locally crystal organization such as fcc, bcc, hcp, etc. of aluminium atoms depend on the cooling rate. For cooling rate 0.1K/ps and 1K/ps (cooling from 1173K to 273K), an fcc crystalline solid aluminium is formed during cooling. But for cooling rate 10K/ps, an amorphous aluminium metal is formed at 273K. The dislocation extraction algorithm (DXA), consists of dislocation of the boundary and Burgers vectors have used to characterize the crystal defect in solidification of aluminium. For cooling rate 0.1K/ps, at the stage of nucleation, many crystal defects are found, but as temperature decreases, crystal defect slowly disappears. In case of cooling rate 1K/ps, crystal defects have seen in very early stage of nucleation but these defects grow continuously as temperature decreases. The thermodynamic analysis behind the origin of crystalline and amorphous aluminium has studied. The face center crystal, fcc, structure of aluminium is a most favorable energy state. Amorphous aluminium is an energetically unfavorable metastable state. Diffusion coefficient decrease as the solidification proceeds, but at the nucleation of crystal, it display a sudden decrease to a negative value and then become nearly zero. An abrupt drop to a negative value, comes due to attractive nearest-neighbor lattice packing and crystal nucleation and its growth.

1. INTRODUCTION

Under the rapid solidification process (RSP) of metals and alloys, phase transition can be formed depending on the thermal motion of atoms. At extremely high cooling rate, the crystallization may be inhibited and a metallic glass are formed. Under such situations, the liquid phases with the short-range order structures are saved in the solid state [1]. Studying the phase transition phenomena in metallic material at such extremely high cooling rate is not experimentally feasible. The aim of this work should be to study the structural evolutions in aluminum during RSP using MD simulations. The crystallization during RSP needs to be investigated and the effect of crystalline behavior of the re-melting temperature may be investigated if required. From last two decades, scientists have shown that metal processing such as rapid solidification, controls the most micro structural properties of aluminium metal by using both experimental [1-16] and computational simulation[19-35] methodology.

Experimentally, rapid solidification process have carried out by using gas atomization[10], spray atomization [11], melt spinning [12], glass-fluxing method [13], drop tube technique [14], rapid quenching [15], etc. The rapid thermal energy extraction that occurs during rapid cooling create a solid state of material which have large deviations from equilibrium, shows many changes in material properties such as an extension of solid solubility, formation of non-equilibrium or meta-stable crystalline phases, retention of disordered structure, modification of grains shape and size. These properties are responsible for enhancement in mechanical properties, thermal stability, wear resistance, and high temperature strength etc. compared to the conventional solidification process. Recently, Wang *et al.* [16] have shown that the creation of homogeneous microstructures which improve mechanical properties of aluminium alloy by increasing the cooling rate through roll casting technique. Overman *et al.* [17] have studied the microstuctural characteristic and mechanical properties of rapid solidify aluminium alloy both at room temperature and 300K. They have found the ultimate tensile strength 544.2 MPa at room temperature and 298.0 MPa at 300 °C. Despite of many experimental studies, there is a need of study of atomic/molecular modeling of rapid solidification of aluminium at the nanometer scale and cooling rate above 10^7K/ps, which is more difficult by experiments.

Corresponding Author :
Email: sunil@nmlindia.org

Atomic/molecular modeling and mathematical analysis also have used to study the rapid solidification [19-35] by few research groups. They have studied the structural order formation, internal energy evolution, common neighbor analysis, cluster formation during solidification, etc at various cooling rates. However, we also need to study the crystal structure formation, detection of crystal defect, mass diffusion, thermodynamics of cluster formation in rapid cooling process for a complete study of aluminium metal. Some recently published article has explained structure order formation in aluminium metal during rapid cooling process by Hou *et al.*[19]. They have used a wide range of cooling rate (10^{13} to 10^{11}K/ps) to study the short – range ordered structure in aluminium by using MD simulation. They have found that the cooling rate influence the microstructure only near the liquid–solid transition temperature. They have found mostly two type of structure icosohedral and face centered cubic during fast and slow cooling rate. However, they have not discussed about mass diffusion and the dynamics of the solidification or liquid formation. Some other research groups [20] have also shown that the FCC and metastable HCP structure can co-exist depending on the cooling rate. Liu *et al*. [21] have studied the local atomic structures evolution of aluminium on different cooling rates. They have determined a critical quenching rate at above the glass exhibits the highest structural stability. Further, in literature [54-56], recently classical and reactive molecular dynamics simulation have applied to investigate solidification, mechanical properties and oxidation of aluminium at nano-scale. Despite various studies of structural organization, we also need to study the crystal defect, thermodyanamics of solidification, mass diffusion and the dynamics of solidification at different cooling rate.

Nanoscopic motion of aluminium atoms during solidification, such as self diffusion of atoms in liquid state, or diffusion from liquid to crystal surface is tough to measure experimentally. Though, this motion is one of the most straight forward to visualize by MD. However, apart from visualization, this information does not actually give one much insight into the physics of how and why atoms or molecules move. A more quantifiable measure is essential, of which the self-diffusion coefficient is one of the most common and useful. Hence, we study the short range ordered crystal structure, along with mass diffusion and dynamics during both cooling of aluminium. This study will enhance our understanding on both academic and industrial purposes. We have used large scale MD simulation to study the behavior of aluminium metal during both rapid cooling and rapid heating. For characterization of solidification and melting process behavior, pair distribution function, center of symmetry, bond orientational order and mean square displacement have been computed to elucidate aggregation of atoms, crystal structure formation and solidification dynamics respectively.

2. MD SIMULATIONS

For MD simulation, We have used LAMMPS [36], VMD [37] and OVITO [38] softwares for simulation, trejectory visualization and data analysis. The EAM force field as given by Mendelev *et al.* [39] is used here. The total energy, E is given by

$$E = \sum_{i=1}^{N-1} \sum_{j=i+1}^{N} \varphi_{ij}(r_{ij}) + \sum_{i=1}^{N} F_i(\rho_i) \tag{1}$$

$$\rho_i = \sum_{i} \psi(r_{ij}) \tag{2}$$

Where ψ (r_{ij}) is the electron density of aluminium atoms. The equation of motion of aluminium atoms can be written as

$$m\frac{d^2 r_i}{dt^2} = F_i = -\nabla_i E \tag{3}$$

The equation (3) is integrated at time step using velocity Verlet algorithm [40] as given in equation (4) and (5).

$$r_i(t+\Delta t) = r_i(t) + v_i(t)\Delta t + \frac{1}{2}(\Delta t)^2 a_i(t+\Delta t) \tag{4}$$

$$v_i(t+\Delta t) = v_i(t) + \frac{1}{2}\Delta t[a_i(t) + a_i(t+\Delta t)] \tag{5}$$

Here v and a are velocity and acceleration of the i^{th} atom.

For the study of solidification and melting process, we have created a simulation system by placing aluminum atoms with an ideal FCC structure (lattice parameter 4.05Å) in a 3D simulation box with periodic boundary conditions. The MD simulation framework comprises of two steps: first is equilibration and second is cooling process. In equilibration, the temperature of system is maintained at 1173 and 273K for solidification and melting process respectively, for 100ps to attain an energetically favorable liquid state.

The temperature of system decrease from 1173 to 273K for solidification by using a wide range of cooling rate such as 10 K/ps, 5K/ps, 4K/ps, 2K/ps, 1K/ps, 0.5K/ps, 0.4K/ps, 0.2 K/ps and 0.1K/ps. The pressure of simulation system is maintained at 0bar for equilibration and solidification and melting step. All these temperature and pressure parameters are controlled by Nose-Hoover thermostat and Andersen barostat which is available in open source LAMMPS. The density and internal energy at liquid and solid state have calculated which are found to similar to experimental or simulation published results as given in ref [19]. We stored simulation data at regular interval during simulation for the visualization and analysis.

3. RESULTS AND DISCUSSIONS

We have discussed our results in the next three sections. In the first section, the study of evolution of various crystal structure during the cooling process, in the second section, the thermodynamics behind the various crystal structure and in the third section shows crystal defects.

3.1. *Evolution of crystal nucleation and growth*

The formation of amorphous or crystalline structure in an aluminium sample is expected to depend on the cooling rate. To understand the morphology of the aluminium, the cooling rates have chosen from 0.1K/ps to 10Kps as given in table 1. It is found that three different types of crystal structure have found during cooling: face centered crystal (fcc), hexagonal close packing (hcp) and amorphous depending on cooling rate as shown in figure 1.The initial state of all systems was at liquid state at temperature T=1173K (melting temperature of aluminium T_m =940K). In liquid state all aluminium samples show amorphous structure as given in figure 1 by white atoms. In case of cooling rate 10K/ps, aluminium atoms unable to organize in crystal structure due to very rapid cooling. The atoms are kinetically traps in meta-stable state and unable to form any crystal structure. However, in case of 5K/ps, 1K/ps and 0.1K/ps aluminium atoms are able to form a crystal structure which also strongly depends on the cooling rate. In cooling rate 5K/ps, few small ordered clusters formed, but unable to grow. The ordered cluster has FCC and hcp type crystal structure, but the majority of atoms is organized in random. In case of cooling rate 1K/ps and 0.1K/ps, most of the aluminium atoms are able to crystallize in fcc structure because slowly cooling allow atoms to search most favorable minimum energy state. However, some crystal defect also has seen in the form of amorphous, hcp and other type of packing of atoms. Section 3, consist the detail study of crystal defects.

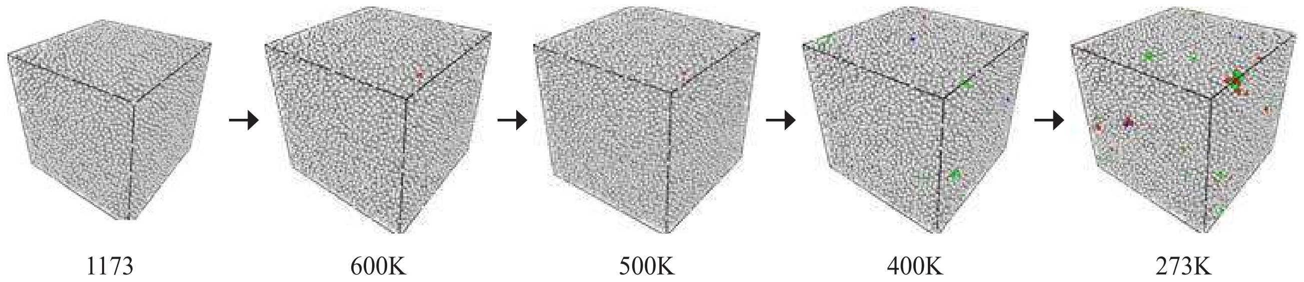

(a) 10K/ps

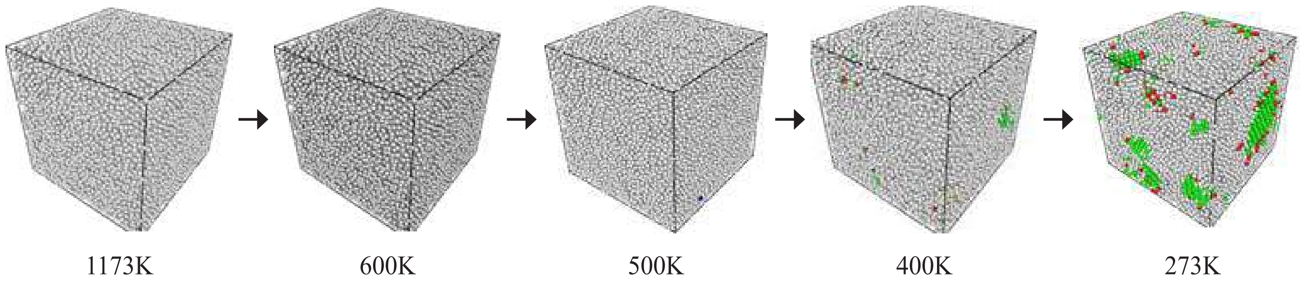

(b) 5K/ps

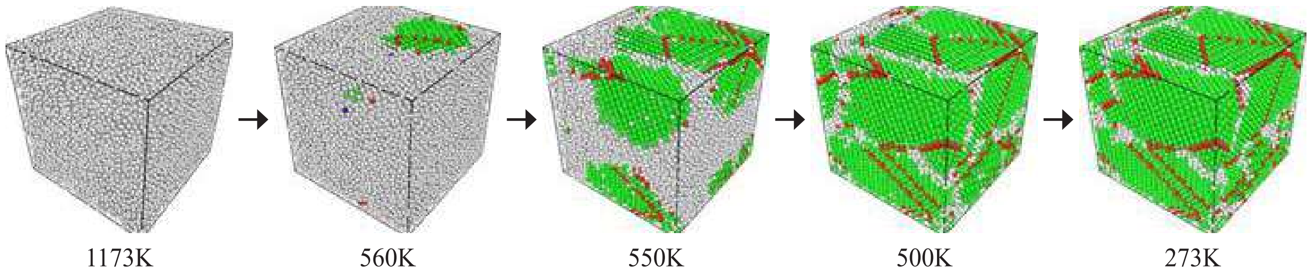

(c) 1K/ps

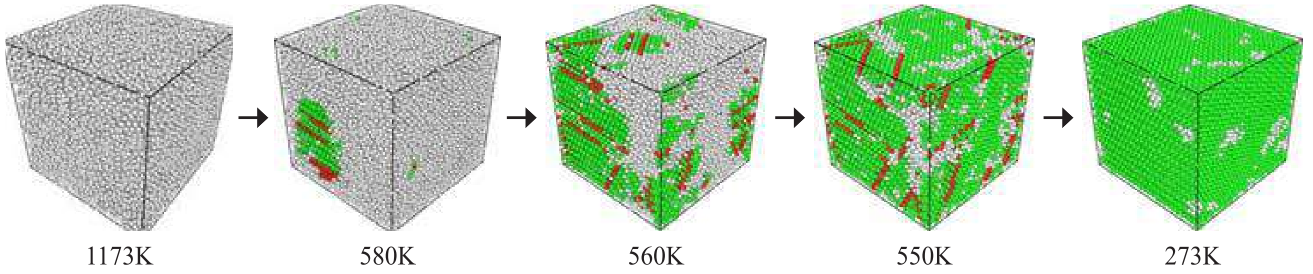

(d) 0.1K/ps

Figure 1. Snapshots of solidification structures under the different cooling rates (a) 10K/ps, (b) 5K/ps, (c) 12K/ps and (d) 0.1K/ps. White, red, blue, and green atoms corresponds to amorphous, HCP, BCC and FCC respectively.

Table 1 Bond order parameters (BOP) for face-centered-cubic, hexagonal close-packed, simple cubic, body-centered-cubic, liquid [45].

Geometry	Q4	Q6	W4	W6
fcc	0.19094	0.57452	-0.15932	-0.01316
hcp	0.09722	0.48476	0.13410	-0.01244
sc	0.76376	0.35355	0.15932	0.01316
bcc	0.08202	0.50083	0.15932	0.01316
liquid	0	0	0	0

The variables of r- g(r) plots with temperature for three different cooling rates are shown in Figure 2. In case of very rapid cooling 10K/ps, r-g(r) plot shows a sharp peak at around at r = 2.65Å, as the temperature rapidly decreases, the height of peak increase, which corresponds to the aggregation of atoms during the solidification process as shown in figure 2(a). In case of cooling rate 1K/ps and 0.1K/ps, g(r) plot shows a sharp peak at high temperature, but as temperature decreases, peaks at r > 3.00 split in many distinct peaks which indicates that the aluminium atom form long rang ordered structure as shown in figure 2 (b) and (c). Figure 2 (d) shows the radial distribution of aluminium structure at 273K, which have formed through various cooling rates. In all samples, the first peak of gI found at r=2.65Å, but the height of the peak is increased as cooling rate decrease, this shows that low cooling results very close packing of aluminium atoms. However, the other peaks at r > 2.65Å, splits in multiple distinct peaks as cooling rate decreases. These distinct peaks indicating toward evolution of long range ordered packing of aluminium atoms.

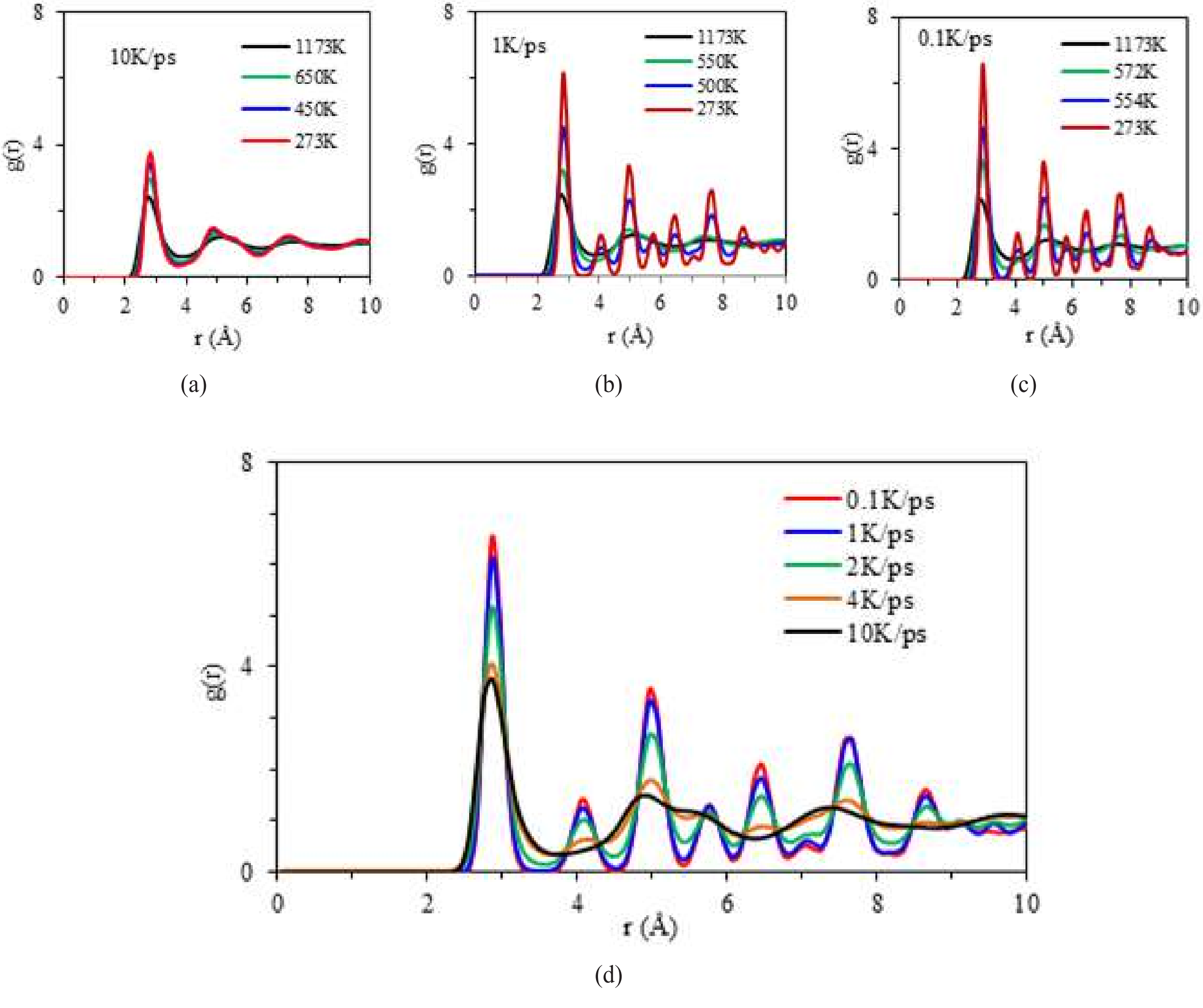

(a)

(b)

(c)

(d)

Figure 2 Variation in g(r) of atoms during various cooling rates: (a) 10K/ps (b) 1K/ps, (c) 0.1K/ps and (d) at 273 K.

To investigate the growth of crystals, the number or atoms belong to the FCC, hcp, bcc, ico and amorphous have calculated during solidification. The amorphous and crystalline region has separated by using an interface mesh as shown in figure 3. At very early stage of crystal nucleation, a small size cluster of atoms has seen, but as the temperature decreases cluster size increases as given in the snapshot. The packing of atoms in the crystal has found different such as fcc, hcp, bcc and ico depending of cooling rate.

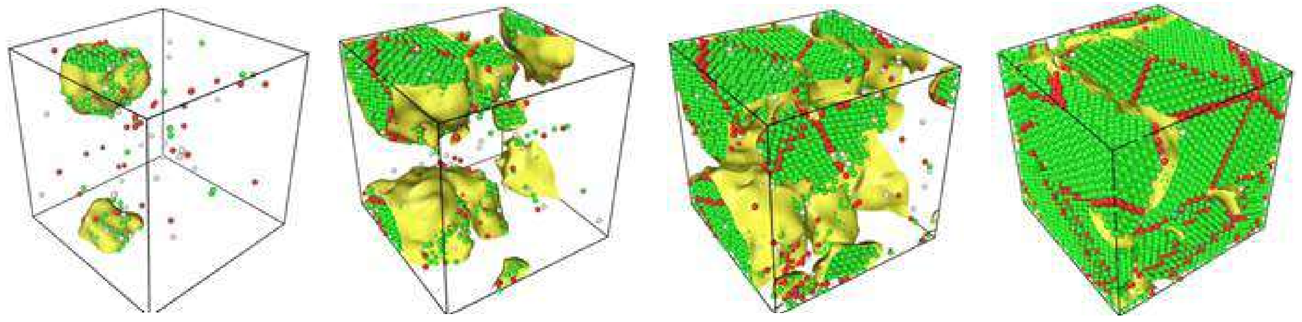

560K (a) 550K (b) 500K (c) 273K (d)

Figure 3 Snapshot of crystal growth during solidification of aluminium at cooling rate 1K/ps. For clear visualization only cluster of crystalline atoms has shown and free region belongs to amorphous atoms. White, red, blue, and green atoms correspond to amorphous, HCP, BCC and FCC respectively.

Figure 4 shows the number of atoms belongs to fcc, hcp, bcc, ico and amorphous have calculated as temperature decreases. In case of cooling rate, 0.1 K/ps, an instant growth of nucleation have found at around 570 to 550K. The number of atoms belongs to fcc crystal increases very rapidly and simultaneously amorphous atoms decreases, which indicates that crystal nucleation and growth occurs at around 570 to 550K. However, atom belongs in bcc, hcp, and ico an appearing during nucleation but as the crystal grows, these atoms have disappeared. But, in case of cooling rate, 1K/ps, gradual growth of crystal have found at around temperature, 530 to 480 K. The atoms belong in fcc and hcp increases gradually as temperature decreases, simultaneously amorphous atom gradually decreases. In case of very rapid cooling rate, 10K/ps, atoms belong to fcc, bcc, hcp and ico are very minor and fluctuate near zero as shown in figure 4c.

(a) 0.1K/ps

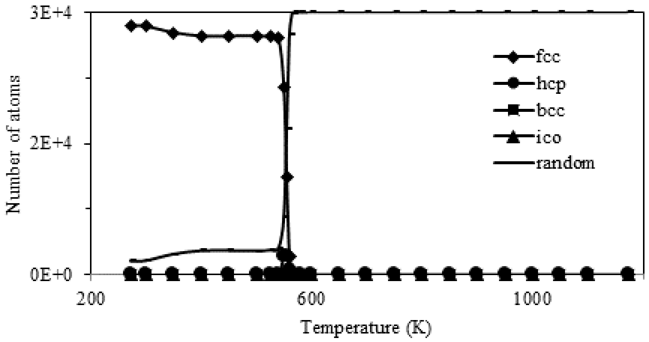

(b) 1K/ps

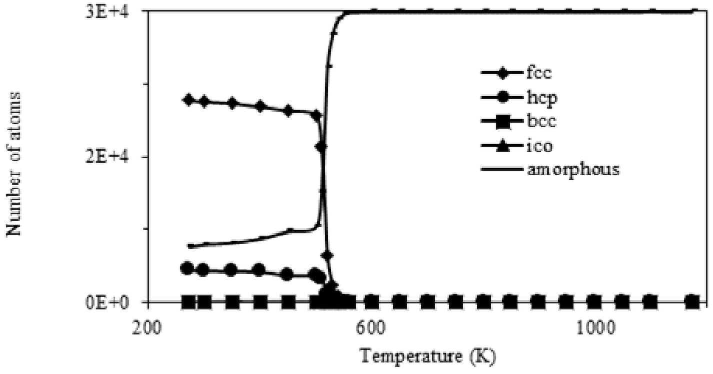

(c) 10K/ps

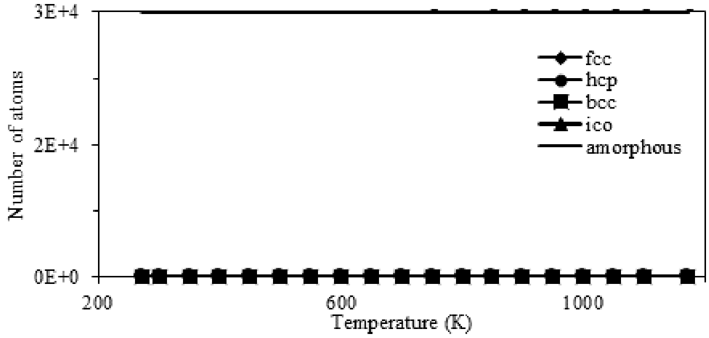

Figure 4 number of atoms belong to different crystal packing are plotted during cooling at various cooling rates: (a) 0.1K/ps, (b) 1K/ps and (c) 10K/ps.

Global bond order parameter

The bond-orientational order parameters *Q*4, *Q*6, *W*4, and *W*6, used to characterize the crystalinity of aluminium by quantitatively during rapid solidification of aluminium as given in figure 5. The numerical value of *Q*4, *Q*6, *W*4, and *W*6 at temperature 273K and cooling rate 0.1K/ps from our simulations are consistent with the standard values as given in table II. Figure 5 shows the variation of *Q*4 and *Q*6 during solidification at various cooling rates. The numerical values of *Q*4 and *Q*6 remain roughly constant at around zero during cooling from 1173K to nearly 580K. Further cooling, results sharp increament in numerical value of *Q*4 and *Q*6 for cooling rate 0.1 and 1K/ps indicate that atoms organization changes from amorphous to crystalline. In case of cooling rate 10K/ps, the value of both *Q*4 and *Q*6 remains constant near zero throughout the cooling process due to the metastable amorphous organization. Thus the bond-orientational order parameters give a good signature of the melting transition.

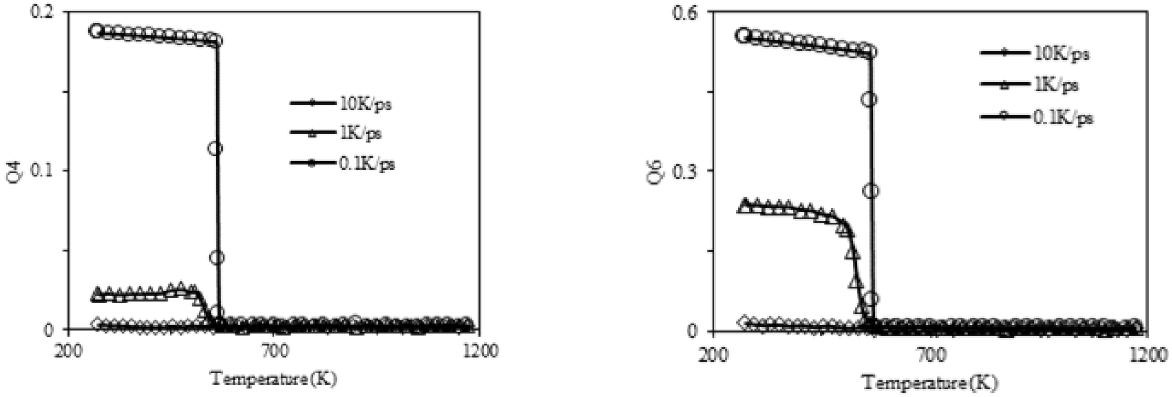

Figure 5 The variation of bond-orientation order parameters during solidification of aluminum at different cooling rate (a) Q4 and (b) Q6.

Crystal defect

The dislocation extraction algorithm (DXA) [50-52] has used to characterize the crystal defect in atomic simulations. It can identify crystal defects by continuous lines and determines their Burgers vectors. As the first step of this method, the crystal defect regions are characterized through the common neighbor analysis (I) method. By this method, an interface mesh is built which distinguishes the crystalline atoms from the disordered ones as shown in figure 6. On this interface mesh, a Burgers circuit is constructed for each defect. In case for high cooling rate, 10K/ps, aluminium structure do not form a crystal structure as given in figure 1. For cooling rate 0.1K/ps, at the stage of nucleation, many crystal defects are found but as simulation proceeds and temperature decreases, crystal defect slowly disappears as shown in figure 6 (a). In case of cooling rate 1K/ps, crystal defects have seen in very early stage of nucleation but these defects grow continuously as temperature decreases as shown in figure 6 b.

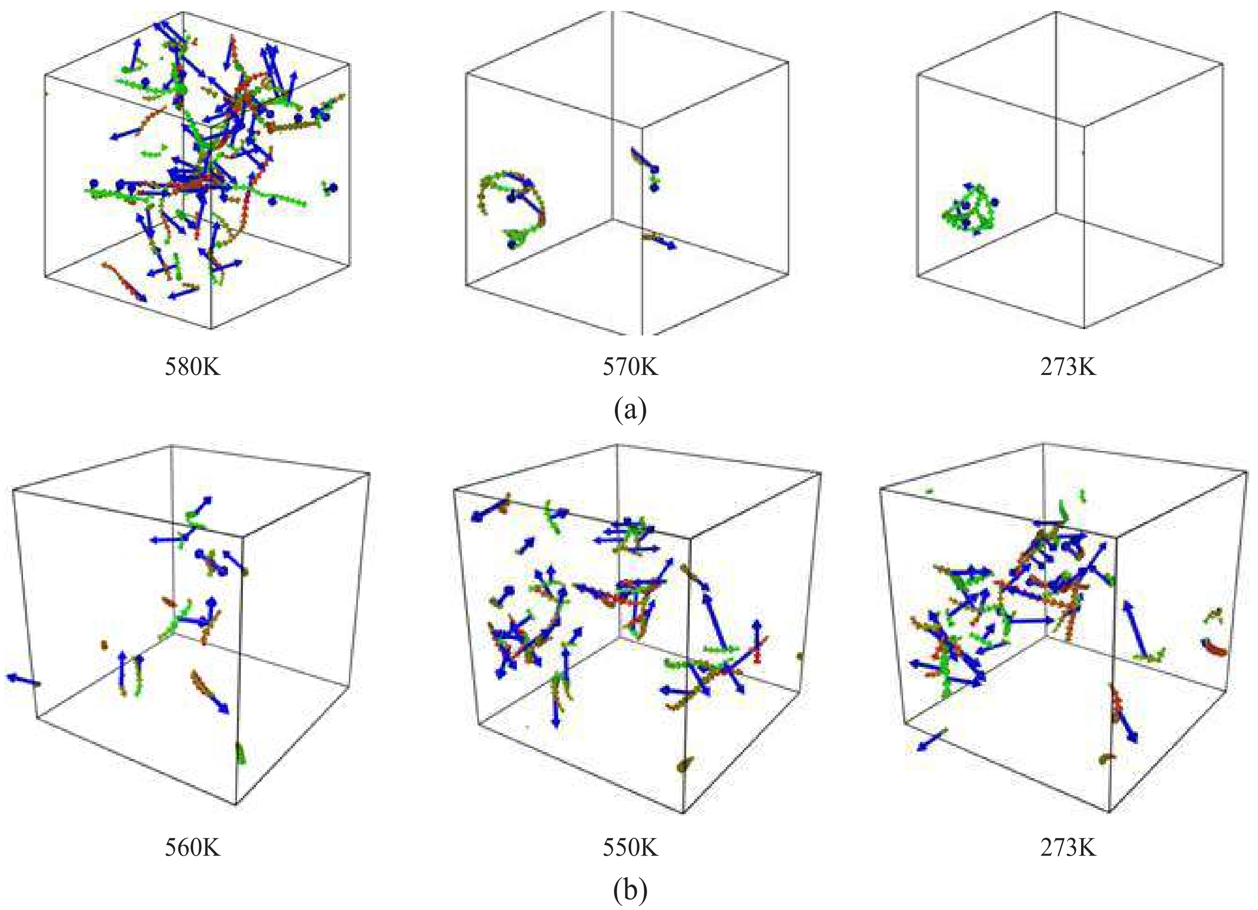
580K 570K 273K

(a)

560K 550K 273K

(b)

Figure 6 Detection of crystal defect by burger vector during solidification from 1173K to 273K at a different cooling rate: (a) 0.1K/ps and (b) 1K/ps. Screw and edge dislocation are indicated by red and green colors respectively. Blue arrow indicates the burger vector and it is perpendicular to dislocation.

3.2. ***Thermodynamic analysis of crystal formation during solidification***

Cooling rate controls the mobility and thermal vibrations of aluminium metal which facilitate close packing of atoms and create clusters of atoms with the low energy region as shown in figure 7. The low energy region act as nuclei for crystal growth. As temperature decreases these nuclei grow rapidly and form a long range ordered structures. In figure 7, low and high potential energy atoms are shown in dark red and blue spheres respectively. At high temperature 1173 to 580, the aluminium atoms are in amorphous state with high potential energy as indicated by blue spheres, but as the system further cools, atoms looses potential energy as indicated by red spheres. The aggregation of low energy spheres creates a nucleation region and its growth leads to the formation of long range ordered structure.

The formation and growth of nucleation region, strongly depends on the cooling rate. The snapshot of the potential energy distribution of various cooling rates is shown in figure 7 (a-d). In case of high cooling rate 10K/ps and 5K/ps, a large number of aluminium atoms reached in a low energy state as shown in randomly distributed dark red colored spheres in figure 7 (a) and (b). However, due to very rapid cooling, the atoms are kinetically traps in meta-stable state and unable to form any cluster for crystal nucleation. In case of high cooling rate 1K/ps and 0.1K/ps, a large number of aluminium atoms reached in a low energy state and subsequently aggregates and form a cluster of atoms which act as crystal nucleation as shown in figure 7 (c) and (d). As the system temperature goes down, size of cluster grow very rapidly and form a long range ordered structures.

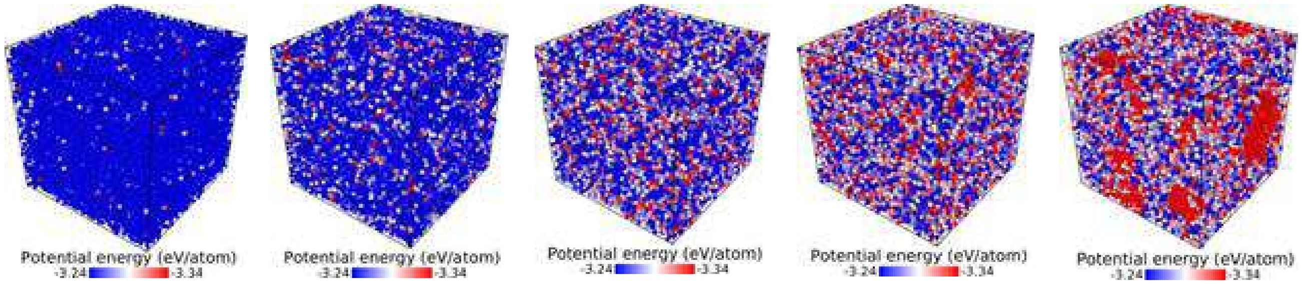

1173 600K 500K 400K 273K

(a) 10K/ps

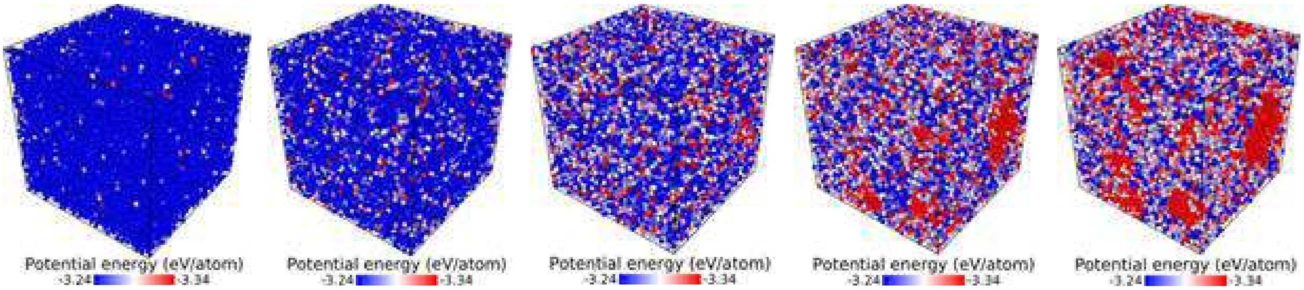

1173K 600K 500K 400K 273K

(b) 5K/ps

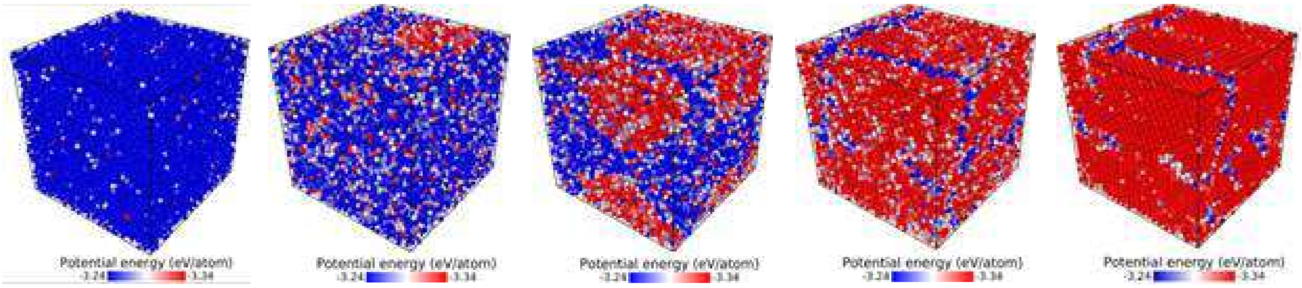

1173K 560K 550K 500K 273K

(c) 1kps

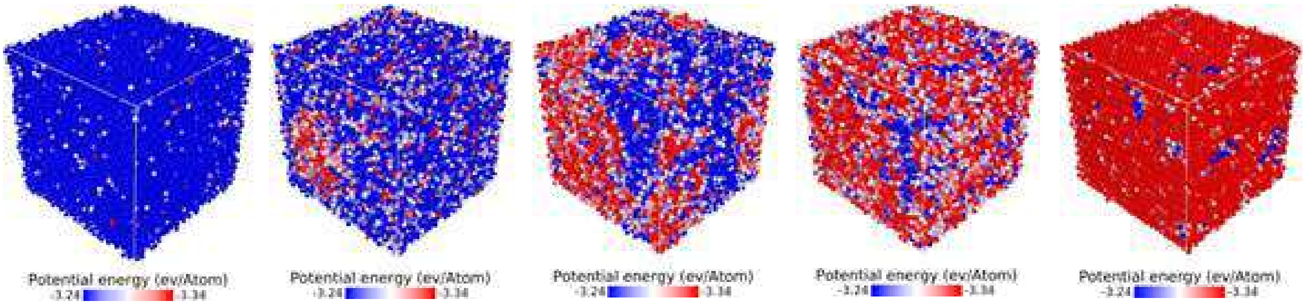

1173K 580K 560K 550K 273K

(d) 0.1K/ps

Figure 7 Potential energy evolution of each atom at various cooling rates (a) 10K/ps, (b) 5K/ps, (c) 1K/ps and (d) 0.1K/ps,

Average energy

Figure 8 and 9 shows the effect of cooling rate on the potential energy per atom during the solidification process of aluminium. The potential energy of aluminium linearly decreases with the decrease in temperature for the amorphous state for highest cooling 10K/ps. Meanwhile, potential energy of aluminium atoms for slower cooling rate, gradually deviate from the linear relationship with temperature at around 650K due to crystal nucleation and growth at cooling rate < 5K/ps. The temperature of nucleation and its growth where the potential energy begins to sharply decrease, increases with the decrease in the cooling rate. The effect of cooling rate on the energy curve appears only after the nucleation of crystal. At 273K, the energies of solidification of aluminium at different cooling rates do not reach the same value. The low potential energy of aluminium atom found at a very slow cooling rate.

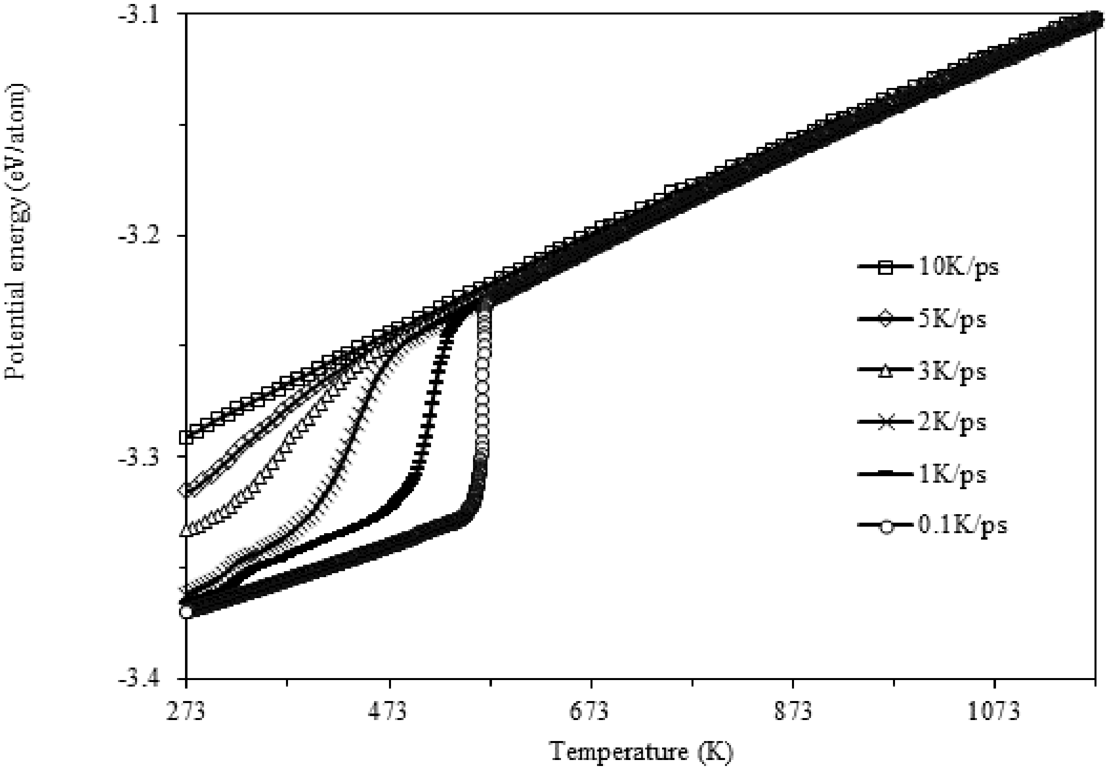

Figure 8 Effect of temperature on the potential energy of aluminium atoms during solidification at various cooling rates.

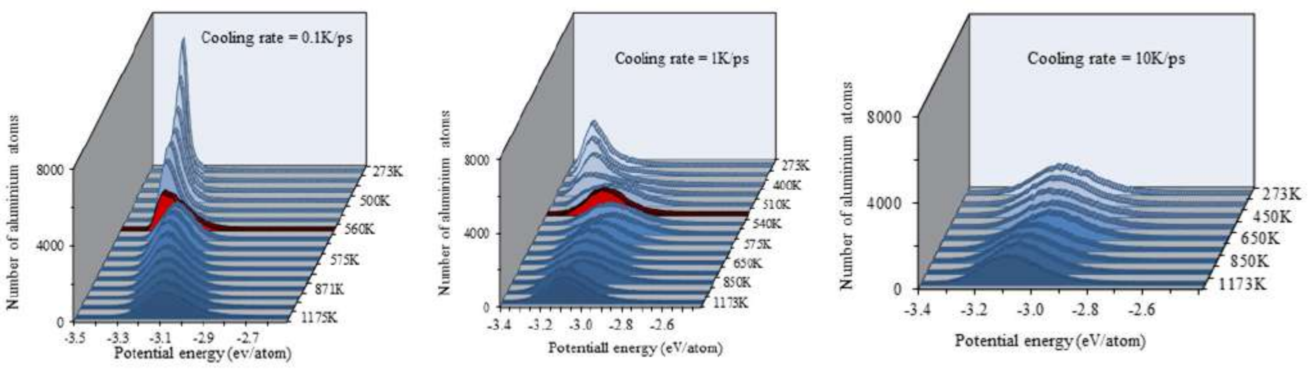

(a) (b) (c)

Figure 9 Potential energy distribution of aluminium atoms during solidification at various cooling rates: (a) 0.1K/ps, (b) 1K/ps and (c) 0.1K/ps. Red colored histogram indicates the early stage of nucleation during crystal growth.

3.3. Dynamics of solidification process

The dynamics of the system has been studied using mean square displacement (MSD) of the aluminum atoms is shown in Figure 10. The MSD at a cooling rate of 0.1K/ps is expressively higher than the MSD at a cooling rate of 1 and 10K/ps, indicating the thermal motion and rearrangements of the atoms is higher at the lower cooling rates. It is also showing that high thermal motion and rearrangement facilitate crystal nucleation and growth. In contrast, at the comparatively high cooling rates, i.e. 10 K/ps, a metallic glass structure formed due to the less thermal motion and rearrangement of atoms. Nano-scopic motion of aluminium atoms during solidification, such as self diffusion of atoms in liquid state, or diffusion from liquid to crystal surface is quantitavely evaluated through diffusion coefficient. The numerical value of diffusion coefficient of our simulations is found nearly similar to reported experimental data [53] as given in table 2.

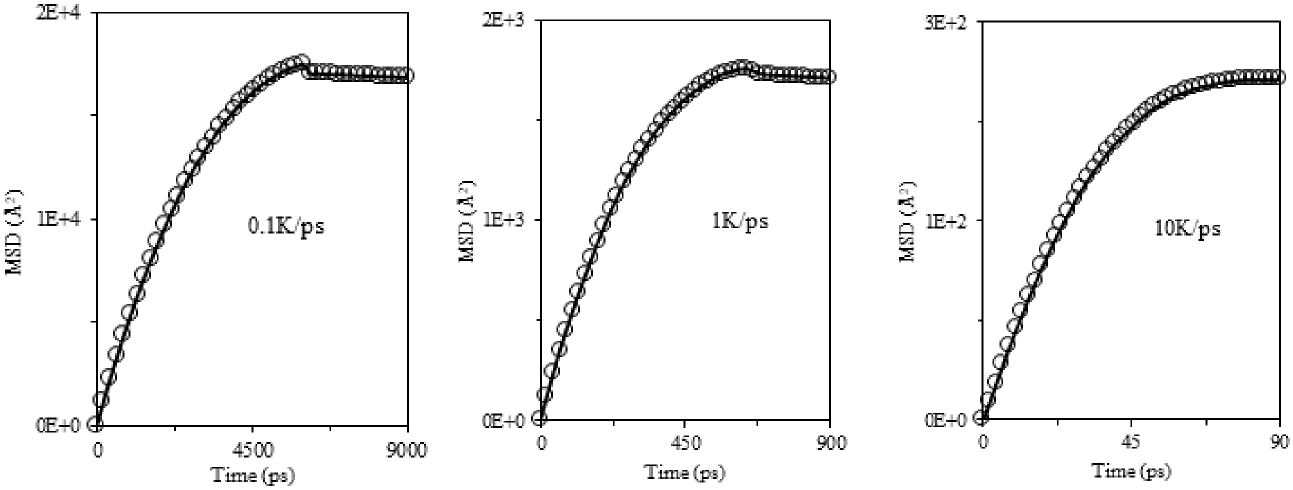

(a) (b) (c)

Figure 10 Mean square displacement of aluminium atoms during solidification at various cooling rates: (a)0.1K/ps, (b) 1K/ps and (c) 10K/ps.

Figure 11 (a-c) shows, the time dependent diffusion coefficient aluminium at different cooling rate. At cooling rate 0.1K/ps, diffusion coefficient decrease as the simulation time increases due to solidification of aluminium atoms, but at the nucleation of crystal it shows sudden drop and then become nearly zero. Sudden drop to a negative value, comes due to attractive nearest-neighbor lattice packing at crystal nucleation and growth. In general, the negative diffusion coefficient is showing the process of increasing concentration or cluster formation as opposed to diffusion. In case of very rapid cooling, the diffusion coefficient gradually decreases as the simulation time increases during solidification which indicates that thermal motion of aluminium atoms slowly decreases and does not involve any structural changes.

Figure 11 (d) shows, the variation of the diffusion coefficient with temperatures during the solidification process at various cooling rates. The plot is indicating that the diffusion coefficient strongly depends on the cooling rate. It is gradually decreasing as temperature decreases for very rapid cooling rate, 10K/ps and not seen any abrupt change. But, in case of 0.1 and 1K/ps, it decreases during cooling and shows a sudden dip at around 550K (for 0.1K/ps) and 510K/ps (for 1 K/ps) due to crystal nucleation.

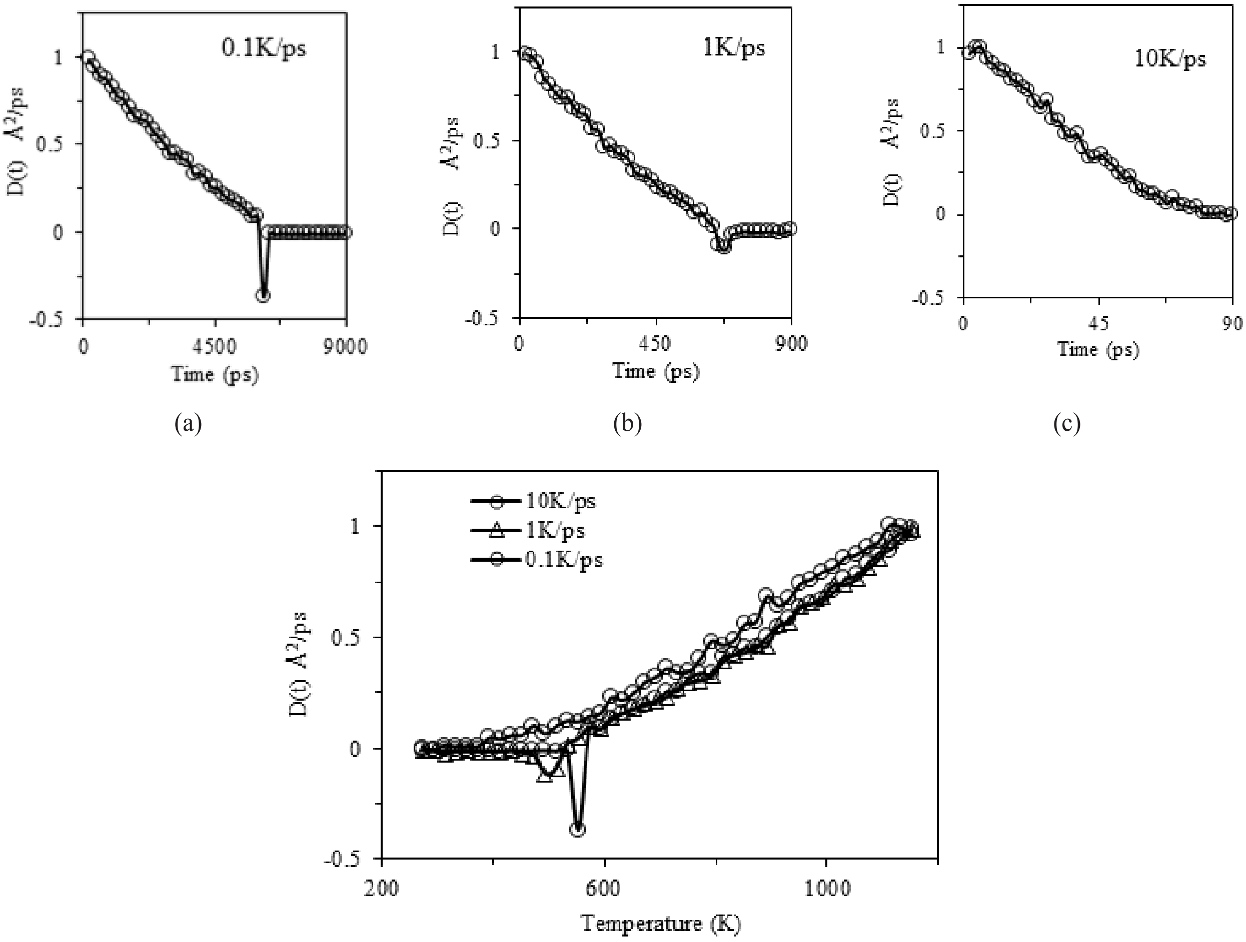

(a) (b) (c)

(d)

Figure 11 Diffusion coefficient of aluminium atoms during solidification at various cooling rates: (a) 0.1K/ps, (b) 1K/ps and (c) 10K/ps and (d) diffusion coefficients vs temperature plot at different cooling rate.

Table 2. Aluminium self-diffusion coefficients measured by MD simulation at cooling rate 0.1K/ps and its comparison with reported experimental data[53].

Temperature (K)	From our MD simulation (cooling rate = 0.1K/ps) ($10^{-9}m^2s^{-1}$)	Reported experimental data ($10^{-9}m^2s^{-1}$)
980	6.45	7.2 ± 0.6
1020	7.03	7.9 ± 0.7
1060	7.76	8.8 ± 0.7

4. CONCLUSION

The MD simulation method has used to explore the effect of cooling rate on the crystal nucleation and its growth. Themodynamic analysis, MSD and diffusion coefficient have used to describe the thermal motion of aluminium. The proportions of locally ordered organization such as fcc, bcc, hcp, etc. of aluminium atoms depend on the cooling rate. For cooling rate 0.1K/ps and 1K/ps (cooling from 1173K to 273K), an fcc crystalline solid aluminium is formed during cooling. But for cooling rate 10K/ps, an amorphous aluminium metal is formed at 273K. The dislocation extraction algorithm (DXA), consists of dislocation of the boundary and Burgers vectors have used to characterize the crystal defect in solidification of aluminium. For cooling rate 0.1K/ps, at the stage of nucleation, many crystal defects are found, but as temperature decreases, crystal defect slowly disappears. In case of cooling rate 1K/ps, crystal defects have seen in very early stage of nucleation but these defects grow continuously as temperature decreases. The thermodynamic analysis behind the origin of crystalline and amorphous aluminium has studied. The face center crystal, fcc, structure of aluminium is a most favorable energy state. Amorphous aluminium is an energetically unfavorable metastable state. Diffusion coefficient decrease as the solidification proceeds, but at the nucleation of crystal, it shows a sudden drop to a negative value and then become nearly zero. Sudden drop to a negative value, comes due to attractive nearest-neighbor lattice packing and crystal nucleation and its growth.

REFERENCE

[1] Y. Birol, Microstructural evolution during annealing of a rapidly solidified Al–12Si alloy. Journal of alloys and compounds 439, 1, 81-86, 2007.

[2] M. Rajabi, M. Vahidi, A. Simchi and P. Davami. Effect of rapid solidification on the microstructure and mechanical properties of hot-pressed Al–20Si–5Fe alloys. Materials Characterization 60, 11, 1370-1381, 2009.

[3] L. Katgerman and F. Dom. Rapidly solidified aluminium alloys by meltspinning. Materials Science and Engineering: A 375, 1212-1216, 2004.

[4] E. Karaköse and M. Keskin. Effect of solidification rate on the microstructure and microhardness of a melt-spun Al–8Si–1Sb alloy. Journal of Alloys and Compounds 479, 1, 230-236, 2009.

[5] O. Uzun, T. Karaaslan, M. Gogebakan and M. Keskin. Hardness and microstructural characteristics of rapidly solidified Al–8–16 wt.% Si alloys. Journal of alloys and compounds 376, 1, 149-157, 2004.

[6] C. L. Xu, H. Y. Wang, F Qiu, Y. F. Yang and Q. C. Jiang. Cooling rate and microstructure of rapidly solidified Al–20wt.% Si alloy. Materials Science and Engineering: A 417, 1, 275-280, 2006.

[7] P. Li, V. I. Nikitin, E. G. Kandalova, and K. V. Nikitin. Effect of melt overheating, cooling and solidification rates on Al–16wt.% Si alloy structure. Materials Science and Engineering: A 332, 1, 371-374, 2002.

[8] C. L. Xu and Q. C. Jiang. Morphologies of primary silicon in hypereutectic Al–Si alloys with melt overheating temperature and cooling rate. Materials Science and Engineering: A 437, 2, 451-455, 2006.

[9] S. P. Nikanorov, M. P. Volkov, V. N. Gurin, Yu A. Burenkov, L. I. Derkachenko, B. K. Kardashev, L. L. Regel and W. R. Wilcox. Structural and mechanical properties of Al–Si alloys obtained by fast cooling of a levitated melt. Materials Science and Engineering: A 390, 1, 63-69, 2005.

[10] G. Antipas, Gas Atomization of Aluminium Melts: Comparison of Analytical Models. Metals 2, 2, 202-210, 2012.

[11] M. Gupta, F. Mohamed and E. Lavernia. The Effect of ceramic reinforcements during spray atomization and codeposition of metal matrix composites: part i. heat transfer. Metallurgical Transactions A 23, 3, 831-843, 1992.

[12] F. T. Wallenberger, N. E. Weston, K. Motzfeldt, and D. G. Swartzfager. Inviscid melt spinning of alumina fibers: chemical jet stabilization. Journal of the American Ceramic Society 75, 3, 629-636, 1992.

[13] M. L. Froberg, Method for preparing molten glass. U.S. Patent 4, 358, 304, issued November 9, 1982.

[14] M. Barth, B. Wei, D. M. Herlach and B. Feuerbacher. Rapid solidification of undercooled nickel-aluminium melts. Materials Science and Engineering: A 178, 1-2, 305-307, 1994.

[15] H. Jones, and C. Suryanarayana. Rapid quenching from the melt: An annotated bibliography 1958–72. Journal of Materials Science 8, 5, 705-753, 1973.

[16] H. Wang, L. Zhou, Y. Zhang, Y. Cai, and J. Zhang. Effects of twin-roll casting process parameters on the microstructure and sheet metal forming behavior of 7050 aluminum alloy. Journal of Materials Processing Technology 233, 186-191, 2016.

[17] N. R. Overman, S. N. Mathaudhu, J. –P. Choi, T. J. Roosendaal, and S. Pitman. Microstructure and mechanical properties of a novel rapidly solidified, high-temperature Al-alloy. Materials Characterization 112, 142-148, 2016.

[19] Z.-Y. Hou, K. Dong, Z. Tian, R. Liu, Z. Wang, and J. Wang. Cooling rate dependence of solidification for liquid aluminium: A large-scale molecular dynamics simulation study. Physical Chemistry Chemical Physics 18, 17461, 2016.

[20] D. M. Herlach, and B. Feuerbacher. Non-equilibrium solidification of undercooled metallic melts. Advances in Space Research 11, 7, 255-262, 1991.

[21] D. Turnbull, Under what conditions can a glass be formed? Contemporary physics 10, 5, 473-488, 1969.

[22] J. Lu and J. A. Szpunar. Molecular-dynamics simulation of rapid solidification of aluminum. Acta metallurgica et materialia 41, 8, 2291-2295, 1993.

[23] C. Kuiying, L. Hongbo, L. Xiaoping, H. Qiyong and H. Zhuangqi. Molecular dynamics simulation of local structure of aluminium and copper in supercooled liquid and solid state by using EAM. Journal of Physics: Condensed Matter 7, 12, 2379, 1995.

[24] C. –S. Liu, Z. –G. Zhu, J. –C. Xia and D.-Y. Sun. Different Cooling Rate Dependences of Different Microstructure Units in Aluminium Glass by Molecular Dynamics Simulation. Chinese Physics Letters 17, 1, 34, 2000.

[25] C. S. Liu, Z. G. Zhu, J. Xia and D. Y. Sun. Cooling rate dependence of structural properties of aluminium during rapid solidification. Journal of Physics: Condensed Matter 13, 9, 1873, 2001.

[26] J. R. Morris, C. Z. Wang, K. M. Ho, and C. T. Chan. Melting line of aluminum from simulations of coexisting phases. Physical Review B 49, 5, 3109, 1994.

[27] A. Sarkar, P. Barat and P. Mukherjee. Molecular dynamics simulation of rapid solidification of aluminum under pressure. International Journal of Modern Physics B 22, 17, 2781-2785, 2008.

[28] S. Solhjoo, A. Simchi and H. Aashuri. Molecular dynamics simulation of melting, solidification and remelting processes of aluminum. Iranian Journal of Science and Technology. Transactions of Mechanical Engineering 36, 1, 13, 2012.

[29] J. Novak, Molecular dynamics simulation of aluminium melting. Materials and Geoenvironment 63, 1, 9-18, 2016.

[30] A. V. Karavaev, V. V. Dremov and T. A. Pravishkina. Precise calculation of melting curves by molecular dynamics. Computational Materials Science 124, 335-343, 2016.

[31] C. S. Hsu, and A. Rahman. Crystal nucleation and growth in liquid rubidium. The Journal of Chemical Physics 70, 11, 5234-5240, 1979.

[32] E. V. Levchenko, A. V. Evteev, I. V. Belova, and G. E. Murch. Molecular dynamics determination of the time–temperature–transformation diagram for crystallization of an undercooled liquid Ni 50 Al 50 alloy. Acta Materialia 59, 16, 6412-6419, 2011.

[33] Y. Shibuta, S. Sakane, T. Takaki and M. Ohno. Submicrometer-scale molecular dynamics simulation of nucleation and solidification from undercooled melt: Linkage between empirical interpretation and atomistic nature. Acta Materialia 105, 328-337, 2016.

[34] Y. J. Lü, M. Chen, H. Yang, and D. Q. Yu. Nucleation of Ni–Fe alloy near the spinodal. Acta Materialia 56, 15, 4022-4027, 2008.

[35] B. Mantisi, Generation of polycrystalline material at the atomic scale. Computational Materials Science 118, 245-250, 2016.

[36] S. Plimpton, Fast parallel algorithms for short-range molecular dynamics,J. Comput. Phys. 117, 1, 1-19, 1995.

[37] W. Humphrey, A. Dalke, K. Schulten, VMD: visual molecular dynamics, J. Mol.Graph. 14 (1), 33-38, 1996.

[38] *A. Stukowski, Visualization and analysis of atomistic simulation data with OVITO – the Open Visualization Tool, Modelling Simul. Mater. Sci. Eng. 18, 015012, 2010.*

[39] M.I. Mendelev, M.J. Kramer, C.A. Becker, and M. Asta, Analysis of semi-empirical interatomic potentials appropriate for simulation of crystalline and liquid Al and Cu, Phil. Mag. 88, 1723-1750, 2008.

[40] L. Verlet, Computer " experiments" on classical fluids. I. Thermodynamical properties of Lennard-Jones molecules. Physical review 159, 1, 98, 1967.

[41] B. G. Levine, J. E. Stone, A. Kohlmeyer, Fast analysis of molecular dynamicstrajectories with graphics processing unit's Radial distribution function histogramming, J. Comput. Phys. 230 (9), 3556-3569, 2011.

[42] Y. Waseda, The structure of non-crystalline materials: liquids and amorphous solids. (1980).

[43] P. J. Steinhardt, D. R. Nelson, and M. Ronchetti. Bond-orientational order in liquids and glasses. Physical Review B 28, 2, 784, 1983.

[44] P. J. Steinhardt, D. R. Nelson, and M. Ronchetti. Icosahedral bond orientational order in supercooled liquids. Physical Review Letters 47, 18, 1297, 1981.

[45] Y. Wang, S. Teitel, and Christoph Dellago. Melting of icosahedral gold nanoclusters from molecular dynamics simulations. The Journal of chemical physics 122, 21, 214722, 2005.

[46] W. Lechner, and Christoph Dellago. Accurate determination of crystal structures based on averaged local bond order parameters. The Journal of chemical physics 129, 11, 114707, 2008.

[47] B. Cichocki, and K. Hinsen. Dynamic computer simulation of concentrated hard sphere suspensions: I. Simulation technique and mean square displacement data. Physica A: Statistical Mechanics and its Applications166, 3, 473-491, 1990.

[48] M. P. Allen, and D. J. Tildesley. Computer simulation of liquids. Oxford university press, (1989).

[49] D. Frenkel, and B. Smit. Understanding molecular simulations: from algorithms to applications. Academic, San Diego (1996).

[50] A. Stukowski, V. V. Bulatov, and A. Arsenlis. Automated identification and indexing of dislocations in crystal interfaces. Modelling and Simulation in Materials Science and Engineering 20, 8, 085007, 2012.

[51] A. Stukowski, Computational analysis methods in atomistic modeling of crystals. Jom 66, 3, 399-407, 2014.

[52] A. Stukowski, and K. Albe. Extracting dislocations and non-dislocation crystal defects from atomistic simulation data. Modelling and Simulation in Materials Science and Engineering 18, 8, 085001, 2010.

[53] F. Kargl, H. Weis, T. Unruh, and A. Meyer. Self diffusion in liquid aluminium. In Journal of Physics: Conference Series 340, 012077, 2012.

[54] V. S.. Krasnikov, A. E. Mayer, and V. V. Pogorelko. Prediction of the shear strength of aluminum with θ phase inclusions based on precipitate statistics, dislocation and molecular dynamics. International Journal of Plasticity 128, 102672, 2020.

[55] N. Gunkelmann, E. M. Bringa, and Y. Rosandi. Molecular dynamics simulations of aluminum foams under tension: influence of oxidation. The Journal of Physical Chemistry C 122, 45, 26243-26250, 2018.

[56] Z. Li, Y. Gao, S. Zhan, H. Fang, Z. Zhang. Molecular dynamics study on temperature and strain rate dependences of mechanical properties of single crystal Al under uniaxial loading. AIP Advances 10, 7, 075321, 2020.

Journal of Metallurgy and Materials Science, Vol. 63, No. 3-4, July-December 2021
Printed in India, © NML, ISSN 0972-4257

Corrosion Protective Graphene Coating : A Mini Review

AYUSHI[1], SHWETA MEHTA[1], MOHIT KUMAR SINGH[1], SWETA SHARMA[2*], RANJAN K. SAHU[1*]
[1] CSIR-National Metallurgical Laboratory, Jamshedpur, 831009, India
[2]Department of Physics, Graduate School and College for Women, Kolhan University, 831001, India

Abstract : Graphene based paint has tremendous potential to protect metal in saline environment, owing to impermeable nature to all corrosive ions. The demand of graphene coating is increasing by leaps and bounds owing to its attractive features. In this review paper, the recent progress of graphene-based paint against corrosion is discussed in details. At the beginning, the corrosion protection mechanisms of metal surface with different types of coating materials such as graphene oxide, reduced graphene, graphene nanoplatelets, and graphene nanocomposite have been presented. In addition, market status of graphene paint and coatings have also been discussed. Subsequently, the discussion has been made on the composition and production protocol of graphene based paint with a special reference to dispersion method. Types of coating in terms of graphene metal matrix composite coatings, graphene polymer matrix composite coatings and graphene composite coatings for corrosion protection of various metal substrates have been reviewed in details with a future outlook.

Keywords *: Corrosion, graphene oxide, reduced graphene, polymers, dispersion, Graphene nanoplatelets*

I. INTRODUCTION

Corrosion is an irreversible and diffusion-controlled process in which metals deteriorate naturally which occurs due to electrochemical or chemical reactions [1]. It is one of the world's most significant challenges [2]. There are various factors that dominate the rate of metal corrosion including metal properties towards contaminated chemicals, concentration and type of pollutants in the atmosphere, temperature, humidity and type of corrosion products. The rate of corrosion in a given environment can be determined thermodynamically using the free energy equation; $\Delta G = -nFE$, where n is the number of electrons involved in the reaction, F is Faraday's constant (F = 96500 C) and E is the electrode potential of metal. Based on the underlying mechanism, most corrosion can be classified into the following forms; uniform corrosion, intergranular corrosion, pitting, selective leaching, crevice corrosion, erosion corrosion, stress cracking and galvanic corrosion. Uniform corrosion is the most common type of corrosion, in which the thickness of metal uniformly gets reduced. Ultimately, the metals fail. Intergranular corrosion is a form of corrosion caused by depletion of elements at and near grain boundary areas. As a result, the cohesive forces between the grains become weak. For example, when stainless steel is heated for a longer time, chromium has dwindled in the grain boundary area resulting in intergranular corrosion. Pitting corrosion is a type of localized corrosion in which pits appear in metals. It is frequently observed in the passive film where small holes or cavities exist. The rate of corrosion accelerates as the damaged area becomes the anode and the passivated area becomes the cathode. Crevice corrosion occurs mainly within crevices and other shielded areas due to concentration differences of ions or dissolved gases between two regions of the same metal section. Erosion corrosion is a natural process that occurs when there is a relative motion between the metal surface and the respective fluid media. It generally occurs in piping. In stress corrosion cracking, small cracks are formed due to the presence of tensile stress and corrosive medium, which propagates normally to the stress. On the other hand, galvanic corrosion is electrochemical corrosion due to dissimilar metals and electric currents. When different kinds of metals are electrically coupled while exposed to an electrolyte, reduction and oxidation occur. The more reactive metal gets corroded. So, the type of corrosion responsible for the deterioration of metal is dependent on the exposure environment and the physical and chemical properties of metals. It may happen that more than one number of mechanisms can also lead to corrosion-driven failure of metals. Therefore, the understanding of different forms of corrosion is very important while developing the corrosion preventive measures of metals.

Corresponding Author :
Email : sweta.shiven@gmail.com;
rksahu@nmlindia.org

To avoid corrosion losses, industries are being paid attention to developing high-performance paints and coatings. As per the report of the World Corrosion Organization, the estimated corrosion-driven damages of steel structures is around $ 2.5 trillion every year, which is 3-4% of the global GDP. Due to corrosion, capital costs are also suffering and also decrease the lifetime of manufacturing equipment [3]. According to a study, corrosion management and corrosion management practices can result in saving 15% - 35% ($375-$875) of the cost of damage globally. In figure-1, different strategies for the protection against corrosion have been given. Corrosion has affected our daily lives directly and indirectly in some other ways. Furniture, metal tools, automobile body panels, etc. are being corroded which causes some amount of loss. In fact, when metals get corroded either it collapses or breakdown which can lead to accidents or even a threat to human life. Further, oil-pipelines break and chemical pipelines leak due to corrosion. Corrosion is also harmful to human health affecting the human digestive tracts, respiratory tracts, eyes and skin, and causes various diseases. The biological system is also adversely affected due to corrosion. When water bodies come in contact with corroded metals and mix with water bodies affects their living. Also, the air becomes polluted. Corrosion also leads to many plants shutting down. Therefore, the massive loss triggered by metal corrosion in industrial sectors is a major challenge. Therefore, corrosion protection measure of metal is useful to prevent financial losses, accidents, various diseases caused due to corrosion and environmental hazards [4]. Corrosion has an obvious effect on the metallic surface, strength, appearance, and efficiency. The economic impact due to the corrosion of metals has stimulated the development of considerable corrosion preventive strategies as metals are used in each field. Among various existing corrosion control strategies protective coatings are gaining popularity around the world due to their ease of production and superior protection. [5-7]. At present day, nanotechnology has introduced nanocoatings, which have a lot of promise in advanced engineering systems. These nanocoatings provide electrically or chemically impermeable coverings on metal surfaces and have customized functionalities such as anti-corrosion, self-repairing, wear and abrasion resistance [8-9]. Rathish et al. has suggested that nano-coatings can increase the effectiveness of protection and create a bulwark against corrosive ions [10]. Adhesion of coatings on the metal surface also plays a crucial role in corrosion shielding. Indeed, epoxy resin coatings are extensively employed due to their flexibility and superior adhesion to a wide range of surfaces. Jiang et al. evaluated the adherence and corrosion resistance of epoxy coatings amalgamated with two types of silane agents, namely, gamma-amino propyl trimethoxy silane and bis-1,2-(triethoxysilyl) ethane. The cross-linkage of epoxy coatings and the chemical bond at the coating and metal interface is effectively reinforced [11-12]. Many reports suggest that the electrochemical reaction rate of nanocoatings is strongly influenced by their grain size. Mishra et al. presented the corrosion activity of nanocrystalline nickel of grain sizes (8–28 nm) and observed that smaller grain size of nickel possessed greater breakdown potential than bigger grain [13]. In addition, the corrosion rate decreased with increasing the grain size.

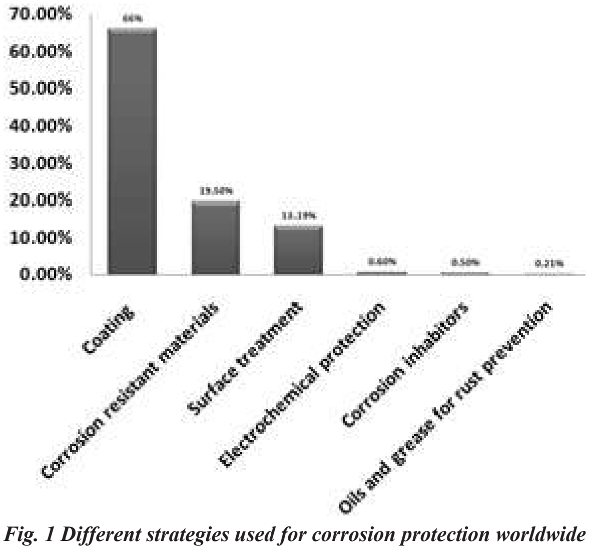

Fig. 1 Different strategies used for corrosion protection worldwide

Currently, several paint formulations have been developed to slow-down the corrosion-driven damages of structural steels. Among them, the paints containing heavy metals (Zn, Chromate or Lead) are efficient barriers for the protection of steel in a highly-corrosive environment. However, these heavy metal based paints are not eco-friendly paints due to the toxic nature of these heavy metals. In contrast, graphene (, an allotrope of carbon) based paint is an ultimate choice for durable rust-preventive coatings due to the following reasons; (a) graphene is impermeable to all the corrosive ions, (b) it improves the mechanical strength and water repelling properties of the coating and (c) it enhances the dissipation of the corrosion-induced current of the coating due to its high-conductivity that becomes harder for the acidic component to attach the steel surface. This review focuses on the usage of graphene for corrosion protection.

2. GRAPHENE : A VERSATILE MATERIAL

In 2004, graphene was discovered for the first time by Andre Geim and Konstantin Novoselov. They were rewarded with a Noble prize in physics in the year 2010 for the discovery of the wonder material. Graphene is a carbon allotrope, a single sheet of sp^2 bonded carbon atom that form a compactly packed hexagonal 2D honeycomb lattice. The sp^2 bonded carbon atoms forms a plane with a molecular bond dimension 0.142 nm. Graphene is exfoliated from graphite (stacked layers of graphene with an interplanar distance of 0.335nm) by disturbing the van der Waals force present in between the graphene layers. Graphene is the sleekest material known to the human world till date. It has unique structural, electrical and mechanical properties which are generally due to 2p orbitals which form πstate bands [14]. It is also light weight material with 1 mm^2 weighing 0.77mg and a high surface area (2630 m^2/gm). Graphene is considered to be the most robust substance known to the world (200 times sturdier than steel) due to its strength, stiffness and toughness caused by the stability of sp^2 bonds. The experimentally evaluated young's modulus is 1TPa with an intrinsic tensile strength of 130GPa and the thickness of graphene is around 0.345 nm. It has high thermal conductivity (5000 W/mK), zero effective mass, impermeable to gases, and high electron mobility (250,000 cm^2/V s at 25^{o}C) [15]. It has a wide range of applications due to its distinctive electronic and thermal properties. Studies have demonstrated that it can conduct current even at zero carrier concentration due to the atomic arrangement of carbon. The valence band and the conduction band merge at a point which is known as Dirac point due to which it is a zero-gap semi-conductor. Graphene used for coating gives a light weight coating and has the ability of resistance to oxidation. Water molecules and diffusion of oxygen on the surface of metals are prevented by graphene by creating a highly tortuous path. Graphene at the metal electrolyte interface also helps to prevent charge transfer [16]. Owing to the outstanding properties of graphene, several methods have been developed for the production of graphene. In table-1, the recent market status of graphene paint and coatings with the involved industries are outlined.

The problem with good quality graphene is that it is expensive. As a result, the price of graphene made of products increases several folds. Therefore, researchers have focused to develop the scalable and cost-effective processes for the production of defect free graphene. Besides, graphene would be suitable for the production of well-dispersed graphene paint. In the recent past, several potential mass production synthesis methods have been developed for the production of graphene. Some notable methods are; the plasma method has been developed for the production of high quality graphene on large scale. The authors demonstrated that the layers from graphite are separated when the high energetic ions hit the surface [17]. Further, Lee et al reported large scale (2 kg / day) continuous production method for reduced graphene oxide (rGO). The produced rGO exhibits electrical conductivity of 660 S /m and a BET surface area of 400 – 600 m^2/g [18].

3. GRAPHENE POTENTIAL AS CORROSION PROTECTIVE COATINGS

Recent past so many materials that are used for corrosion resistance coatings. Compared to these coating materials, graphene paint and coating have higher potential to show corrosion protection in saline environment. Different forms of graphene such as graphene oxide (GO), reduced graphene oxide (rGO), graphene nanoplatelets (GNP) and graphene nanocomposite are being used in the paint and coating. Among them, GO is widely used for corrosion protection in metals. The oxygen groups of GO enhance the bonding of coating with the metal substrate. It is also observed that the performance of polymer coating is improved when the GO is distributed homogeneously. So, the oxygen functional groups become handy to control the interactions through hydrogen bonding in order to agglomeration free graphene sheets. However, the high amount of polar oxygen functional groups such as hydroxyl, epoxy and carboxylic groups can facilitate hydrolysis. Consequently, it shows an adverse impact on the coatings. Therefore, one has to optimize the type and amount of oxygen functional groups of GO while using in the paint and coating for corrosion protection. The oxygen functional groups become useful for grafting with organic and inorganic polymers. In the recent past, there are many reports that demonstrated grafting of GO. Polyacrylate functionalized GO decreased the corrosion rate of epoxy coating almost three times [19]. Again the GO grafted polyaniline filler increases the hydrophobicity that leads to an increase in the corrosion resistance of epoxy coating in saline water [20]. Further, the addition of 0.5 wt.% GO grafted polypyrole filler increases the corrosion resistance of epoxy resin [21]. They have also discussed that the amino functional groups of polypyrole increase the crosslinking density of polymer that leading to a decrease in the micro-pores density. Hence, GO-polypyrole filler enables to increase the barrier effect of coating significantly. Also, tensile toughness is enhanced by the incorporation of GO in epoxy coating. In acidic media, it has a negative charge due to which it is an excellent cation absorbent and smart nanocomposite in the acidic medium as well as anticorrosive layer. This study also suggests that the size of GO sheets determine the barrier property i.e. smaller the sheet, higher the barrier property [22]. Baker et al. studied the size dependent corrosion protection efficiency of GO sheets [23]. Based on the electrochemical impedance data, they argued that smaller graphene oxide sheets have higher activation energy for water diffusion. As a result, the penetration rate of water through the coating containing smaller graphene sheets is significantly reduced.

In addition, reduced graphene oxide (rGO) is also used in the paint for corrosion protection. The rGO sheets are prepared by using suitable reducing agents. Though the reducing agents of GO are efficient to remove the oxygen functional groups, they also produce lots of defects. However, defect free graphene sheets are desirable to achieve high performance of graphene paints and coatings. Hydrazine, hydrogen iodide and ascorbic acid are widely used reducing agents for the preparation of rGO chemically. Some researchers reported that hydrogen iodide produces low defect density rGO sheets. Su et al. reported that rGO film produced using hydrogen iodide reducing agent is an efficient barrier to all gases, liquids and aggressive chemicals including hydrogen flouride [24]. They explained that the reducing agent converts the oxygen functional groups into H_2O, therefore, no structural damage occurs during the reduction. The thermal reduction also transforms GO to rGO. A mild amount of rGO was added to polyurethane (PU) matrix which leads to good physical barrier to corrosion [25]. Researchers also used MoS_2-rGO composite modified with propytrimethoxysilane and MoS_2-rGO/epoxy composite coating for corrosion

Table-I Recent market status of different companies using graphene

Company	Country	Product
Applied Graphene Materials	U.K.	Graphene incorporated water based coatings
The Sixth Element Materials	China	Graphene-Zinc based primer
Graphenano	Spain	Graphene based paints
Talga Resources Ltd	Australia	Graphene coating
The British Electro Conductive Products	U. K.	Graphene based conductive coating
Garmor Inc.	United states	Graphene oxide based coatings
Rusgraphene	Russia	Graphene - epoxy based paints
Tata Steel	India	Graphene paints
Global Graphene Group	United states	Graaphene coating
Nanoxplore	Canada	Graphene based paint

protection applications [26]. Graphene nanoplatelets (GNP) are another form of graphene is made up of tiny heaps of graphene sheets and has 3-10 nm thickness. These graphene nanoplatelets have dimensions of about 100 nm to 100 microns. These GNP's have more than 99 % of carbon content and oxygen content is less than 1%. These GNPs help in decreased permeability and also decreases the diffusion coefficient which is helpful in various applications. X. Cao et al. used GNPs in zinc rich epoxy coating for better corrosion barrier performance. It acts as an oxygen and hydrogen barrier and helps in good electrical conductivity of the coatings on a steel substrate. The Zn-GNP-Zn network acts as better anode corrosion prevention [27]. Graphene based nanocomposites limit the rate of gas diffusion at the metal coating interface. Thus, reduces the cathodic oxygen reduction rate and also reduces the vertical oxygen diffusion. Kirkland et al. revealed the theory in accordant with the diffusion hindering effects of graphene based nanocomposites in composite layers [28]. Yu et al. described that graphene-based polyaniline can provide corrosion protection as it behaves as a gas barrier [29]. The integration of a unique 2D structure with polymer matrix also makes the coating a desirable platform for preventing corrosion, mechanical wear and abrasion, heat or radiation loss, fouling, and bacterial infection [30-31].

Graphene has been also explored for corrosion protection film in biological environments. W. Zhang et al has shown astounding results of graphene coated Cu foils implanted in living body for corrosion inhibition. The cell viability test results demonstrate the effective performance of graphene in reducing the toxicity of Cu by corrosion inhibition [32]. Graphene based thin films have been also reported to provide a protecting layer while functioning as lubricants to minimize surface wear by getting adsorbed by the frictional surface. [33]. Its stability is the reason for it working as an excellent anti-oxide and anti-corrosion layer on metal surface. Graphene used for coating gives a light weight coating and has the ability of resistance to oxidation. Water molecules and the diffusion of oxygen on the surface of metals are inhibited by graphene by creating a highly tortuous path. It acts as a blocking shield on the metal surface to the passing of gas molecules. The hexagonal 2D structure of graphene is an important aspect of the impermeability of other molecules [34]. There are various corrosion protection mechanisms like barrier protection, sacrificial protection, electrolytic inhibition, anodic passivation, etc. based on which the anticorrosive coatings are categorized. Graphene and its derivative based coatings are classified as barrier protective coating because the exfoliation of graphene sheets is a mandatory procedure in forming films over the metal surface. In the barrier protection mechanism, the coating acts as a shield at the coating - substrate interface and restrain the passage of electrolytic ions into the metal. The degree of dispersion of graphene sheets plays a vital role. When the graphene sheets are well suspended in the matrix it acts as an efficient barrier layer at the interface. But sometimes, the lipophobic nature of the graphene induces corrosion. Therefore, the functionalization of graphene proves to be an important step for the production of efficient barrier coatings. Zheng et al. has shown the difference between barrier protection mechanisms of modified and unmodified reinforced graphene epoxy coatings. When the GO/EP coating was exposed to a corrosive environment, the electrolyte molecule got accumulated at the interface, thereby forming defects that further played the role of diffusion channel. Whereas on incorporating functionalized GO in the epoxy coating, the conversion of hydrophilic GO to lipophilic GO aided in better barrier properties [35]. Ramezanzadeh et al. has explained the corrosion protection mechanism of covalently grafted GO sheets with polyimide (PI) chains. The functionalization of the binding sites on GO with PI upgraded the interfacial interactions among graphene sheets and PU matrix. The interpolated PI–GO sheets boost the tortuosity in the path of electrolyte. Along with the coating-substrate interface the PI–GO layers deterrent the diffusion of electrolytes through the parallel directions among local anodes and cathodes [36].

Various factors like adhesion, wettability, electrochemical parameters have an impact on corrosion protection properties of graphene coatings in many ways. Many papers discussed the dependence of corrosion protection of graphene coatings on bonding to the metal surface. Abakah et al. has claimed better adhesion of graphene nanoplatelets incorporated epoxy coatings than neat epoxy coating with 9.6% coating loss in pull-off test studies. Adhesion of coating to a substrate determines the strength of the coating [37]. Water absorption on the coating surface implies poor corrosion protection ability. Water uptake can be measured by two methods namely the gravimetric technique (weight variation on exposure to atmosphere) and capacitive technique (change in electrical capacitance over long-term exposure to aqueous environment) [38]. Aneja et al have recorded that the addition of graphene drops the water uptake. Decreasing the amount of water absorbed is an indicator of the ability of a graphene-modified coating to provide a tortuous path [39] or industrial application the motto is to obtain defect free coating. The pore resistance is inversely related to defect concentration. Zhou et al. found in their electrochemical studies that graphene/epoxy coatings with high pore resistance (1.21×10^6 Ωcm^2) have low defects which enhances corrosion protection potential [40]. Coating capacitance is a measure of determining defects in the coating surface. Defect-free coatings are highly protective. Aneja et al. reported high conductivity (5 Sm^{-1}) of graphene coating which may also offer an alternate path for ions, discharged at the anode to travel, thereby delaying the overall corrosion process. [41]. In coatings usually, cracks are induced and move through the grain boundaries. However, graphene incorporated coatings have the least amount of cracks due to the layered structure. Graphene structure in a coating depends on its dispersion in the matrix chosen. The next section briefly describes the dispersion of graphene in various ways.

4. METHODS FOR DISPERSION OF GRAPHENE IN MATRIX

Graphene has very good chemical, physical and barrier properties, but it has a very low dispersibility. Thus, for widening its application in various fields, the problem of dispersibility is solved. Different ways are used for the dispersibility of graphene are: physical dispersion methods, covalent bonding methods and non-covalent bonding methods [42]. Some tips must be followed for dispersion methods which are: (a) the type, position, and amount of the binding materials on graphene needs to be controlled, (b) the processing effect on matrix materials and graphene must be minimized, (c) unwanted components must be removed and (d) should be cost-effective for large scale production.

4.1 Physical dispersion methods

For even distribution of graphene to obtain anti-corrosion coating, it is mixed in steps and then blended. Fig 6 briefs the exfoliation of graphite to obtain graphene sheets through various ways. The polymerization method is used in which graphene is added with the monomer of resin. The dispersion methods include unmodified simple mechanical dispersion and conventional wet transfer dispersion. Stirring or ultrasound is used in the conventional mechanical dispersion route to disperse graphene directly, without any modification, but this showed difficulty in compatibility. However, this method is acceptable for graphene oxide [43] and could be used for corrosion prohibiting coatings, as the carboxyl and epoxy groups are present on the surface. Chang et al. explained that due to the principle of impermissibility and similarity, the resins having the same functional groups owns compatibility with the oxidation groups and carboxyl. In unmodified wet transfer dispersion, firstly, the graphene is dispersed in water. After dispersing graphene in water, with the help of extraction and evaporation, it is then transferred to resin. [44] In the case of GO, with the help of the wet transfer method, it is extracted directly from aqueous dispersion into epoxy resin. The extraction process is done by the addition of triglycidyl-p-amino-phenol to bisphenol-A epoxy resin. In the formation of a graphene/epoxy dispersion system, phase transfer agents simplify the stages of agitation, temperature, and energy consumption. This method is stable in dispersion and very less time consuming [45].

4.2 Covalent bonding methods

This method of dispersion is most widely used at present as it is carried out by using 3 aspects of small organic molecules, polymers, and inorganic nano-oxides. Using small organic molecules, graphene is modified by mixing oxygen containing groups and small organic molecules. The organic molecules include silane coupling agents, titanite coupling agents, isocyanate, thionyl chloride, etc. This takes place with the help of covalent interactions on the surface of GO. The silane coupling agent (EPTES), forms Si-OH bonds on decomposition. EPTES, on the surface of graphene, is covalently bonded to an active oxidation site. EPTES modified GO along with epoxy resin shows improved compatibility as a number of epoxy groups of EPTES is directly proportional to compatibility modified graphene/epoxy resin, which leads to good dispersion results [46]. Titanate coupling agent also used to modify graphene, showed excellent stability in aqueous dispersion for several weeks. GO, GO-Ti and Nano-Ti particles could be dispersed in epoxy resin using ultrasonic dispersion [47]. Li et al. explained that the coating, with waterborne polyurethane shows good barrier properties for corrosion protection [48]. At present, the dispersion of graphene using polymers is more considerable. In polymers, its structural parameters can be altered which helps the graphene by providing useful properties. The properties include ductility, toughness, etc. by altering the function and type of the polymer [49]. In epoxy resins, the polymers which can be used for dispersion include polyaniline, polyvinylpyrrolidone by mechanical stirring, and aniline trimmer. Fully-oxidized polyaniline was used to modify GO. After that modified GO, with the help of mechanical stirring was dispersed in polyvinyl butyral resin uniformly [50]. Graphene modified with polyvinylpyrrolidone is dispersed in epoxy resin. This enhances the anti-corrosion ability of epoxy resin with good adhesion. The mechanical and thermal property of epoxy resin coating is enhanced which is useful for corrosion protection [51]. GO surface modified with sulfonated aniline trimmer (sulfonated with 3-aminobenzenesulfonic acid) was dispersed in epoxy resin. Sulfonated aniline trimmer and graphene oxide have a synergistic effect and this makes the dispersion easy. The solvent property of sulfonated aniline trimmer shows excellent compatibility with epoxy resin and enhances the anti-corrosion ability of epoxy resin coating. [52] Yu et al. explained that dispersion of graphene oxide is enhanced by the formation of a chemical bond between vinyl-grafted graphene oxide and styrene monomer in a polystyrene matrix. This material was used for corrosion protection coating and it enhanced the anti-corrosion ability. He also discussed about the graphene sheets which were water dispersible. Carboxylatedoligoanilines were used to stabilize these graphene sheets. These were used for corrosion protection coatings [53]. Yeh et al. reported that polyaniline with graphene used for coating leads to excellent corrosion protection. Better dispersion of graphite was shown by 4-aminobenzoyl group functionalized graphene sheets [54]. The use of inorganic nano-oxides for dispersion of graphene for corrosion protection coating is also considered a promising method. Chemical bonding takes place for modification GO with inorganic nano-oxides. GO-Al_2O_3 hybrid with epoxy shows excellent corrosion barrier property. 3-aminopropyltriethoxysilane is used to anchor Al_2O_3 on GO sheets and then the GO-Al_2O_3 hybrid was dispersed in epoxy matrix. It was dispersed uniformly in epoxy resin [55]. TiO_2-GO hybrids dispersed in epoxy resins show anti-corrosion properties. TiO_2, with help of (3-aminopropyl) trimethoxysilane (APTS) was synthesized on graphene oxide sheets and was dispersed in the epoxy resin [55]. SiO_2 is anchored with the help of 3-glycidoxypropyltrimethoxysialne and 3-aminopropyltriethoxysilane on GO sheets. Then, this SiO_2/GO is dispersed into epoxy resin and this showed enhanced corrosion protection ability [56]. Graphene is modified with 4-aminobenzoic acid and then a covalent bonding, as well as polymerization takes place with the aniline monomer to form graphene/polyaniline. This graphene/polyaniline is used for coating as it acts as a barrier for oxygen and water, hence acts as an excellent corrosion protective barrier [57].

4.3 Non-covalent bonding methods

Dispersion of graphene also becomes stable by modifying the surface with the help of non-covalent bonding methods such as π-π interactions, ionic bonding, and hydrogen bonding. Li et al. described Ionic bonding help the graphene oxide to dissolve in water, as there is a negative charge in the surface carbonyl of graphene oxide. Thus, a stable colloidal solution is formed due to the repulsion of negative charges. Thus, by controlling the reduction process, carboxyl ions are retained and get good dispersion of graphene in water [58]. Electrostatic adsorption was used to disperse GO in the aluminium powder and anionic surfactant without the use of any chemical catalysts. Then, with the help of sintering method, GO/Al_2O_3 composite was prepared. Then, graphene was mixed with the sodium polyacrylate (anionic surfactant) and this mixture showed an excellent dispersion in water and can be used in water-borne epoxy coatings [59]. Dispersion of graphene can also be done by π-π non-covalent interactions. π-π non-covalent interactions give excellent dispersibility of graphene with the same conjugated structure. It absorbs the organic molecules on the graphene surfaces. Molecules that have conjugated structures with the plane and aromatic rings have good dispersion of graphene. Hence, these graphene-based epoxy coatings also show good anti-corrosion properties. Poly (2-butylaniline), a dispersing agent, was immersed on the graphene surface. Then P2BA was mixed with graphene and ultrasonicated. A stable dispersion was obtained due to non-covalent π-π interactions between graphene sheets and P2BA. Then, by curing the reaction of P2BA/GO, epoxy resin, and amine hardener, graphene sheets were integrated with the coating matrix. [60] Corrosion protection property of epoxy coating, with 3, 4, 9, 10-perylene tetracarboxylic acid and graphene is enhanced. PTGA was added to graphene and ultrasonicated. Due to π-π interactions between PTGA and graphene, PTGA was absorbed on the graphene surface and showed good dispersion of modified graphene in epoxy resin [61]. Iqbal et al. explained the dispersion of graphene in polyethylene. Polyethylene, graphene, and oxidized polyethylene with the help of the solvent blending method were mixed. Polyethylene was blended with oxidized polyethylene to enhance the dispersion of graphene in polyethylene [62]. Graphene oxide forms hydrogen-bonding interactions with various substances. as a large number of –COOH and -OH groups are present. Therefore, the dispersion of graphene is improved as it does not change the molecular structure. Li et al. using the method of solution blending, dispersed, graphene oxide in thermoplastic polyurethane. Thus, due to the presence of hydrogen bonds, graphene is uniformly distributed on the polyurethane matrix. Then, in-situ thermal reduction method was used to reduce graphene oxide nanosheets in the composites [63]. The surface of graphene oxide was absorbed by the doxorubicin hydrochloride under no light and ultrasonic surroundings. This was mainly due to the existence of the hydroxyl group in graphene oxide and also in the doxorubicin hydrochloride [64]. A highly efficient dispersant, vitamin B_2, namely FMNS (flavin mononucleotide) is used in the preparation of aqueous dispersions of a few layers of graphene flakes which are defect free. FMNS is used for graphene colloidal dispersion and inks. This process is done with the ultrasonic exfoliation of graphite powder. Due to the presence of hydrogen bonding interactions between the graphene and FMNS, a stable dispersion of graphene is observed during the process of ultrasonic stripping of graphene sheets. [65] Chemical plating is one of the dispersion methods in which graphene surface is chemically plated. The surface of graphene is firstly coated by some metals and then combined with other metal matrix. In this process, metal ions are reduced to metal atoms in the solution and deposited on the surface of materials. However, chemical plating cannot be used with every material, only materials which have autocatalytic properties can be chemically plated. Graphene nanoplates do not have catalytic properties. Thus, activation and sensitization are performed. This is the process in which chemical plating is possible in graphene if some catalytical property particles are absorbed on the surface of graphene [66]. Graphene was dispersed in water by stirring and ultrasonication. Using the electroless plating method, containing no reducing agent, Fe and Fe-rGO coatings were formed on Cu substrate. The Fe-rGO coating shows better corrosion protection as it has a dense structure owing to the plating bath in which GO is added [67].

5. TYPES OF GRAPHENE COATING

5.1 Graphene Metal Matrix Composite Coatings

This section is brief about the various graphene reinforced metal matrix composite coatings. Kumar et al. explored the anticorrosive property of Ni and Ni-Gr composite coatings. They suggested that the introduction of graphene in Ni metal matrix affects the crystal growth which leads to a small average crystallite size of 20 nm as compared to 30 nm of pure Ni coating. He explained the mechanism of increasing nucleation growth and reducing crystal growth of Ni at the Ni/Gr has a more positive shift in E_{corr} with lower I_{corr} which shows the corrosion resistance of Ni/G coatings. He also suggested that the insertion of graphene may lead to high mechanical strength and hardness of the composite coating [68]. Nazir and his co-workers also investigated the corrosion behaviour of various nickel matrix-based nanocomposite coatings. Among different metal oxide reinforced nanocomposites, graphene was also used as one of the reinforcing elements in the metal matrix. Graphene platelets were used to disperse in prepared Ni solution and were electrodeposited on steel. They reported that Ni/graphene coatings formed a very fine coating resembling glass with low porosity and least surface roughness. When the prepared coated samples were exposed to an aggressive corrosion environment, they found that in the case of Ni/graphene coatings there was the lowest percentage rise in grain size leading to enhance impermeability to oxygen and electrolyte ions this was confirmed from the obtained corrosion product (0.3wt % Fe) [69]. Srivastava et al. has presented the remarkable results of the incorporation of graphene in Cr metal-based coatings by electrodeposition. They observed that the incorporation of graphene in the CF (Chromium coating containing Zinc-Oxide nanoparticles deposited using formic acid) ensued in improving the topology and surface morphology of bare Chromium coating. In their electrochemical studies, they found that CFG (Chromium coating containing Zinc-Oxide nanoparticles and graphene deposited using formic acid) has a more positive Ecorr value than other CF & C (Cr coating) coatings which explains the inertness of CFG towards corrosive media. Also, they found that the corrosion rate and corrosion current value was lowest with respect to other Cr coatings which support the stability of graphene incorporated Cr coatings. They also suggested further study of the photothermal conversion behaviour of Cr-G coatings [70]. Raghupathy et al. explained the surface modification of Cu-GO coatings on mild steel. The electroplated Cu-GO coatings showed crystal growth along <220> atomic plane. The electrochemical corrosion test verified that with the loading of GO the coating yielded higher corrosion potential. He studied the long-term corrosion resistance property of Cu-GO coatings and found considerable surface change after 5 days of exposure to corrosion media [71].

5.2 Graphene Polymer Matrix Composite Coatings

Many researchers have shown their interest in graphene and its derivative, as a filler material for polymer composites due to the uniqueness of graphene. Already some scientists have claimed the novel properties of graphene incorporated polymer composites for corrosion protection. The uniform distribution of graphene as reinforcement plays a significant role in the production of graphene-based nanocomposites. Graphene used as nanofiller acts as a physical blockade that descends the permeability of polymer-based coatings by extending the tortuosity of the wandering route for particles. Chang et al. illustrated the principle of enhanced corrosion protection of polyaniline/Graphene and polyaniline/clay composite coating on steel. They incorporated functionalized graphene into polyaniline which worked as a gas barrier that retards the penetration of gases like O_2 and H_2O molecules into the coating, thereby protecting the metal surface. K.C. Chang and his fellow workers presented the better corrosion resistance properties of hydrophobic epoxy graphene composites (HEGC) than epoxy / graphene composites. The electrochemical studies of HEGC coatings showed a higher E_{corr} value (-411mV). They demonstrated that 1 wt. % graphene inclusion in epoxy - graphene composite can inhibit up to 60% of O_2 permeability [72]. Pourhashem et al. has presented the importance of dispersion graphene derivative in the matrix for the efficiency of coating over the substrate. They claimed via his electrochemical measurements that the increasing GO content lowers the barrier properties as there is a chance of GO aggregation with higher wt.%. They also suggested that GO directly added hardener has superior dispersion and corrosion resistance properties than GO incorporated in epoxy. Hayatdavoudi et. al. presented the influence of an adequate amount of graphene in Zn-rich epoxy (ZRE) coatings for protection against corrosion. The long-term corrosion studies revealed that the role of graphene content in galvanic coupling corrosion as lower content of graphene act as a cathodic site for sacrificial ZRE coating and increase the percolation period thereby deteriorating the efficiency of the coating against corrosion. Also, in the salt spray test, they noted the formation of white rust in high graphene content ZRE coatings which indicate better protection while there was the formation of red rust in the scribed areas of lower graphene content in ZRE coatings after 1000 hrs of spray test [73]. Zheng et al. has reported the anticorrosion property of modified graphene-based epoxy coating. The graphene was modified using poly- urea formaldehyde via in-situ polycondensation reaction followed by a mixing of epoxy resin. From the characterization results, they proposed that the hydrophilicity of GO no longer existed after the modification. Also, the GO/UF composite acts as a sheet pigment in epoxy. Ramezanzadeh et al. showed in his report, the advanced barrier properties of functionalised GO sheets into Polyurethane coatings. The GO sheets were conjugated with polyisocyanate (PI) resin. They concluded from the obtained SEM images that the PI–GO/PU composite has smooth surface fracture which signifies the reduction of cracks by graphene derivative. Li et al. studied the corrosion protection of different forms of graphene reinforced into waterborne polyurethane (PU) coatings. He found that except functionalized GO (FG), GO and mildly reduced GO (RGO) were well dispersed in PU due to the hydrophilic character of GO. They concluded through his investigations that RGO with low content of 0.2 wt% showed the best anti-corrosion properties in the electrochemical test as well as salt spray test. However, increased content of Functionalized Gr of 0.4 wt% has better resistance than 0.2 wt% Functionalized Gr he expected the reason behind improved properties is due to the parallel alignment of FG to the substrate [74].Other than coating as a corrosion barrier, Graphene paints also attracted researchers to investigate the properties for practical applications. Krishnamoorthy et al. demonstrated the inhibition performance of GO nano paint in an acidic medium by weight loss method in the saline medium. They reported the inhibition efficiency of GO nanopaint to be 88.70% in an acidic atmosphere. The corrosion-resistant efficiency was calculated 76.61% in 3.5 wt% NaCl solution [75].

5.3 Graphene composite coatings for corrosion protection of various metal substrates

Chen et al. has explained the corrosion hindrance ability of graphene for Cu and Cu/Ni alloys. They have reported the chemical inertness of monolayer and bilayer graphene coatings in both air oxidation and liquid solution environment [76]. For the nickel surface coated with graphene acts as an ionic barrier. This decreases the corrosion rate leading to corrosion protection. Ni coated with graphene by chemical vapour deposition, graphene acts as a barrier for electrochemical reactions [77]. There is a mechanism of greater solubility of carbon in nickel and surface catalysis. The graphene coating has great coverage of the surface, has good adhesion and correlation. Also, the Ni surface coated with graphene has very less defects, as a result of which there is high corrosion resistance. When graphene is coated on nickel, the rate of corrosion is 10.45 x 10 $^{-3}$mm/year, corrosion potential -233 mV and corrosion current of 0.85 μA/cm^2 in 0.5 M NaCl. Kumar et al. examined that the corrosion rates become 7 times slower as compared to nickel coating where there are no additives. The preparation route of coating also affects the efficiency of coatings to corrosion barriers. Prasai et al. had presented the difference between the corrosion resistance of graphene-coated Ni formed by mechanical transfer and CVD. They found that CVD-developed coating has 20 times corrosion resistance while few layers of mechanically deposited coating resulted in excellent property [78]. However, there are other methods used for coating prepared graphene composites on metal like rapid thermal annealing, spin coating, electrophoretic deposition, vacuum filtration, powder spray, solution spray, dip coating, brush painting, or drop-casting [79]. Graphene-coated copper has lower corrosion densities and corrosion current dropped by 20 times with respect to bare Cu [80]. The rate of corrosion for graphene-coated copper is observed to be 0.08 mm/year

Table-II. Electrochemical data of some graphene coated metal substrate in 3.5 wt.% NaCl solution

Composite coating	Coating method	Substrate material		Immersion time	Electrochemical parameters				Ref.
					E_{corr}(mV)	**I_{corr} (μA/ cm^2)**	**R_{corr} (mm/y)**	**R_p (KΩ cm^2)**	
G/PANI	Nano-casting	Steel		_	−537	0.38	0.00044	135.22	[54]
GO/isocyanate	Electro deposition	Copper		_	−211	3.49	0.04068	0.025	[91-92]
G/polyimide	Spin coating	Cold rolled steel		30 min	−432	0.15	0.00176	165.29	[93]
G/epoxy	Nano-casting	Cold rolled steel		30 min	−411	0.10	0.00009	442	[73]
GO/per nigraniline	Dip coating	Copper		168 hours	-23	5.98×10^{-5}	6.99×10^{-7}	9.86×10^{5}	[50]
GO/epoxy	Film applicator	Mild steel		240 hrs	−	0.2015	2.366×10^{-3}	1.669	[94]

rGO / diatomaceous earth / TiO_2	Cold spray	Copper		15 min	12.2	0.159	0.00158	_	[79,95]
rGO/epoxy	Spin coating	Zinc		144 hrs	−957	0.18	0.00272	_	[51]
GO/PMMA	Drop casting	Copper		100 hrs	−250	0.069	_	_	[83]
rGO/silicon-acrylate resin	Spin coating	Zinc		144 hrs	−585	0.45	0.00682	_	[96]
G/polyurethane–	Film applicator	Mild steel		_	−27.2	2.45×10^{-5}	2.88×10^{-7}	_	[97]
G/PANI	Electro polymerization	Copper		_	−234	0.1	0.00005	1.5×10^{2}	[98]
GO/chitosan	Dip coating	Carbon steel		48 hrs	−374	3.9	0.0017	1.44	[99]
G/epoxy	Film applicator	Q235 steel		48 hrs	−566	0.0551	0.0007	369.4	[100]
GO–ZrO_2epoxy		P110 steel			–432	0.37			[101]
rGO/PPy	Electrodeposition	Mild steel		1 hr	-544	0.85	0.0099	66.9	[102]

whereas for bare copper it is 0.18 mm/year [81]. Singh Raman et al. described that Cu coated with graphene by CVD was ensured to have improved corrosion resistance by magnitude of two orders. Raman spectroscopy was to determine the number of layers. There are 4-5 layers of graphene on copper films (I_G/I_{2D} ratio = 1.36) [82]. Kalita et al. described that copper coated with graphene provide oxidation resistance for an only a short period of time and inferior corrosion resistance for long period of time [83]. Electrochemical Impedance spectroscopy (EIS) and potentiodynamic polarization is used to study corrosion protection due to graphene. Kirkland et al. had shown in their study, that there was an anodic shift for Ni and cathodic shift for Cu substrate layered with CVD-grown graphene. Coating thickness and exposure to a corrosive environment have an effective impact on the protection tendency of coatings. Qi and co-workers have explained the effect of exposure time and Coating thickness on different concentrations of PMMA-g-GO. They noted that 81% PMMA-g-GO film has better performance than 62% PMMA-g-GO. Also, with the increase in film thickness from 2µm to 10µmthere were no corrosion traces with 10 µm thickness. 81% PMMA-g-GO proved to provide corrosion protection up to 100 hrs [84]. For steel, graphene acts as an ionic barrier. For corrosion protection of mild steel substrate, epoxy-GO nanocomposite coating is used which has enhanced barrier properties. Diffusion of corrosive species is restricted by GO nanosheets in epoxy coating. For enhanced corrosion protection, GO is directly added to polyamide hardener. To deposit GO onto carbon steel, nowadays EPD (electrophoretic deposition) is being used.

The sheets of GO are smooth and clear, have high functionality, and improve adhesion. Park et al. described that GO sheets were inactive as an oxidation barrier because it was less dense [85]. In the case of aluminum, graphene coating served as a barrier layer which was highly protective. Al substrate coated with graphene has corrosion protection efficiency of magnitude order 3 that was higher than bare Al substrate. Graphene coatings by dip coating on the Al surface worked as a barrier between the Al surface and the electrolyte. Lui et al. reported that by Raman spectra it was found that graphene dip-coating covered the Al surface uniformly. XPS analysis described that from graphene dip coatings, oxygen-containing functional groups were removed. [86] Al-2219 alloy was coated with graphene blended PVA. This was done by using multiple dip coating. Hikku et al. reported that there was a uniform coating of GPVA on the Al surface. As compared to bare Al, Al-2219 coated with GPVA showed lower corrosion current, lower corrosion rate, and higher polarization resistance [87]. Chen et al. had represented the corrosion protection ability of graphene-coated Cu and Cu-Ni alloys when exposed to high temperatures. They claimed that multilayer graphene act as passivation coating for a short time period. They found that the multi-layered graphene-coated Cu/Ni alloy samples remained shiny even after two days in air at the 200°C. Meanwhile, iron is considered the most active metal for corrosion. Bare iron easily turns brown when exposed to harsh conditions due to oxide layer formation over its surface. Kang and his co-workers have confirmed that the colour of five bilayer rGO coated iron foil does not change even in oxidation conditions [88] Gan et al. reported that further research is required for the protection mechanism of graphene composite coatings [89]. Bohm et al. discussed that steel coated with graphene has corrosion rates of 0.000196 mm/year as compared to bare graphene which had a corrosion rate of 0.7 mm/year. Galvanized steel had corrosion rate of $3.87*10^{-2}$ mm/year whereas 20% wt.% unfunctionalized graphene had corrosion rate of $8.46*\ 10^{-4}$mm/year [90]. Table 3 shows graphene-based coating on different substrates.

6. FUTURE OUTLOOKS FOR CORROSION PROTECTION USING GRAPHENE

Researchers are working on graphene paints for corrosion protection and have demonstrated that in the future graphene paints can be used to protect steel and other metals in corrosive atmosphere. In the future graphene will have greater progress as much researches is going on for the improvement of defects and to make perfect graphene that gets evenly spread in the polymer resin. The key element that diminishes the competence of graphene for various applications is the number of defects. It is found crucial to achieve defect-free, ordered arrangement of graphene, and develop environment-friendly modification methods for the original structure of graphene which are not harmful to human health as well as the environment, the amount of graphene domain boundaries is to be reduced thereby producing sheets of a larger area. Graphene waterborne anti-corrosive coatings are also given attention for the future. The main global goal is to make graphene useful for commercial products in society and in the market. In the next 10 years, it is believed to achieve this goal and benefit society with the astonishing properties of graphene.

7. CONCLUSIONS

Graphene coating is regarded as an ultra-thin coating that protects the metal from oxygen and water by providing a good shielding. It is also regarded as an eco-friendly coating free from any hazardous chemicals. Compared to ceramic coating graphene is always better in terms of its durability, hydrophobicity, glossy, and it's easy to apply, still, the challenges for its application as effective material against corrosion lies in terms of its high cost. Researchers are working in this area to make this material less cost-effective by devising various new synthesis techniques.

REFERENCES

[1] E.M. Fayyad, K.S. Kishor, P. Deepalekshmi, A.M. Mariam,Oleic acid-grafted chitosan/graphene oxide composite coating for corrosion protection of carbon steel. Carbohydrate Polymers 151, 871-878, 2016.

[2] E. Bakhshandeh, A. Jannesari, Z. Ranjbar, S. Sobhani, M. R. Saeb:Anti-corrosion hybrid coatings based on epoxy–silica nano-composites: toward relationship between the morphology and EIS data. Prog Org Coat 77, 1169-1183, 2014.

[3] The Effects and Economic Impact of Corrosion Corrosion: understanding the basics.ASM International, 2000.

[4] Gurrappa, I. V. S. Yashwanth:The Importance of Corrosion and the Necessity of Applying Intelligent Coatings for Its Control In: Intelligent Coatings for Corrosion Control. Butterworth-Heinemann 7-58, 2015.

[5] D. Wang, G. R. Bierwagen:Sol-gel coatings on metals for corrosion protection.Prog Org Coat 64, 327-338, 2009.

[6] C. T. J. Low, R. G. A. Wills, F. C. Walsh:Electrodeposition of composite coatings containing nanoparticles in a metal deposit. Surf Coat Tech 201, 371-383, 2006.

[7] J. E. Gray, B. Luan: Protective coatings on magnesium and its alloys – a critical review. Jour Alloys Compd 336, 88-113, 2002.

[8] E. M. Fayyad, M. A. Almaadeed, A. Jones, A. M. Abdulla:Evaluation techniques for the corrosion resistance of self-healing coatings. Int Jour ElectrochemSci 9, 4989-5011, 2014.

[9] L. Bamoulid, M. T. Maurette, D. D. Caro, A. Guenbour, A.Ben Bachir, L. Aries, S.E. Hajjaji, F.Benoît-Marquié, F. Ansart:An efficient protection of stainless steel against corrosion: Combination of a conversion layer and titanium dioxide deposit.Surf Coat Tech 202, 5020-5026, 2008.

[10] J. R. Rathish, R. Dorothy, R. M. Joany, M. Pandiarajan, S. Rajendran:Corrosion resistance of nanoparticle incorporated nanocoatings. Euro Chem Bull 2, 965-970, 2013.

[11] M. Y. Jiang, L. K. Wu, J. M. Hu, J. Q. Zhang:Silane-incorporated epoxy coatings on aluminum alloy (AA2024). Part 1: Improved corrosion performance. Corr Sci 92, 118-126, 2015.

[12] M. Y. Jiang, L. K. Wu, J. M. Hu, J. Q. Zhang:Silane-incorporated epoxy coatings on aluminum alloy (AA2024), Part 2: Mechanistic investigations. Corr Sci 92, 127-135, 2015.

[13] R. Mishra, R. Balasubramaniam:Effect of nanocrystalline grain size on the electrochemical and corrosion behaviour of nickel. Corr Sci 46, 3019–3029, 2004.

[14] D. G. Papageorgiou, I. A. Kinloch, R. J.Young:Mechanical properties of graphene and graphene-based nanocomposites. Prog MatSci 90, 75-127, 2017.

[15] S.C.Ray:Application and uses of graphene. In: Applications of Graphene and Graphene-Oxide Based Nanomaterials, Elsevier Inc., 1-38, 2015.

[16] N. H. Othman, M. C. Ismail, M. Mustapha, N. Sallih, K. E. Kee, R. A. Jaal:Graphene based polymer nanocomposites as barrier coatings for corrosion protection. ProgOrg Coat 135, 82-99, 2019.

[17] A. Islam, B. Mukherjee, K. K. Pandey, A. K. Keshri: Ultrafast, Chemical-free, mass production of high quality exfoliated graphene. ACS Nano 15, 1775-1784, 2021.

[18] S. Lee, S. H. Eom, J. S. Chung, S. H. Hur: Large-scale production of high-quality reduced graphene oxide. Jour ChemEng 233, 297-304, 2013.

[19] Y. Xie, C. Liu, W. Liu, L. Liang, S. Wang, F. Zhang, H. Shi. M. Yang: A novel approach to fabricate polyacrylate modified graphene oxide for improving the corrosion resistance of epoxy coatings, Colloids Surf. A PhysicochemEng Asp, 593, 124627, 2020.

[20] X. Zhu, Z. Ni, L. Dong, Z. Yang, L. Cheng, X. Zhou, Y. Xing, J. Wen, M. Chen:In-Situ modulaton of interactions between polyaniline and graphene oxide films to develop waterborne epoxy anticorrosion coatings. Prog Org Coat 133, 106–116, 2019.

[21] Q. Zhu, E. Li, X. Liu, W. Song, Y. Li, X. Wang, C. Liu: Epoxy coating with in-situ synthesis of polypyrrole functionalized graphene oxide for enhanced anticorrosive performance. Prog Org Coat 140, 105488, 2020.

[22] I. Khosravi, Z. Shahryari, S. M. J. Moghadas, H. T. Sarraf, M. Yegane:The application of graphene oxide as corrosion barrier. Micro and Nano Technologies 127-140, 2020.

[23] N. H. Bakar, G. A. M. Ali, J. Ismail, H. Algarni, K. F. Chong: Size-dependent corrosion behavior of graphene oxide coating.Prog Org Coat 134, 272-280, 2019.

[24.] Y. Su, V. G. Kravets, S. L. Wong, J. Waters, A. K. Geim, R. R. Nair: Impermeable barrier films and protective coatings based on reduced graphene oxide. Nat Comm 5, 4843, 2014.

[25] J. Li, J. C. Cui, J. Y. Yang, Y. Y. Li, H. X. Qiu, J. H. Yang:Reinforcement of graphene and its derivative on anticorrosive properties of waterborne polyurethane coatings.Compos SciTechnol 206, 30-37, 2019.

[26] C. L. Chen, Y. He, G. Q. Xiao, Y. Q. Xia, H. J. Li, Z. He:Two-dimensional hybrid materials: MoS_2-rGO nanocomposites enhanced the barrier properties of epoxy coating. Appl Surf Sci 444, 511-521, 2018.

[27] X. K. Cao, F. Huang, C. Huang, J. Liu, Y. F. Cheng:Preparation of grapheme nanoplate added zinc-rich epoxy coatings for enhanced sacrififcial anode-based corrosion protection. CorrSci 159, 108-120, 2019.

[28] N. T. Kirkland, T. Schiller, N. Medhekar, N. Birbilis:Exploring graphene as a corrosion protection barrier. CorrSci 56, 1-4, 2012.

[29] Y. H. Yu, Y. Y. Lin, C. H. Lin, C. C. Chan, Y. C. Huang:High performance polystyrene/graphene-based nanocomposites with excellent anti-corrosion properties. Polymer Chem 5, 535-550, 2013.

[30] M. J. Nine, M. A. Cole, D. N. H. Tran, D. Losic, Graphene: a multipurpose material for protective coatings, J. Mater. Chem. A, J. Mater. Chem. A, 3, 12580-12602, 2015.

[31] P. A. Dearnley, G. A. Smith:Corrosion–wear mechanisms of hard coated austenitic 316L stainless steels.Wear 256, 491– 499, 2004.

[32] W. Zhang, S. Lee, K. McNear:Use of graphene as protection film in biological environments. Sci Rep 4, 4097, 2014.

[33] H. Kinoshita, Y. Nishina, A. A. Alias, M. Fujii:Tribological properties of monolayer graphene oxide sheets as water-based lubricant additives. Carbon 66, 720, 2014.

[34] J. S. Bunch, S. S. Verbridge, J. S. Alden, A. M. Van der Zande, J. M. Parpia, H. G. Craighead:Impermeable atomic membranes from graphene sheets. Nano Lett 8, 2458-2462, 2008.

[35] H. Zheng, Y. Shao, Y. Wang, G. Meng, B. Liu: Reinforcing the corrosion protection property of epoxy coating by using graphene oxide–poly(urea–formaldehyde) composites. CorrSci 123, 267-277, 2017.

[36] B. Ramezanzadeh, E. Ghasemi, M. Mahdavian, E. Changizi, M. H. M. Moghadam:Covalently-grafted graphene oxide nanosheets to improve barrier and corrosion protection properties of polyurethane coatings. Carbon 93, 555–573, 2015.

[37] R.R. Abakah, F. Huang, Q. Hu, Y.Wang, L. Jing: Comparative Study of Corrosion Properties of Different Graphene Nanoplate/Epoxy Composite Coatings for Enhanced Surface Barrier Protection. Coatings 11, 285, 2021.

[38] F. Bellucci, L. Nicodemo:Water transport in organic coatings.Corrosion 49, 235– 247, 1993.

[39] K. S. Aneja, H. L. Mallika, H. L. M. Böhm, A. S. Khanna, S. Böhm:Functionalised graphene as a barrier against corrosion. Flat Chem 1, 11–19, 2016.

[40] S. Zhou, Y. Wu, W. Zhao, J. Yu, F. Jiang, L. Ma: Comparative corrosion resistance of graphene sheets with different structures in waterborne epoxy coatings. Colloids and Surfaces A: Physicochemical and Engineering Aspects 556, 273-283, 2018.

[41] K. S. Aneja, S. Bohm, A. S. Khanna,H. L. M. Bohm:Comparative corrosion resistance of graphene sheets with different structures in waterborne epoxy coatings. Nanoscale 7, 17879-17888, 2015.

[42] A. Liang, X. Jiang, X. Hong, Y. Jiang, Z. Shao, D. Zhu: Recent Developments concerning the dispersion Methods and Mechanism of Graphene. Coatings 8, 33, 2018.

[43] K. C. Chang, W. F. Ji, C. W. Li, C. H. Chang, Y. Y. Peng, J. M. Yeh, W. R. Liu:The effect of varying carboxylic group content in reduced graphene oxides on anti-corrosive properties of PMMA/graphene composites. Express PolymLett 8, 908-919, 2014.

[44] H. Yang, C. Shan, F. Li, Q. Zhang, D. Han, L. Niu:Convenient preparation of tunably loaded chemically converted grapheneoxide/epoxy resin nano-composites from graphene oxide sheets through two-phase extraction. Jour Mater Chem 19, 8856-8860, 2009.

[45] S. Pourhashem, M. R. Vaezi, A. Rashid, M. R. Bagherzadeh: Exploring corrosion protection properties of solvent based epoxy-graphene oxide nanocomposite coatings on mild steel. CorrSci 115, 78-92, 2016.

[46] Xia W, Xue H, Wang J, Wang T, Song L, Guo H, Fan X, Gong H, He J,Functional graphene serving as free radical scavenger and corrosion protection in gamma-irradiated epoxy composites,Carbon, 101, 315-323, 2016.

[47] H. Yuan, F. Qi, N. Zhao, P. Wan, B. Zhang, H. Xiong, B. Liao:Graphene oxide decorated with titanium nanoparticles to reinforce the anti-corrosion performance of epoxy coating. Coatings10, 29, 2020.

[48] Y. Li, Z. Yang, H. Qiu, Y. Dai, Q. Zheng, J . Yang: Self-aligned graphene as anticorrosive barrier in waterborne polyurethane composite coatings. Jour Mater Chem 2, 14139-14145, 2014.

[49] J. Liu, W. Yang, L. Tao, D. Li, C. Boyer, T. P. Davis:Thermosensitive graphene nanocomposites formed using pyrene-terminal polymers made by RAFT polymerization. JournPolymSci Part PolymChem 48, 425–433, 2010.

[50] W. Sun, L. Wang, T. Wu, Y. Pan, G. Liu:Synthesis of low-electrical-conductivity graphene/pernigranilinecomposites and their application in corrosion protection. Carbon 79, 604-614, 2014.

[51] Z. Zhang, W. Zhang, D. Li, Y. Sun, Z. Wang, C. Hou, L. Chen, Y. Cao, Y. Liu:Mechanical and anticorrosive properties of graphene/epoxy resin composites coating prepared by in-situ method. IntJournMolSci 16, 2239–2251, 2015.

[52] H. Lu, S. Zhang, W. Li, Y. Cui, T. Yang: Synthesis of graphene oxide-based sulfonatedoligoanilines coatings for synergistically enhanced corrosion protection in 3.5% NaCl solution. Appl Mater Inter 9, 4034-4043, 2017.

[53] Y. Yu, Y. Lin, C. Lin, C. Chan, Y. Huang:High-performance polystyrene/graphene based Nanocomposites with excellent anti-corrosion properties. PolymChem 5, 1049-1056, 2014 .

[54] C. H. Chang, T. C. Huang, C. W. Peng, T. C. Yeh, H. I. Lu, W. I. Hung, C. J. Weng, T. I. Yang, J. M. Yeh:Novel anticorrosion coatings prepared from polyaniline/ graphene composites. Carbon 50, 5044–5051, 2012 .

[55] Z. Yu, H. Di, Y. Ma, L. Lv, Y. Pan, C. Zhang, Y. He:Fabrication of graphene oxide-alumina hybrids to reinforce the anti-corrosion performance of composite epoxy coatings. Appl Surf Sci 351, 986-996, 2015.

[56] Z. Yu, H. Di, Y. Ma, Y. He, L. Liang, L. Lv, X. Ran, Y. Pan, Z. Luo: Preparation of graphene oxide modified by titanium dioxide to enhance the anti-corrosion performance of epoxy coatings. Surf Coat Technol 276, 471-478, 2015.

[57] Y. Ma, H. Di, Z. Yu, L. Liang, P. Yang, Y. Zhang, D. Yin:Fabrication of silica-decorated graphene oxide nanohybrids and the properties of composite epoxy coatings. Appl Surf Sci 360, 936-945, 2016.

[58] D. Li, M. B. Müller, S. Gilje, R. B. Kaner, G. G. Wallace:Processable aqueous dispersions of graphene nanosheets. Nat Nanotech 3, 101–105, 2008.

[59] L. B. Liu, K. Tan, J. Zhang:Preparation of polyacrylate sodium ceramic slurry dispersant and study on its dispersion mechanism. Bulletin of the Chinese Ceramic Society 24, 91-94, 2005.

[60] C. Cheng, Q. Shihui, C. Mingjun, Q. Songlv, Y. Guoping, Z. Haichao, W. Liping, X. Qunji:Achieving high performance corrosion and wear resistant epoxy coatings via incorporation of noncovalent functionalized graphene. Carbon114, 356-366, 2017.

[61] T. Yang, Y. Cui, Z. Li, H. Zeng, S. Luo, W. Li:Enhancement of the corrosion resistance of epoxy coating by highly stable 3, 4, 9, 10-perylene tetracarboxylic acid functionalized graphene, Journ. Hazard Mater 357, 475-482, 2018.

[62] M. Z. Iqbal, A. A. Abdala, V. Mittal, S. Seifert, A. M. Herring, M. W. Liberatore:Processable conductive graphene/ polyethylene nanocomposites: Effects of graphene dispersion and polyethylene blending with oxidized polyethylene on rheology and microstructure.Poly98, 143–155, 2016.

[63] S. Liu, M. Tian, B. Yan, Y. Yao, L. Zhang, T. Nishi, N. Ning:High performance dielectric elastomers by partially reduced graphene oxide and disruption of hydrogen bonding of polyurethanes. Polymer 56, 375–384, 2015.

[64] X. Li, D. L. Zhao, L. Z. Bai, F. Li, H. J. Zhao, L. F. Gao:Graphene oxide as a nanocarrier for controlled loading and release of doxorubicin hydrochloride. JournFunct Mater 44, 96-98, 2013.

[65] M .Ayan-Varela, J. I. Paredes, L. Guardia, S. Villar-Rodil, J. M. Munuera, M. Díaz-Gonzalez, C. Fernandez-Sanche, A. Martínez-Alonso, J. M. Tasc:Achieving extremely concentrated aqueous dispersions of graphene flakes and catalytically efficient graphene-metal nanoparticle hybrids with flavin mononucleotide as a high-performance stabilize. Appl Mater Inter 7, 10293-10307, 2015.

[66] O. Yaglioglu, T. Fang, R. Martens, B. Eldridge:Electroless silver plating and in-situ SEM characterization of CNT-metal hybrid contactors, IEEE 60th Holm Conference on Electrical Contacts (Holm), New Orleans, LA, USA, 1-5, 2014.

[67] X. Zhang, Y. Zhou, A. Liang, B. Zhang, J. Zhang:Facile fabrication and corrosion behavior of iron and iron-reduced graphene oxide composite coatings by electroless plating from baths containing no reducing agent. Surf CoatTechnol 304, 519–524, 2016.

[68] C. M. P. Kumar, T. V. Venkatesha, R. Shabadi:Preparation and corrosion behavior of Ni and Ni–graphene composite coatings. Mat Res Bull 48, 1477–1483, 2013.

[69] M. H. Nazir, Z. A. Khan, A. Saeed, V. Bakolas, W. Braun, R. Bajwa, S. Rafique:Analyzing and Modelling the Corrosion Behavior of Ni/Al2O3, Ni/SiC, Ni/ZrO2 and Ni/Graphene Nanocomposite Coatings, Materials, 10, 1225, 2017.

[70] M.Y. Rekha, P.M.K. Kumar, C. Srivastava:Electrochemical Behaviour of Chromium-Graphene Composite Coating. RSC Adv 6, 62083-62090, 2016.

[71] Y. Raghupathy, A. Kamboj, M. Y. Rekha, N. P. Narasimha, C. Srivastava:Copper-graphene oxide composite coatings for corrosion protection of mild steel in 3.5% NaCl. Thin Solid Films 636, 107-115, 2017.

[72] K. C. Chang, M. H. Hsu, H. I. Lu, M. C, Lai, P. J. Liu, C. H. Hsu, W. F. Ji, Chuang TL, Wei Y, Yeh JM, Liu WR Room-temperature cured hydrophobic epoxy/graphene composites as corrosion inhibitor for cold-rolled steel, Carbon, 66, 144-153, 2014.

[73] H. Hayatdavoudi, M. A. Rahsepar:Mechanistic study of the enhanced cathodic protection performance of graphene-reinforced zinc rich nanocomposite coating for corrosion protection of carbon steel substrate. Jour Alloys Comp 727, 1148-1156, 2017.

[74] L. Jing, J. Cui, J. Yang, Y. Li, H. Qiu, Yang:Reinforcement of graphene and its derivatives on the anticorrosive properties of waterborne polyurethane coating. Jour Comp SciTechn 129, 30-37, 2016.

[75] K. Krishnamoorthy, K. Jeyasubramanian, M. Premanathan, G. Subbiah, H. S. Shin, S. J. Kim:Graphene oxide nanopaint. Carbon 72, 328–337, 2014.

[76] S. Chen, L. Brown, M. Levendorf, W. Cai, S. Y. Ju, J. Edgeworth:Oxidation resistance of graphene-coated Cu and Cu/Ni alloy. ACS Nano 5, 1321-1327, 2011.

[77] A. Tiwari, R. K. Singh:Long-Term Corrosion Protection of a Cupro-Nickel Alloy Due to Graphene Coating. Coatings 7, 210, 2017.

[78] D. Prasai, J. C. Tuberquia, R. R. Harl, G. K. Jennings, K. I. Bolotin:Graphene : Corrosion inhibition coating ACS Nano 6, 1102-1108, 2012.

[79] M. J. Nine, M. A. Cole, D. N. Tran, D. Losic:Graphene: Amultipurposematerial for protective coatings. Jour Mater ChemA 3, 12580–12602, 2015.

[80] M. A. Krishnan, K. S. Aneja, A. Shaikh, S. Bohm, K. Sarka, H. L. M. Bohm, V. S. Raja:Graphene based anticorrosive for copper. RSC Adv. 8, 499-507, 2018.

[81] N.U. Kiran, S. Dey, B.P. Singh, L. Besra: Graphene coating on copper by electrophoretic deposition for corrosion prevention. Coatings 7, 214, 2017.

[82] R. Singh, R. K. Chakraborty, P. Banerjee, D. E. Lobo, H. Gullapalli, M. Sumandasa, A. Kumar, L. Choudhary, R. Tkacz, P. M. Ajayan, M. Majumder:Protecting copper from electrochemical degradation by graphene coating. Carbon 50, 4040-4045, 2012.

[83] G. Kalita, M. E. Ayhan, S. Sharma, S. M. Shinde, D. Ghimire, K. Wakita, M. Umeno, M. Tanemura:Low temperature deposited graphene by surface wave plasma CVD as effective oxidative resistive barrier. CorrosSci 78, 183-187, 2014.

[84] K. Qi, Y. Sun, H. Duan, X. Guo:A corrosion-protective coating based on a solution-processable polymer-grafted graphene oxide nanocomposite. CorrSci 98, 500-506, 2015.

[85] J. H. Park, J. M. Park:Electrophoretic deposition of graphene oxide on mild carbon steel for anti-corrosion application. SurfCoatTechn 254, 167-174, 2014.

[86] J. Lui, L. Hua, S. Li, M. Yu: Graphene dip coatings: An effective anti-corrosion barrier on aluminium. App Surf Sci 327, 241-245, 2015.

[87] G. S. Hikku, K. Jeyasubramanian, A. Venugopal, R. Ghosh: Corrosion resistance behavior of graphene/polyvinyl alcohol nanocomposite coating for aluminium-2219 alloy. Jour All Comp 716, 259-269, 2017.

[88] D. Kang, J. Y. Kwon , H. Cho, J. H. Sim, H. S. Hwang, C. S. Kim, Y. J. Kim, R. S. Ruoff, H. S. Shin:Oxidation Resistance of Iron and Copper Foils Coated with Reduced Graphene Oxide Multilayers. ACS Nano 6, 7763–7769, 2012.

[89] G. Cui, Z. Bi, R. Zhang, J. Lui, X. Yu, Z. Li: A comprehensive review on graphene-based anti-corrosive coatings. ChemEng Jour 373, 104-121, 2019.

[90] S. Böhm: Graphene against corrosion.Nature Nanotech 9, 741–742, 2014.

[91] B. P Singh., B. K. Jena, S. Bhattacharjee, L. Besra:Development of oxidation and corrosion resistance hydrophobic graphene oxide-polymer composite coating on copper. Surface and Coatings Technology 232, 475–481, 2013.

[92] B. P. Singh, S. Nayak, K. K. Nanda, B. K. Jena, S. Bhattacharjee, Besra L: The production of a corrosion resistant graphene reinforced composite coating on copper by electrophoretic deposition. Carbon 61, 47–56, 2013.

[93] K. C. Chang, C. H. Hsu, H. I. Lu, W. F. Ji, C. H. Chang, W. Y. Li, T. L. Chuang, J. M. Yeh, W. R. Liu, M. H. Tsai: Advanced anticorrosive coatings prepared from electroactive polyimide/graphene nanocomposites with synergistic effects of redox catalytic capability and gas barrier properties. EXPRESS Polymer Letters 8, 243–255, 2014.

[94] M. Rajabi, G. R. Rashed, D. Zaarei: Assessment of graphene oxide/epoxy nanocomposite as corrosion resistance coating on carbon steel. CorrEngSciTechn 50, 509-516, 2014.

[95] M. J. Nine, M. A. Cole, L. Johnson, D. N. Tran, D. Losic: Robust superhydrophobic graphene-based composite coatings with self-cleaning and corrosion barrier properties. ACS Appl Mater Interfaces 7, 28482–28493, 2015.

[96] Y. Cao, X. Tian, Y. Wang, Y. Sun, H. Yu, D. S. Li, Y. Liu:In situ synthesis of reduced graphene oxide-reinforced silicone-acrylate resin composite films applied in erosion resistance. Jour. Nanomater 2, 1-8, 2015.

[97] C.Y. Huang, P.Y. Tsai, B.E. Gu, W.C. Hu, J.S. Jhao, G.S. Jhaung, Y. L. Lee: The Development of Novel Sound-Absorbing and Anti-Corrosion Composite Coating. ECS Transactions 72, 171-183, 2016.

[98] Y. Jafari, S. M. Ghoreishi, M. S. Nooshabadi: Polyaniline/Graphene nanocomposite coatings on copper: Electropolymerization, characterization, and evaluation of corrosion protection performance. Synthetic Metals 217, 220-230, 2016.

[99] S. Liu, L. Gu, H. Zhao, J. Chen, H. Yu: Corrosion resistance of graphene reinforced waterborne epoxy coatings. Jour Mater SciTech 32, 425–431, 2016.

[100] H. Di, Z. Yu, M. Yu, C. Zhang, F. Li, L. Liang, P. Yang, S. Heng, H. Yi: Corrosion-resistant hybrid coatings based on graphene oxide–zirconia dioxide/epoxy system. Jour. of the Taiwan Institute of Chemical Engineers 67, 511-520, 2016.

[101] M. Li, X. Ji, L. Cui, J. Liu:In situ preparation of graphene/polypyrrolenanocomposite via electrochemical co-deposition methodology for anti-corrosion application. Jour Mater Sci 52, 12251–12265, 2017.

[102] K. Catt, H. Li, C. X. Tracy:Poly(3,4-ethylenedioxythiophene) Graphene Oxide Composite Coatings for Controlling Magnesium Implant Corrosion. ActaBiomaterialia 48, 530-540, 2016.

[104] D. Yu, S. Wen, J. Yang, J. Wang, Y. Chen, J. Luo, Y. Wu: RGO modified ZnAl-LDH as epoxy nanostructure filler: a novel synthetic approach to anticorrosive waterborne coating. Surf Coat Tech 326, 207–215, 2017.

[105] Y. Wang, Y. Zhou, Y. Ma, H. Lu, Y. Sun, G. Zhao, Y. Liu.:Preparation of a natural rubber nanocomposite coating based on Fe_3O_4 carbon materials and their corrosion resistance. Int Jour ElectrochemSci 12, 9798–9811, 2017.

[106] S. Pourhashem, A. Rashidi, M. R. Vaezi, M. R. Bagherzadeh: Excellent corrosion protection performance of epoxy composite coatings filled with amino-silane functionalized graphene oxide. Surf Coat Technol 317, 1–9, 2017.

[107] S. Pourhashem, M. R. Vaezi, A. Rashidi:. Investigating the effect of SiO2- graphene oxide hybrid as inorganic nanofiller on corrosion protection properties of epoxy coatings. Surf Coat Technol 311, 282–294, 2017.

[108] M. Selvam, K. Saminathan, P. Siva, P. Saha, V.Rajendran: Corrosion behavior of Mg/graphene composite in aqueous electrolyte. Mat ChemPhy 172, 129-136, 2016.

Journal of Metallurgy and Materials Science, Vol. 63, No. 3-4, July-December 2021
Printed in India, © NML, ISSN 0972-4257

Total Dissolved Solids (TDS) in Packaged Drinking water in India: A Review

Pragati Jha*and Mita Tarafder
CSIR-National Metallurgical Laboratory
Jamshedpur-831007, Jharkhand, India.

1. ABSTRACT :

Many parameters are used to determine the quality of water. One vital parameter is Total dissolved solids (TDS) which measure the deterioration of water quality. Regular consumption of low TDS in packaged drinking water leads to adverse health effects like chronic gastritis, cardiovascular diseases, homeostasis, and metabolic acidosis in humans. In this review, an overview of low TDS and its ill effects on human health due to the consumption of packaged drinking water containing low minerals is discussed.

Keywords : *Total dissolved solids (TDS), Packaged drinking water (PDW), Impacts of low TDS, Human health and TDS, Low minerals.*

2. INTRODUCTION

Total Dissolved Solids (TDS) is one of the water quality parameters which can be defined as the presence of inorganic salts like Ca, Mg, Na, CO_3^-, Cl^-, SO_4^-, NO_3^- and other cations and anions as their major constituents in the water [1]. It is determined by weighing the residue left after the evaporation of the filtered water sample at 180^0 C [2].

$$\text{TDS }\left(\frac{mg}{l}\right) = \frac{Mass\ of\ solids\ (W_2 - W_1)\ (g)}{Volume\ of\ sample\ (ml)} \times 1000$$

Where, the value of W_2 is the final weight of the dish and filtrate after evaporation, and W_1 is the initial weight of the dish before evaporation. TDS is one of the oldest parameters for determining the quality of water and has always been taken to represent materials present in the water [3]. Low level of TDS in packaged drinking water like bottled water, sachet water, and distilled water is believed to cure arthritis by "washing out" calcium from deposits in joints. Many believed that consuming water containing low TDS, those which are treated by distillation, reverse osmosis, or deionization tends to leach out minerals from the body and causes its deficiencies and other ill-effects [4]. Recent years have witnessed high emergence and rapid growth of the bottled water industry; perhaps due to its ease of availability in carrying, inexpensive cost, and absence of harmful contaminants have made packaged water a good alternate source for drinking in maximum developing and developed countries [5]. Bottled water represents water sealed in plastic containers without any added ingredients, containing safe and harmless antimicrobial agents which are suitable for drinking [6]. In India, the bottled water industry showed remarkable growth when Parley launched Bisleri. India is now counted in the top ten countries in terms of bottled water utilization. According to the survey data analysis in several restaurants and hotels in Kolkata West Bengal, India, it was observed that the packaged drinking water like Kinley had a maximum market share off around 52%, followed by Bisleri and Aquafina 14% each, bailey shared 4% of the market share, and other companies shared the rest 16%[7]. Due to the over-treatment of packaged drinking water, they lack in essential minerals hence resulting in low TDS of water. The classification of water, based on mineral content and concentration of TDS along with its palatability with respect to the European Union mineral water directive (EU) [8] and Bureau of Indian Standards (BIS) [9], is mentioned in Table-1

Corresponding Author :
Email: pragati1371@gmail.com

Table-1 ***Classification of different water type based on concentration of TDS***

EU		BIS	
Water Type	***Criteria TDS (mg/l)***	***Concentration of TDS (mg/l)***	***Palatability remark***
Very low mineral concentration	Mineral content (TDS) <50 mg/l	< 300 mg/l	Excellent
Low mineral concentration	TDS 50-500 mg/l	300-600 mg/l	Good
Average mineral concentration	TDS 500-1500 mg/l	600-900 mg/l	Fair
High mineral concentration	TDS > 1500 mg/l	900- 1200 mg/l	Poor
-	-	>1200 mg/l	Unacceptable

Even though the consumption of bottled drinking water has increased worldwide, strict standardization and periodic inspection are essential factors for both economy and human health. The World Health Organization (WHO) provides general guidelines that are essential for better water quality [10, 11]. Similarly, in India Bureau of Indian Standards (BIS) formulates Indian standards drinking water specifications required in drinking water [9]. Studies elsewhere have shown non-compliance of physicochemical properties of packaged drinking water with the results mentioned in their labeling. Bottled water is also regulated by various international guidelines provided by International Bottled Water Association (IBWA), Food and Drug Administration (FDA), and United State Environmental Protection Agency (USEPA) as mentioned in table-3 [9-12].

2.1. Correlation of TDS with pH and EC of water

TDS, pH, and Electrical Conductivity (EC) are the essential parameters that determine the quality of water. pH is the measure of acidity and alkalinity of the solution. The scale of pH ranges from 0-14. The scale is logarithmic, not linear. For example, if the solution has pH 6 then it is ten times more acidic than pH 7. Pure water is said to have a pH of 7. Water below pH value 7 is considered acidic while pH above 7 is considered as basic or alkaline. Electrical conductivity can be defined as the capacity of the solution to carry an electric current. The ability to pass electrical flow mainly depends on the concentration of ions present in it along with the optimum temperature. Solutions with more inorganic salts, acid, and bases have good EC [13]. TDS and EC are indicators of salinity in the water and are correlated [14, 15]. Researchers have done various investigations to find out the precise mathematical correlation between EC and TDS. TDS concentration can be easily calculated from the EC value as per the given equation [14].

$$\text{TDS}\ \left(\frac{mg}{l}\right) = \text{k} \times \text{EC}\ \left(\frac{\mu s}{cm}\right)$$

Where k measures the ionic concentrations and the value of k depends on the ion concentration and it increases with the increasing ions in water. If EC increases the amount of TDS also increases. Thus TDS when correlated with conductivity directly, affects the pH of the drinking water. If the EC is high, TDS becomes more and the pH of the water decreases resulting in acidity [1].

2.2. Desirable TDS Content of Drinking Water

If the TDS level changes then the texture and taste of water also change. Maintaining the TDS level of bottled water is essential for maintaining good health. According to Bisleri, TDS level 50-150 mg/l is excellent and is considered as the most suitable and acceptable limit for drinking [16]. According to World Health Organization, 1980 report, a minimum of 100 mg/l of TDS is required to be present in water. The recent guidelines of WHO, 2017 recommended TDS level <1000 mg/l as suitable for drinking.

Thus, the research on TDS and packaged drinking water continues with various modifications in research methods. This paper presents the overview of drinking low TDS water such as packaged drinking water and its impact on consumer's health due to low mineral consumption and the various methods adopted in determining TDS of water.

3. REVIEW OF LITERATURE

Various methods for testing TDS in packaged water at research levels are adopted and presented in the technical papers, which have been referred to, for the present review. The critical findings from these papers are discussed below.

Mahajan et al. [17] took seventeen bottled samples of various brands, collected from various retailed shops in Amritsar, India. The physical and chemical parameters, like TDS, Ca, Mg, pH, Cl, K, hardness, Zn, Cd, Cu, and Chlorine demand of the sample were analyzed in the laboratory to match it with the recommended limits of WHO and USEPA. The pH of the samples was determined using a pH meter, TDS was determined using the evaporation method and Conductivity using a conductometer. The authors analyzed the pH of the samples, out of 17 samples 3 samples were found slightly acidic with pH values around 6.79, 6.83, and 6.73 respectively. Thus, all the commercially packaged drinking water had pH value within the prescribed limits by WHO and USEPA. It was observed through the experiment that all the samples had TDS values lower than the recommended limit of 500 ppm, three of the packaged water had TDS < 50, and another four <100 ppm. The authors discussed the results and pointed out that the water lacks essential minerals and is lower than the desirable limits and the majority of the brands of packaged water are over-treated. This paper gives an overview about over treatment of packaged drinking water resulting in low mineral content, when consumed it can lead to mineral deficiency in the body. Studies all across the world revealed that various methods are adopted for determining the TDS present in water as shown in Table-2.

Table-2. Various methods to determine TDS of water

Parameter	Various Methods	Sources
TDS (mg/l)	Evaporation method	[17], [18]
	Gravimetric method	[19], [20]
	Digital TDS meter	[1], [21], [22], [23], [24], [25]
	*AAS	[26]
	YSI-Multiparameter	[27], [28]
	Conductivity meter	[11], [29],[30]
	TDS and EC relationship	[31]

*AAS- Atomic Absorption Spectrophotometer.

Ray et al. [32] conducted a study to access the physicochemical quality of Packaged Drinking Water (PDW) in the city of Kolkata, West Bengal, India. The authors took 27 types of PDW and 10 different types of bubble top can PDW. The analysis of the sample was done at the School of Water Resource Engineering, Jadavpur University, West Bengal, as per the prescribed guidelines of the American Public Health Association (APHA). Another, eighteen samples were collected randomly from Kolkata Municipal Corporation (KMC) in different localities. The samples were analyzed and the result of PDW and KMC were compared with each other. The samples were tested for both bacteriological and physicochemical parameters. The pH and turbidity of the samples were determined using digital pH meter and Nephelo-turbidity meter, and TDS was measured with a digital TDS meter, whereas Fluoride, Chloride TH was determined using Ion-selective Electrode (ISE), argentometric method, and EDTA titration method, respectively. The study also showed that 41% of PDW had a pH value of 6.5 and was acidic. The minerals content, TDS, Ca, Mg, the types of PDW were found low and F^- were found negligible. All PDW showed the minimum TDS level between 38.26 mg/l for bottled water, 24.68 mg/l for bubble top cans, and the maximum of 117 mg/l, which signifies a low level of TDS in water. On the other hand, the samples of KMC water supply showed higher values of the above-mentioned physicochemical parameters. The study concludes that the regular consumption of low-mineralized water is not safe and may lead to potential health risks like an irritation to mucous membranes and cardiovascular diseases. The KMC water supply can be a good alternative for drinking purposes. This paper compared two different types of water that are packaged and tap water, where the data reveals that the packaged drinking water showed low mineral content as compared to water of Kolkata municipal corporation. The authors concluded that tap water is safer as compared to PDW due to its high mineral content.

Rao et al. [19] conducted a study to assess the physical, chemical, and bacteriological parameters of various packaged and public drinking water. The samples were collected from villages of Vikarabad, located in Telangana, India. One sample from each bore well from 35 villages in Vikarabad Mandal, one municipality tap water sample from Vikarabad municipality, and five samples of each brand of bottled, four sachets, and four canned water sample was collected from the same location. For analyzing the physical and chemical evaluation the bore well water samples, canned and municipality water samples were collected in sterilized white jerry cans of 1L capacity. For analyzing the bacteriological parameter same samples were collected in sterilized jars of 100 ml capacity along with bottled water and sachets of 1L capacity. All water samples were collected under sterilized conditions, numbered in the sequence and refrigerated to preserve the parameters, and transported to Telangana State Pollution Control Board, Hyderabad for analysis. The guidelines of the American Public Health Association (APHA) were followed for the analysis of the samples. The pH of the sample was examined using a pH meter, the EC of the sample was examined using a conductivity meter and the TDS of the samples were determined using the gravimetric method. The values obtained from the studied parameters were compared with the guidelines provided by the Bureau of Indian Standards (BIS) given in table-3.

Table-3. ***Guidelines for the maximum allowable levels of contaminants in drinking water***

Parameters	***IBWA***	***FDA***	***USEPA***	***WHO***	***BIS***
pH	6.5-8.5	-	6.5-8.5	6.5-8.5	6.5-8.5
TDS (mg/l)	500	500	500	<1000	500
EC (µS/cm)	-	-	-	400	-

***IBWA-** International Bottled Water Association; **FDA-** Food and Drug Administration; **USEPA-** U.S Environmental Protection Agency; **WHO-** World Health Organization; **BIS-**Bureau of Indian Standard.

The statistical analysis and Pearson's correlation of the result were obtained using the SPSS package (Version 21.0) given in Table-4.

Parameter	**Min/Max/Mean**	**Bottle**	**Sachet**	**Can**	**Bore well**	**Tap water**
pH	Minimum	5.52	5.98	7	5.9	
	Maximum	6.89	7.58	7.5	9.4	
	Mean	6.34	7.13	7.2	6.8	7.8
Electrical Conductivity	Minimum	47	53	48	49	
	Maximum	181	174	690	1299	
	Mean	104.4	111.5	214.5	658.7	456
TDS	Minimum	31	34	31	32	
	Maximum	118	113	445	1012	
	Mean	67.8	73	139.5	498.2	296

Table-4:***Mean values of physicochemical parameters assessed in drinking water.***

The physicochemical quality of drinking water from different sources like bottled, sachet can, bore well and tap water was not within the permissible limits in Vikarabad, India.

Khatri et al. [33] conducted a study to assess the quality of drinking water in nine villages of Harij Taluka, located in Patan district in Northern Gujarat, India. Water from nine villages was sampled for the analysis of parameters that are crucial for drinking, such as TDS, F, Mg, Cl, dissolved oxygen, and many others at GEMI'S Laboratory, Gandhinagar, Gujarat. Weekly analysis of the samples for pH was done for six consecutive weeks.The result was observed and noted. The pH of the water was found in the range between 6.5-8.5which was within the range provided by BIS [9] in all the samples for the six consecutive weeks. The conductivity of water samples was analyzed for six consecutive weeks. It was found that the conductivity of water samples was below 400 µS/cm except for the two villages, where it was present beyond the acceptable limits. The samples were analyzed for TDS in water. It was found that the TDS of water was above 500 mg/L in Jaswantpura and Jasomav for all the weeks, which was beyond the acceptable limits of BIS [9]. Only the second week at Bhalana showed TDS level beyond the acceptable limits as per BIS as shown in Fig 1. The authors concluded that the quality of water in all the nine villages is of good quality and safe for human consumption.

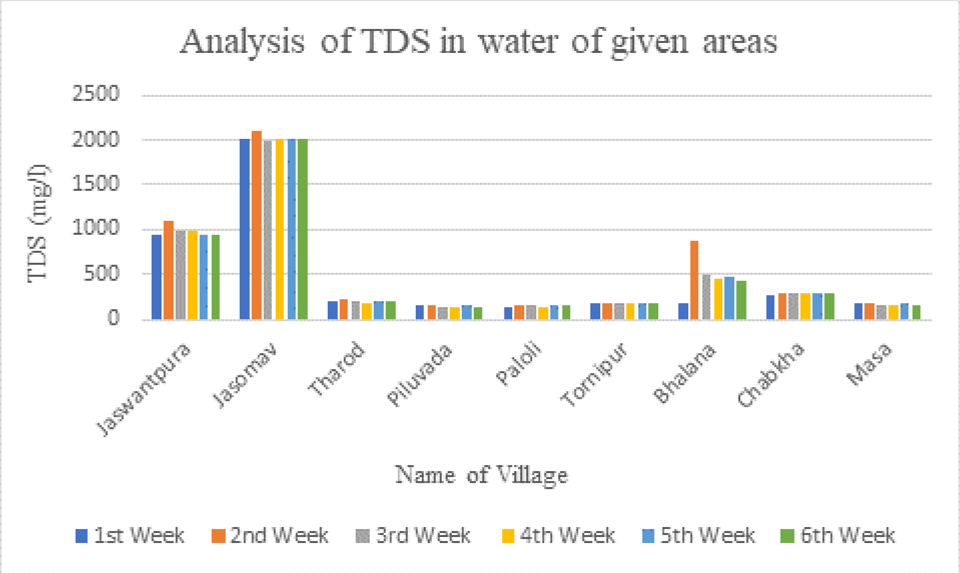

Fig 1. Graphical representation of scientific analysis of TDS in water samples [33].

4. IMPACT OF LOW TDS ON HUMAN HEALTH

Levallois et al. [34] state that the taste of water has an intense impact on a person's willingness to drink it. When consumers experience an unacceptable taste in drinking water, they typically look for different water sources. The sudden growth of bottled water is one of the reasons for this notion. In addition, the water treatment devices installed in buildings and homes of the consumers are the sign that they are searching for ways to improve drinking water taste [35]. The artificially produced desalinated/deionized water was previously used by laboratories and industries and not for drinking. However,in the last three decades, treated water has become a widely practiced technique in providing safe and clean drinking water. However, deionized water may vary in composition due to the existing treatment facilities which may result in minimum TDS and other minerals content. The high risk of health effects due to long-term consumption of desalinated water is of interest in countries and places where freshwater is not available and bottled water is consumed. Verma KC and Kushwaha AS [36] state that Ca and Mg are important elements for health. Although, drinking water is not the only source of our Ca and Mg but along with supplements they can outweigh its nutritional contribution to the body. Bubble top cans now a days are found in many homes and the demineralized water is utilized for cooking. Desalinated water when used for cooking causes substantial losses of all essential elements from foods like cereals and vegetables etc. The substantial losses may reach up to 60% for Ca and Mg or may also eliminate other microelements.

Demineralized or deionized water are those which is completely free from dissolved minerals resulting in low TDS (1 mg/l) of water. Such water also shows a low EC value. Research has been carried out to find the possible adverse health effect of water that lack dissolved mineral content. The ill effects of demineralized water on health are discussed below.

4.1. ***Effect of low mineral content of water directly on the mucous membrane of intestine, metabolism of body and homeostasis***

Some research in the laboratories has been conducted on animals and humans and the observation was noted accordingly. TDS less than 50 mg/l can impart a negative taste to the consumers. This type of water is also reported to be less thirst-quenching [37]. Although they have no high health risks, they should be taken into account when considering the suitability of low mineral content for consumption. Williams [38] reported that deionized water when introduced into the intestine of rats changed the epithelial cells. Schumann et al. [39] in their experiment for 14 days on rats concluded that there is no sign of erosion, ulceration, and inflammation in the stomach, oesophagus of rats. It has been adequately demonstrated [40] that water with low mineral content impart negative effect on the body's mechanism of homeostasis. The mechanism of homeostasis ensures equilibrium in the Urinary system. If the mineral content is low in the water, then the urine increases the elimination of major intra and extracellular ions from the body. Experiments on rats upto one year have shown that intake of distilled or deionized water that has a TDS value <75 mg/l leads to diuresis, increasing tendency of thirst, elimination of Na and Cl ions from the body. It also slows down the volume of red cells and leads to hematocrit changes [37]. The WHO 1980 report [40] came in agreement with the results of experiments evaluated by the researchers and agreed that low TDS water (TDS < 100 mg/l) results in diuresis, homeostasis, and increases the leaching of potassium, chloride, calcium, and magnesium ions from the body. The low mineral content in water acts on osmoreceptors of the gastrointestinal tract resulting in decreased aldosterone secretion and increasing sodium elimination. The German Society for Nutrition gave resembling conclusion about the effect of deionized or distilled water and warned the public against drinking it. Studies have shown that consuming low mineral water regularly may lead to acute damage such as hyponatremic shock or delirium. Hyponatremic shock, so-called "Water intoxication" increases with decreasing levels of TDS in water. More severe risk like acidosis and oedema was observed in infants whose drink was prepared using distilled, deionized or low-mineral bottled water [41].

4.2. ***Low or no intake of Ca and Mg from demineralized water***

Calcium (Ca) and Magnesium (Mg) are essential elements for the body. Ca is a substantial component of bones and teeth while Mg acts as cofactor and activator of more than 300 enzymatic reactions including glycolysis. It also helps in transporting elements such as Na, K, Ca through membrane synthesis of protein and nucleic acids. Although drinking water is not the only source of Ca and Mg in our body, they add its nutritional contribution along with the supplemental intake. The epidemiological studies in many countries reported that drinking water low in Mg is directly associated with the mortality and morbidity rate due to cardiovascular diseases. Studies concluded that intake of soft water, water low in Ca may create higher risks of bone fractures in children [42] and certain diseases related to neurons [43]. Several studies suggested low intake of these elements leads to cardiovascular disorder, tiredness, weakness or muscular cramps [37]. Lutai [37] conducted an epidemiological study in the Ust-Itim region of Russia. The study focused on physical development and morbidity rate in 7658 adults, 562 children, and 1582 pregnant women and their newborn babies. The area was divided into two different localities and one locality was supplied with water containing high minerals and another with water containing low minerals. The population of both areas did not differ in terms of food, air, and social habits. It was observed that the locality supplied with low minerals water showed a higher rate of goiter, hypertension, duodenal ulcers, chronic gastritis, heart disease, and nephritis. Children exposed to low mineral water exhibited slower physical development and more growth abnormalities. Pregnant women showed edema and anemia. Whereas, the locality supplied with high mineral content showed no such symptoms. The author concluded Such water is physiologically optimum.

4. CONCLUSION

TDS normally indicates the presence of salinity in water. Water containing no dissolved solids is intolerable and releases a flat taste to consumers. Earlier data shows water containing TDS <100 mg/l has negative impacts on human health like hyponatremia shock, metabolic acidosis, brain oedema, cardiovascular disease, chronic gastritis, goitar, etc. Also, TDS <50 mg/l is considered to be less thirst-quenching. According to reputed packaged drinking water manufacturers, minimum range between 50-100 mg/l TDS is required in drinking water. However recent data shows very less information on ill effects due to consumption of low TDS water. According to WHO 1980 Report, the minimum permissible limit required for TDS was 100 mg/l. However, recent guidelines of WHO 2017 remain silent on the minimum TDS level required in drinking water and only show the maximum permissible limits of TDS in drinking water i.e., <1000 mg/l. It can be highlighted that a minimum TDS level between 50-100 mg/l is recommended to be present in drinking water to avoid a negative impact on human health.

5. ACKNOWLEDGMENT

The authors are thankful to the DST-Women Technology Park for capacity building and entrepreneurship development (GAP 0288) and CSIR Integrated Skill Initiative (NWP 100) for the research grant.

6. REFERENCES:

1. R Islam, S M Faysal, M R Amin, F M Juliana, M J Islam, M J Alam, M N Hossain, M Asaduzzaman: Assessment of pH and total dissolved substances (TDS) in the commercially available bottled drinking water. IOSR J Nur Health Sci6(5), 35-40, 2017.
2. M. Tomar, Quality Assessment of Water and Wastewater, 1st Edition, CRC Press, 1999.
3. C S Howard: Determination of total dissolved solids in water analysis. IndEngChem Anal Ed 5(1), 4-6, 1933.
4. L T Rozelle, R L Wathen: Consumption of low TDS water. A committee report by water quality association science advisory committee, 1993. Available via https://www.wqa.org/Portals/0/Technical/Technical%20Fact%20Sheets/1993_ConsumptionOfLowTDSWater.pdf
5. A Singla, H Kundu, P Basavraj, S Singh, K Singh, S Jain: Physico-chemical and bacterial evaluation of packaged drinking water marketed in Delhi - Potential public health implications. J ClinDiagn Res 8(3), 246-250, 2014.
6. L A Semerjian: Quality assessment of various bottled waters marketed in Lebanon. Environ Monit Assess 172, 275-285, 2011.
7. S K Saha: Packaged Drinking Water - A Trivial Necessity, a Study in Kolkata, India. J Hotel Bus Manage 5(121), 1-5, 2016.
8. M. van der Aa: Classification of mineral water types and comparison with drinking water standards. EnvGeol 44, 554-563, 2003.
9. Indian standard drinking water – specification. IS 10500: 2012. Available via https://tspcb.cgg.gov.in/Environment/BIS-10500-2012-new-standards.pdf
10. J A Cotruvo: 2017 WHO Guidelines for Drinking Water Quality: First Addendum to the Fourth Edition. J Am Water Works Assoc 109(7), 44-51, 2017.
11. R C G Chidya, L Singano, I Chitedze, K A Mourad: Standards compliance and health implications of bottled water in Malawi. Int. J. Environ. Res. Public Health 16(6), 951, 2019.
12. M A Saleh, F H Abdel-Rahman, B B Woodard, S Clark, C Wallace, A Aboaba, W Zhang, J H Nance: Chemical, microbial and physical evaluation of commercial bottled waters in greater Houston area of Texas. J Environ Sci Health Part A43(4), 335-347, 2008.
13. S P Gorde, M V Jadhav: Assessment of water quality parameters: a review. IntJ Eng Res Appl3(6), 2029-2035, 2013.
14. A F Rusydi: Correlation between conductivity and total dissolved solid in various type of water: A review. IOP Conf. Ser.: Earth Environ. Sci. 118, 012019, 2018.

15. P N Patil, D V Sawant, R N Deshmukh: Physico-chemical parameters for testing of water - A review. Int J Environ Sci3(3), 1194-1207, 2012.

16. Understanding TDS and its Role in Drinking Water 2020. Available via https://www.bisleri.com/blog-detail/understanding-tds-and-its-role-in-drinking-water.

17. R K Mahajan, T P S Walia, B S Lark, Sumanjit: Analysis of physical and chemical parameters of bottled drinking water. Int J Environ Health Res 16(2), 89-98, 2006.

18. A I Airaodion, E O Airaodion, E U Osemwowa, E O Ogbuagu, U Ogbuagu: Quality Assessment of Sachet and Bottled Water in Ogbomoso Metropolis, Nigeria. Asian Food Sci J 9(2), 1-15, 2019.

19. K Y Rao, M S Anjum, P P Reddy, M Monica, I A Hameed, G V Sagar: Physico-chemical and bacterial evaluation of public and packaged drinking water in Vikarabad, Telangana, India - Potential public health implications. J ClinDiagn Res 10(5), LC01-LC07, 2016.

20. A. R. Jatoi, A. Q. Jakhrani, K. C. Mukwana, A. N. Laghari, M. M. Tunio: Study of Physicochemical Properties of Commercial Drinking Bottled Water Brands. EngTechnolApplSci Res 8(6), 3576-3579, 2018.

21. I A Akpoborie, A Ehwarimo: Quality of packaged drinking water produced in Warri Metropolis and potential implications for public health. J Environ ChemEcotoxico l4(11), 195-202, 2012.

22. A M Taiwo, A M Gbadebo, J A Awomeso: Potability assessment of selected brands of bottled water in Abeokuta, Nigeria. J ApplSci Environ Manage 14(3), 47-52, 2010.

23. M F Alam, N C Dafader, S Sultana, N Rahman, T Taheri: Physico-chemical analysis of the bottled drinking water available in the Dhaka city of Bangladesh. J Mater Environ Sci 8(6), 2076-2083, 2017.

24. EmanHussein, M Radha, Z Sabah: Quality Assessment of Various Bottled-Water and Tap-Water in Kirkuk-Iraq. Int J Eng Res Appl 4(6), 8-15, 2014.

25. J C Onweluzo, C A Akuagbazie: Assessment of the quality of bottled and sachet water sold in Nsukka town. Agro-Science 9(2), 104-110, 2010.

26. N B Khan, A N Chohan: Accuracy of bottled drinking water label content. Environ Monit Assess 166, 169-176, 2010.

27. F R Sulaiman, N F Mohd Rafi, S N Kamarudin, S. N. Syed Ismail: Assessment of physicochemical characteristics and health risk of drinking water. JurnalTeknologi 78(2), 107-114, 2016.

28. A Z Aris, R C Y Kam, A P Lim, S M Praveena: Concentration of ions in selected bottled water samples sold in Malaysia. Appl Water Sci 3, 67-75, 2013.

29. E Yilkal, F Zewge, B S Chandravanshi: Assessment of the quality of bottled water marketed in Addis Ababa, Ethiopia. Bull ChemSoc Ethiop 33(1), 21-41, 2019.

30. E O Oyelude, S Ahenkorah: Quality of sachet water and bottled water in Bolgatanga municipality of Ghana. Res J ApplSciEngTechnol, 4(9), 1094-1098, 2012.

31. I Z Mihayo, S L Mkoma: Chemical water quality of bottled drinking water brands marketed in Mwanza city, Tanzania. Res J ChemSci 2(7), 21-26, 2012.

32. S Ray, P K Roy, A Majumder: Quality of packaged drinking water in Kolkata City, India and risk to public health. Desalination Water Treat 57(59), 28734-28742, 2016.

33. N Khatri, S Tyagi, D Rawtani: Assessment of drinking water quality and its health effects in rural areas of Harij Taluka, Patan District of Northern Gujarat. Environ Claims J28(3), 223-246, 2016.

34. P Levallois, J Grondin, S Gingras: Evaluation of consumer attitudes on taste and tap water alternatives in Quebec. Water SciTechnol, 40(6), 135-139, 1999.

35. E. Mackey, J. Davis, L. Boulos, J. Brown, G. Crozes: Consumer perceptions of tap water, bottled water, and filtration devices. IWA Publishing, 2004. Available via https://books.google.co.id/books?id=nIQZiMvTwE8C&redir_esc=y&hl=id&pli=1

36. K C Verma, A S Kushwaha: Demineralization of drinking water: Is it prudent?. Med J Armed Forces India70(4), 377-379, 2014.

37. F Kozisek: ‘Health risks from drinking demineralised water’ in the book ‘Nutrients in drinking water’, pp. 148-163, 2005.

38. A W Williams: Electron microscopic changes associated with water absorption in the jejunum. Gut 4(1), 1-7, 1963.

39. K Schumann, B Elsenhans, F X Reichl, H Pfob, K H Wurster: Does intake of highly demineralized water damage the rat gastrointestinal tract?. Vet Human Toxicol 35(1), 28-31, 1993.

40. Guidelines on health aspects of water desalination. ETS/80.4. Geneva: World Health Organization, 1980.

41. Hyponatremic Seizures Among Infants Fed With Commercial Bottled Drinking water--Wisconsin, 1993, Morbidity and mortality weekly report, 43(35), 641-643. Available via https://www.cdc.gov/mmwr/PDF/wk/mm4335.pdf

42. V S Verd, S J Domingues, Q M Gonzales, M M Vidal, S A C Mariano, C C de Roque, M J M Sevilla: Association between calcium content of drinking water and fractures in children (in Spanish). AnalesEspañoles de Pediatría 37(6), 461–465, 1992.

43. H Jacqmin, D Commenges, L Letenneur, P Barberger-Gateau, J F Dartigues: Components of drinking water and risk of cognitive impairment in the elderly. Am J Epidemiol 139(1), 48-57, 1994.

Journal of Metallurgy and Materials Science, Vol. 63, No. 3-4, July-December 2021
Printed in India, © NML, ISSN 0972-4257

Conservation of Resources by Processing of Waste Dumped Iron Ore Fines

ABHISHEK KUMAR[1], AKULA SANKARA RAO[2] AND SHOBHANA DEY[1]*
[1]Mineral Processing Division, CSIR-National Metallurgical Laboratory, Jamshedpur, India
[2]Mineral Processing Division, P G Centre, Nandihalli, VSK University, Karnataka

Abstract : The dumped iron ore sample having 49.62% Fe, 6.96% SiO_2, 9.94% Al_2O_3, and 7.65% LOI was used for the present investigation. Characterization studies of the as-received sample reveal that major iron-bearing minerals present in the ore are hematite and goethite. The magnetite/ martitized magnetite is observed in minor traces. The major gangue minerals are clay and gibbsite followed by quartz.

The present study aims to enrich the iron values of dumped iron ore fines to produce a value-added product. The iron values present in the feed sample were enriched by removing silica and alumina. The deslimed feed was subjected to a Floatex Density Separator. A statistical factorial design matrix was followed for conducting the tests using the process variables as, teeter water flowrate, bed pressure, and pulp density. The underflow obtained from FDS content is 58.2% Fe and the product yield is 64.4%. For further enrichment of the Fe-grade of the U/F, it was ground to 150µm for better liberation. After desliming the ground product of U/F, Fe-grade could be improved to 60%, and further subjecting the deslimed product to magnetic separation enhances the Fe-grade to 62% with mass recovery of 44.5%. The final product produced from the dumped iron ore fines could be used for pellet feed.

Keywords: *Waste iron ore fines; Fine processing; Floatex density separator; Bed pressure; Desliming, Magnetic separation*

1. INTRODUCTION

Iron ore is the basic raw material used in the production of pig iron, sponge iron, and finished Steel. Steel being a core sector, it is integral to the growth of the economy and one of the measures for accessing development. Recently, iron ore demand has increased tremendously due to the rise in industrial applications and the global scenario for industrial development. The metallurgical requirements for iron concentrate conditions have increased, as far as the chemical composition and final concentrate stability are concerned, as the quality iron ore is not only required for stable blast furnace operation but also to enhance the efficiency of the blast furnace operation. Some of the critical issues related to iron ore which encompass the composition of the iron ore with low Fe and high Al-Si ratio, low strength, lower reducibility, low temperature softening and melting tendency needs to be addressed effectively. The exploitation of lean grade ores became necessary due to the depletion of the high-grade iron ores and the increased demands of the industry. Therefore, it becomes essential to beneficiate low-grade ores to make them amenable for blast furnace operation using appropriate mineral processing systems.

Iron ores in India are usually beneficiated simply by crushing, sizing, and washing in coarser sizes. Fines produced during crushing and grinding of the iron ores, in order to beneficiate them, are simply discarded because of low iron content, high silica, alumina content in their fine size. These fines thrown into the dumps are increasing over the years, creating a lot of environmental issues. Moreover, the increasing tonnage of these fines dumps calls for additional space to accommodate them for which a lot of land is required at or near the plant. It is imperative to utilize the low-grade ore or fines from dumps by suitable beneficiation technique to conserve the resource. It will also reduce the tonnage of waste.

The gravity separation technique is one of the economic processes, especially for iron ore fines where the density difference between the valuable and gangue minerals is more. This could be utilized for effective separation at the

Corresponding Author :
E-mail : sd@nmlindia.org

initial stage. The fines (< -1mm) could be processed by a Spiral concentrator or Floatex Density Separator (FDS). However, in a spiral concentrator, separation is affected by the combined effect of the centrifugal action with a multiple sluicing system where the surface water washes away the lighter grains, leaving the grains of heavy minerals concentrated in the deeper section of the trough. The Floatex density separator works on the principle of hinder settling. It has been used for the processing of manganese fines, chromite tailing, coal fines and other minerals [1-5]. It is an advanced hindered settling classifier, called a counter-current and autogenous teeter bed separator [6]. It makes use of differential settling rates of the particles to segregate them according to size, shape and density. It includes low cut points, previously unattainable efficiencies and short payback periods [7]. FDS can be used for the processing of the material size in the range of 800-75µm [8]. Thus, it is found to be effective for discarding the silica from the different minerals [9-10].

Keeping in view of the increasing demand of raw materials and depleting quality of the ore of the run-of mine (ROM), it is necessary to process the dumped fines. It is very important to utilize the waste as it significantly impacts mineral resources and environmental hazards. The present study highlights the interactive effects of the process variables of FDS on the processing of the dumped low-grade iron ore and its effective separation. In the investigation, an attempt has been made to process the dumped low-grade iron ore fines for its gainful utilization and to produce a value-added product for pellet making and resource conservation.

2. MATERIALS AND METHODS

2.1 Material

The raw material used for the present study was fine dumped iron ore sample of size of about 1mm and the origin is from the Eastern part of India. The sample was characterized by chemical analysis, size-wise chemical analysis, specific gravity, and mineralogical study. The chemistry of the sample studied determined by the wet conventional method is presented in Table 1. It was found that the silica and alumina content in the sample is quite high. The high LOI indicates the presence of hydrated minerals in the sample along with the silicate minerals.

Table 1: Chemical characterization of as received sample

Radical	Fe (T)	SiO_2	Al_2O_3	LOI
%	49.62	6.96	9.94	7.65

The distribution of particle size in the feed material was determined by analysing the 80% (d_{80}), 50% (d_{50}) passing sizes, and -74µm size fraction with their Fe-content and Fe distribution. The detailed mineralogical characteristic of the sample is described below.

2.1.1 Characterization

The mineralogical characterization of the as-received sample was carried out by using Orthoplan Microscope (Leica). Microscopic study reveals that hematite, goethite/ limonite and martitized magnetite are the iron-bearing minerals present in the sample. Among the iron-bearing minerals, hematite and goethite are present in major amounts, while magnetite/ martitized magnetite is noticed in very minor to traces. Hematite occurs as anhedral to subhedral-shaped grains and needle-shaped microcrystalline aggregates i.e specularite (Fig-1 A). Goethite occurs as colloform bands with alternating layers of hematite (Fig 1 C). Some of the places magnetite grains are partially or completely transformed to hematite and some unaltered remnants of magnetite are noticed within hematite grains. (Fig 1C). Clay and gibbsite are the dominant gangue minerals present in the sample followed by quartz. In places, clay is thoroughly intermixed/ intergrown with fine-grained hematite (Fig 1D). Globular inclusions of gangue minerals (gibbsite and quartz) are observed within the hematite grains (Figs. 1A &B).

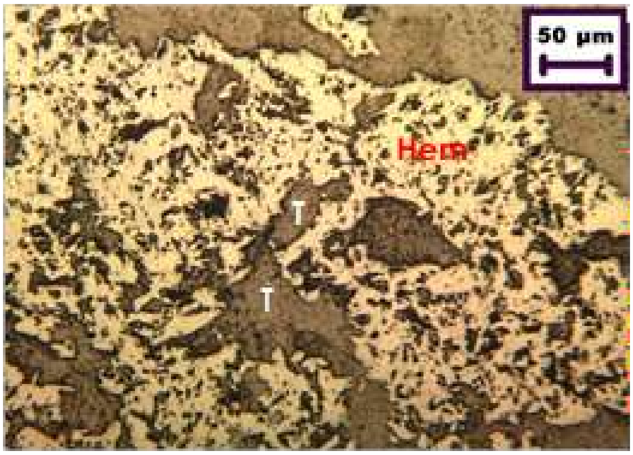

Fig 1A: hematite occurs as anhedral-shaped grains and is intricately associated with transparent gangues (clay, gibbsite & quartz).

Fig. 1B: Hematite with transparent gangues (clay, gibbsite & quartz).

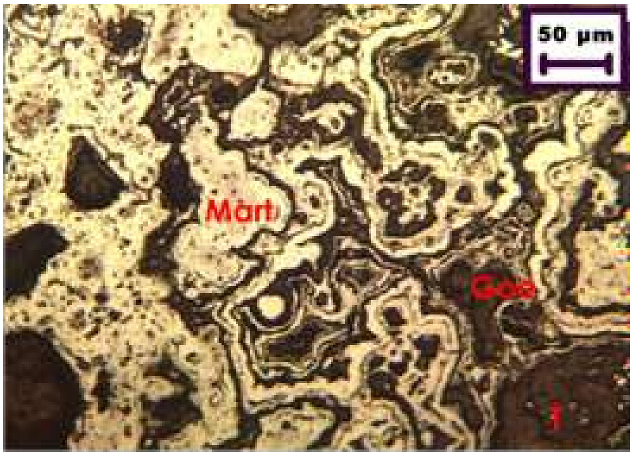

Fig 1C: Goethite occurs as colloform bands with alternating layers of hematite. Hematite replaces magnetite and remnants of unaltered magnetite found within hematite.

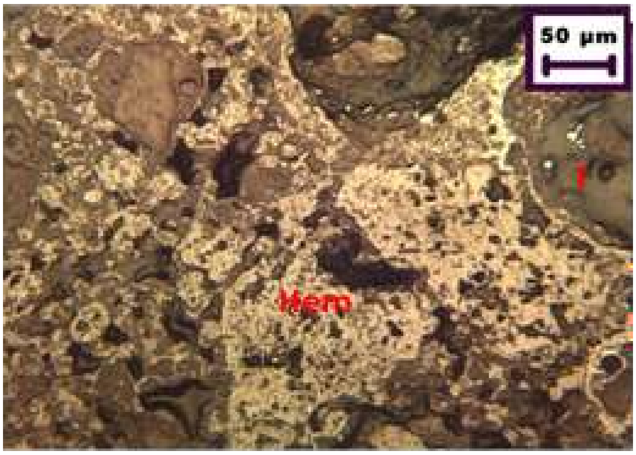

Fig 1D: Clay is thoroughly intermixed/ intergrown with fine-grained hematite.

Fig. 1: Photomicrographs showing the mineralogical characteristics and association of mineral phases present in the as-received sample. T- Transparent gangue (clay, gibbsite & quartz), Mart- Martitized magnetite, Hem- Hematite, Goe-Goethite.

2.2. Methods

The dumped iron ore fine sample was characterized with respect to the particle size distribution and each size fraction was analysed for Fe-content. Initial processing of the sample was carried out with Floatex Density Separator. In Floatex Density Separator (FDS), the three main zones as shown in Fig.2 are (i) upper zone (A) above the feed inlet (ii) intermediate zone (B) between the teeter water addition point and feed inlet, and (iii) lower section (C) below the teeter water addition point. Each zone plays a significant role in the separation of the feed based on their densities. Feed slurry is introduced to the FDS tangentially through a centralized feed well that extends to approximately one-third of the main tank length. Fluidizing (teeter water) is introduced over the entire cross-sectional area at the base of the teeter chamber through evenly spaced water distribution pipes. When the feed enters the main separation zone, it dilates into a fluidized bed by the rising current of water. The teeter water flow rate is dependent upon the particle size distribution in feed, density of the slurry, and the required cut-point for the separation. The separation takes place in zone B. The separated lighter/finer particles leave the separator through zone A and the coarser/heavier particles through zone C. The FDS provides to maintain a constant height of the teeter bed and a steady discharge of the underflow [11]. The hindered settling involved in the separation prevails the effective separation compared to the spiral concentrator.

Floatex Density Separator works on the principle of fluidization and hindered settling in which the settling rate is affected by the neighbouring particles [12]. In hindered settling, the particles settle according to their size, shape, and specific gravity whereas, in free settling, the size and shape are the only factors that affect the particle settling velocity. The settling rate of particles in hindered settling environment could be determined by Newton's law. According to Newton's law, the settling rate presented in equation (1) indicates that the settling rate decreases with the increase of the pulp density. This is attributed to the increase in the particle-particle interference and thus, the viscosity of the medium.

$$v = \left[\frac{3gd(\rho_s - \rho_f)}{\rho_f} \right]^{1/2} \qquad \text{.... (1)}$$

Where, v = settling rate of particle

d = diameter of particle, g = acceleration due to gravity

ρ_s = density of solid, ρ_f = density of fluid

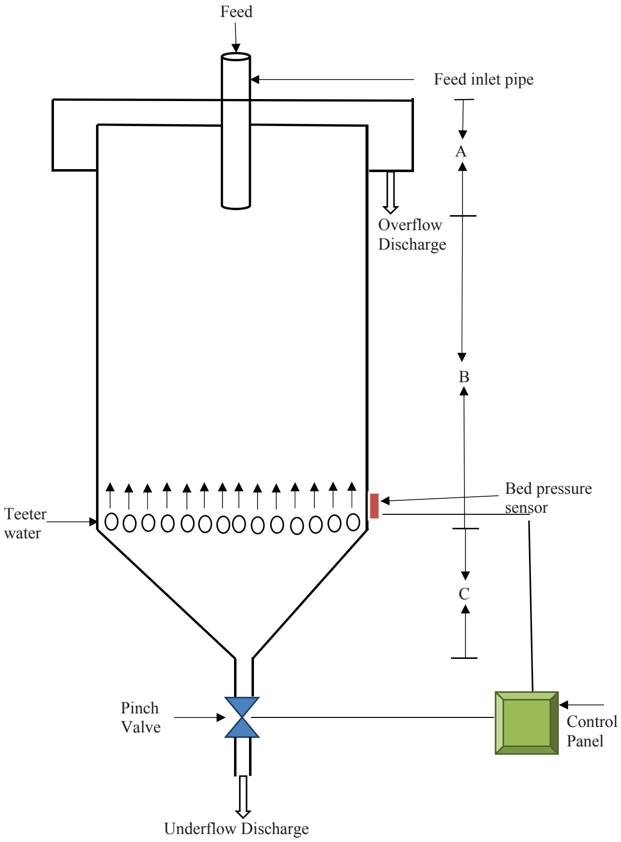

Fig.2: Schematic diagram of the set-up of Floatex Density Separator.

Processing of the as-received iron ore fines was carried out using Floatex Density Separator (Model No. LPF-0230, OUTOKUMPU). The initial stage of processing was carried out by gravity concentration as gravity separation is one of the cheapest methods of processing low-grade or waste material and no reagents are used. The FDS has a cross-section of 230 mm×230 mm, 530 mm height of the square tank and 200 mm height of the conical section at the bottom. The feed distributor was inserted inside down to 230 mm from the top.

Experiments with Floatex density separator were carried out based on the factorial design of experiments using three variables. The variable parameters like teeter water flow rate (TW) and bed pressure (BP) are the machine parameters; however, the feed rate and percent solids on the slurry (PD) refer to the material variable. Among the four parameters mentioned, the teeter water flow rate, bed pressure and slurry pulp density were considered important variables as these have a significant effect on the yield and grade of under and overflow products of FDS. The feed rate in the form of the slurry was kept constant at 300 kg/hr throughout the study. The levels of parameters are given in Table 2. Experiments were carried out under the varied levels to optimize the condition for maximizing the yield with improved Fe-content.

Table 2: Variable parameters and levels

Parameter	Units	Levels		
Teeter water flow rate (TW)	lpm	10	14	18
Bed Pressure (BP)	kPa	5	5.5	6
Pulp density (PD)	% solid	30	40	50

The teeter water flow rate was adjusted with the support of a rotameter (flow meter) and pressure or set point was calculated and set on the PID controller. When the pressure inside the column reached the set pressure, the sensor receives the signal to open the valve actuator of the pinch valve when already settled solids could be discharged as the underflow. When the pressure becomes less than the set point the valve is actuated by the sensor and is closed. This maintains the constant pressure inside the teeter column. The fine and light particles will be discharged continuously through the overflow pipe. After completion of the feeding, the pressure is reduced to drain out the already settled solids to the underflow stream. The samples collected from both the streams i.e., underflow and overflow were analysed for Fe content.

The underflow obtained from the Floatex density separator at optimized conditions was ground to -150 µm for its better liberation. The ground product was deslimed using a 2" lab model Mozley hydrocyclone keeping the diameter of the vortex finder at 14mm and apex opening at 6.5mm. The size distribution of the ground product of hydrocyclone underflow was determined. The feed inlet pressure was varied at three levels namely10 kPa, 12kPa, and 14 kPa keeping the solid concentration at 10% to obtain the best rejection of tailing (yield and grade) to the overflow. The hydrocyclone underflow was subjected to magnetic separation for further improvement of the Fe-content of the product.

3. **RESULTS AND DISCUSSION**

1.1 ***Characterization of as-received sample***

The characterization results of the as-received feed sample were presented in Figs. 3 and 4. The specific gravity of the different size fractions was determined using a pycnometer. The size distribution and Fe-grade in the fractions are indicated in Fig. 3, and the specific gravity of different size fractions is presented in Fig. 4. From Figure 3 it is found that around 20% and 50% of materials are of -160µm and -550µm size respectively. The -74µm fraction is 10.8% containing 31.4% Fe with 6.8% Fe distribution. The fraction +74µm is 89.2% by weight assaying 51.83% Fe and 93.2% Fe distribution. Fig. 4 shows that the coarser fractions have higher specific gravity than the finer fractions below 74µm. The reason is the presence of a higher amount of Fe content in the coarser fractions. Therefore, below 74µm was discarded from the feed by wet screening before subjecting for processing as the slimes contain more gangue minerals and also have a detrimental effect on the process efficiency**.** Desliming of the feed material enriched the quality of the feed material from 49.81% to 51.83% and will also enhance the efficiency of the downstream processes.

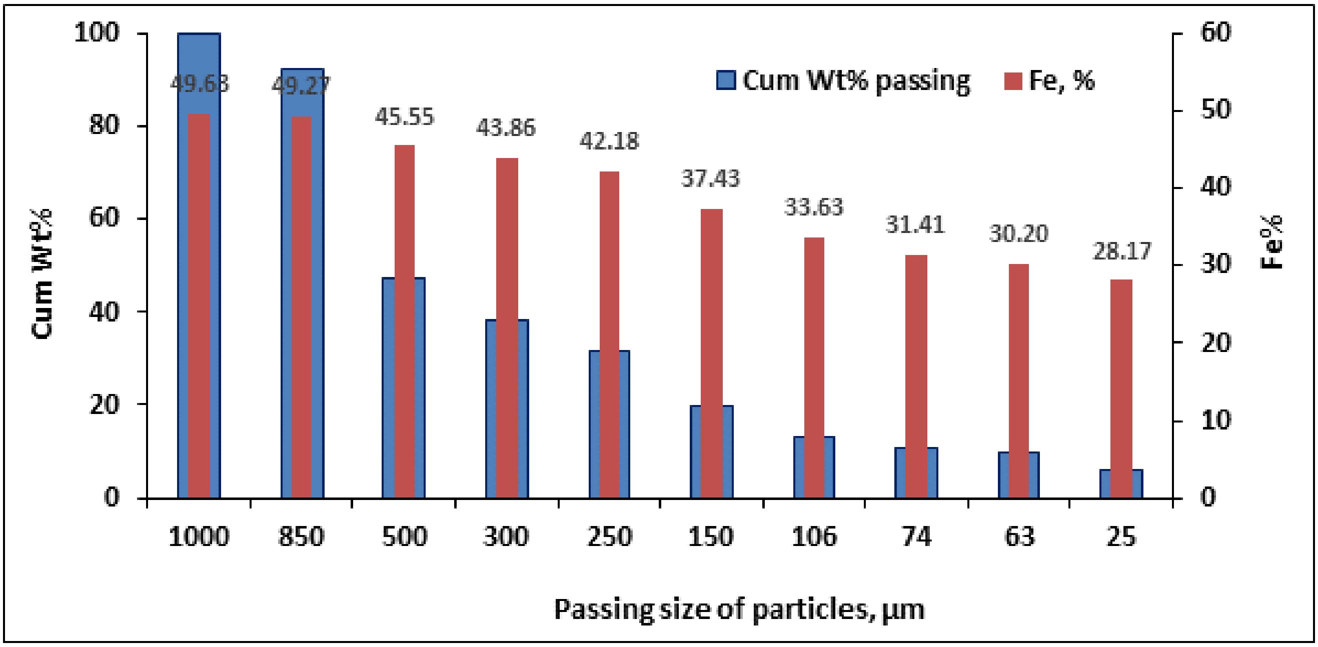

Fig 3: Particle size distribution with Fe-content of as received sample.

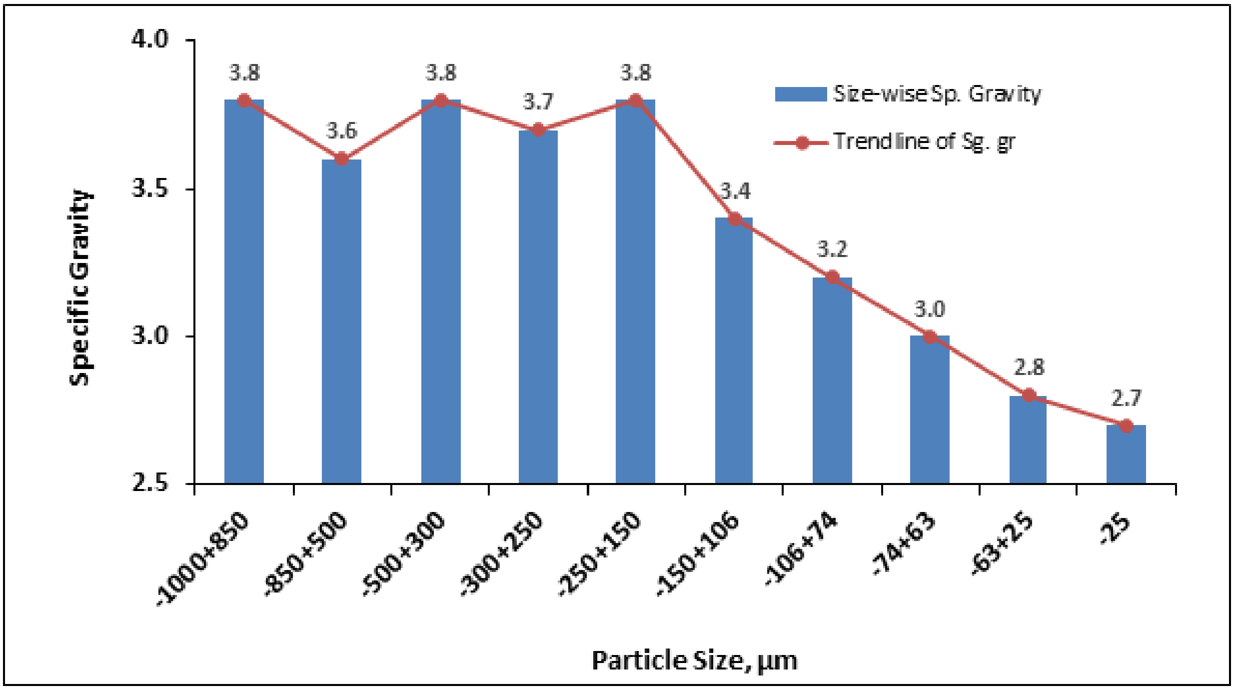

Fig.4: Size-wise density of size fractions of an as-received sample.

3.2 Floatex Density Separator

The beneficiation studies were carried out with the deslimed feed sample using a Floatex density separator based on the factorial design of experiment using three process variables at two levels (Table 2). The results obtained under the varied conditions are presented in Table 3. The effect of the process variables of FDS on the underflow and overflow products are presented in Figs. 5 and 6. The values with respect to the original feed have been indicated in the figures.

Table 3: Results of deslimed feed using Floatex Density Separator

Trial Nos.	Process Variables			Yield, %		WRO, %		Fe- Grade, %	
	Tweeter water	Bed Pressure	Pulp Density	U/F	O/F	U/F	O/F	U/F	O/F
1	10	5	30	82.7	17.3	73.8	15.4	53.5	46.4
2	18	5	30	76.3	23.7	68.1	21.1	57.4	40.4
3	10	6	30	83.2	16.8	74.2	15.0	53.9	41.4
4	18	6	30	75.3	10.7	67.2	22.0	56.7	44.7
5	10	5	50	80.2	19.8	71.5	17.7	56.0	43.1
6	18	5	50	72.2	27.8	64.4	24.8	58.2	40.0
7	10	6	50	81.6	18.4	72.8	16.4	55.1	41.2
8	18	6	50	77.7	22.3	69.3	19.9	57.0	41.1
9	14	5.5	40	81.9	18.1	73.1	16.1	55.8	43.4
10	14	5.5	40	82.7	17.3	73.8	15.4	55.8	41.3
11	14	5.5	40	83.6	16.4	74.6	14.6	55.8	41.8

3.2.1 Effect of Teeter Water flow

The role of teeter water flow is to keep the material fluidized. The effect of teeter water flow rate on the underflow yield and Fe content could be seen in Fig. 5. It was observed that within the experimental conditions, teeter water flow rate has a significant effect over the other variables. With the increase in teeter water flow rate (Trial Nos. 2,4,6 in Table 3), the yield of underflow decreases with a gradual increase in the Fe-grade (Fig. 5). Higher teeter water imposes a greater fluid drag on the particles which hinders them to settle and eventually leads more light and fine particles to the overflow resulting in less underflow yield with better Fe content [13-16]. At a higher flow rate of 18 lpm, the effect was found to be reflective and significant enrichment in Fe-content (59.6%) in the underflow was achieved with a 58.2% yield (with respect to original feed). The overflow yield is 24.8% with 40% Fe content (Fig. 6).

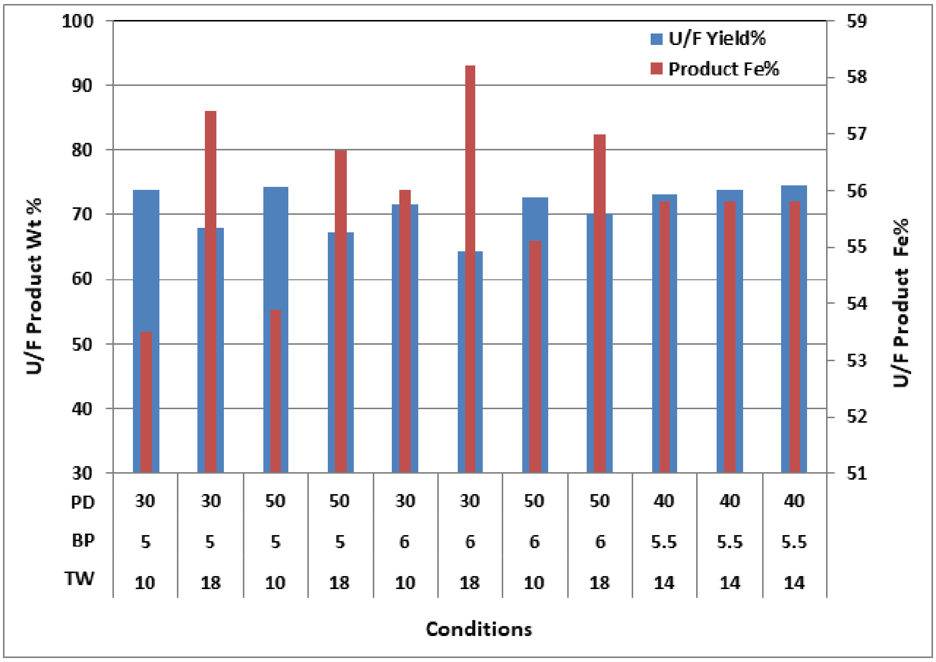

Fig. 5: Effect of variables on yield and Fe grade of Floatex underflow.

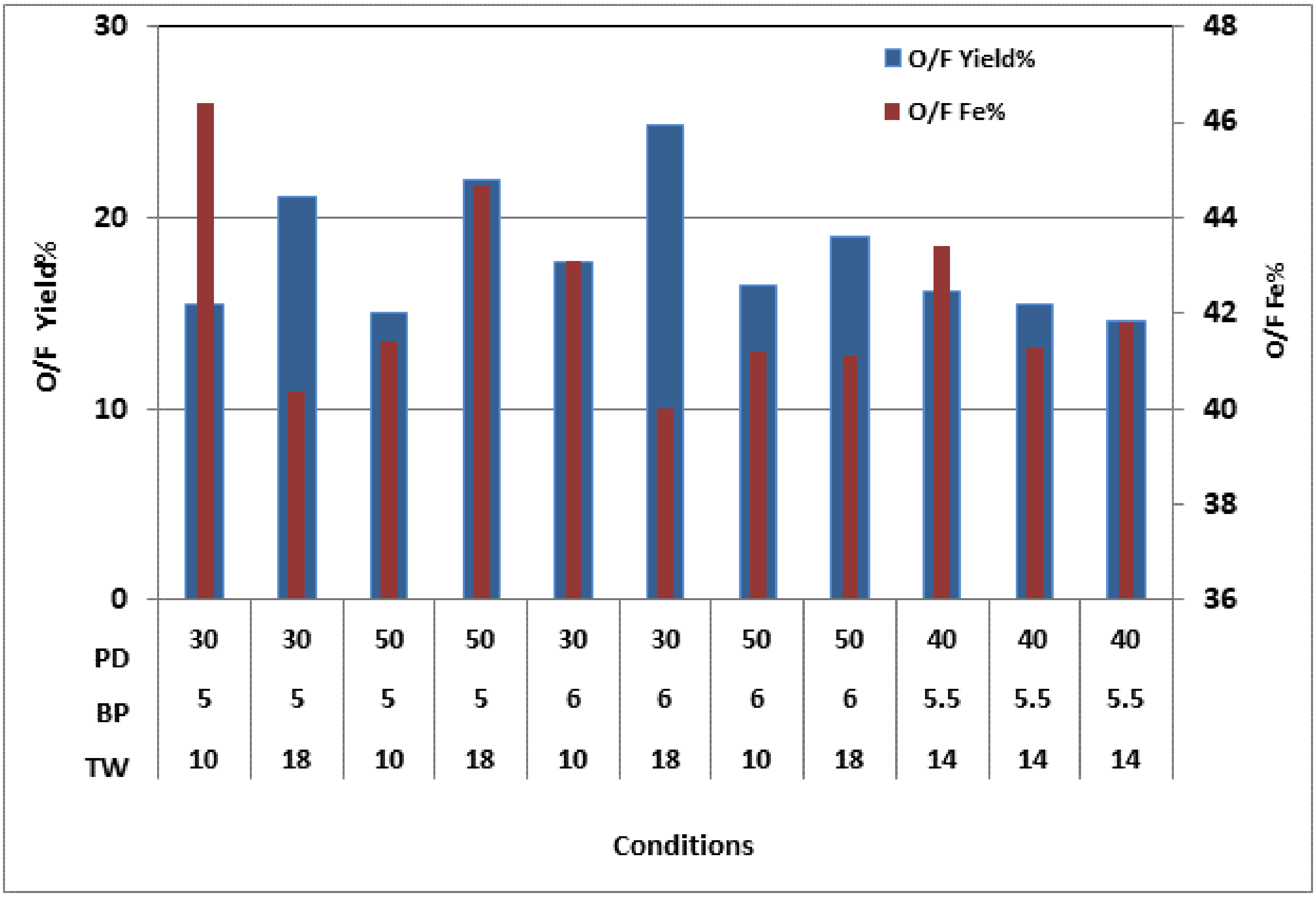

Fig. 6: Effect of variables on yield and Fe grade of Floatex overflow.

3.2.2 Effect of Bed Pressure

In the present study, the bed pressure was varied in the range of 5 to 6 kPa based on the distribution of particles in the feed. The effect of bed pressure and teeter water flow rate are inversely proportional to the responses. With increasing the bed pressure, the yield of the underflow increases with the decrease of Fe-grade (Fig. 5). Higher bed pressure results to reduce the voidage in the particle bed. Subsequently, the bed becomes more compact. As a result, increases the suspension density of the pulp and causes more rejection of the lighter particles in the overflow stream. The effect of bed pressure within the experimental variation (domain) was found to be less than the teeter water flow rate. At high bed pressure and teeter water flow rate and low pulp density (condition: BP= 6 kPa, TW=18 lpm, PD= 30%), produces an underflow yield of 64.4% with as high as 58.2% Fe-grade.

3.2.3 Effect of Pulp Density

The pulp density of the slurry defines the distribution of the feed particles. The higher the pulp density, the more is the particle-particle interaction in the slurry. It has a direct impact on the hinder settling of the particles. In the present investigation, the pulp density of the slurry was varied from 30 to 50% solid. At a higher pulp density of 50% solid, the effect of hinder settling is more and increases the effect of bed pressure, thus reducing the efficiency of the separation process. It appears from Fig. 5 and 6 that due to the more effect of teeter-water and bed pressure, the Fe-grade of the underflow product increases and yield decreases. At lower pulp density (30% solid), the rejection of lighter minerals (gangue) in the overflow is 24.8% with Fe content. Thus, a higher teeter water flow rate and low pulp density facilitate enriching the Fe content of the underflow yield.

3.3 Interaction effect of variables on responses

The results produced from the FDS based on statistical factorial design were analyzed by Design software (version 7.0) to interpret the individual and interactive effects of the process variables on the responses, like the yield of underflow and their Fe grade. The % contribution of the variables to the responses is presented in Table 4. It could be found that teeter water has more than 70% effect on the yield and Fe-content of the underflow. The regression equations generated from the ANOVA of the product (U/F) yield and Fe-grade of the yield of underflow are indicated by equations 2 and 3 respectively. The coefficients of regression equations indicate the degree of the effect. The higher the values of the coefficient, the greater the impact. It was found that teeter water (TW) and pulp density (PD) have a positive effect and the bed pressure (BP) has a negative effect on the yield of the product (U/F). The regression equation (2) shows that besides the effect of individual factors (TW, BP, PD), there is an interactive (TW-BP, TW-PD, BP-PD) effect on the product yield; however, the coefficients are not as high as the teeter water. Regression equation (3) of the Fe-grade of underflow shows that the co-efficient of the bed pressure (BP), pulp density (PD), and interaction effect of teeter water and pulp density is significant as compared to the interactive effect of the teeter water flow and bed pressure.

Table 4: Contribution of significant variables and their interaction on responses

Variables	**% Conribution**	**Effect on responses**
Response: U/F Yield		
Teeter water (TW)	74.29	Decrease
Bed pressure (BP)	2.76	Decrease
Pulp density (PD)	3.41	Increase
TW&BP	3.53	Increase
TW&PD	11.15	Increase
BP&PD	2.56	Increase
Response : U/F Fe-grade		
Teeter water (TW)	73.50	Increase
Bed pressure (BP)	7.76	Increase
Pulp density (PD)	4.59	Decrease
TW&PD	7.76	Decrease
TW&BP	1.65	Decrease

Yield of undeflow

$$= 65.35 - 5.55*TW - 1.07*BP + 1.19*PD + 1.21*TW*BP + 2.15*TW*PD + 1.03*BP*PD \quad \ldots(2)$$

Fe grade of undeflow

$$= 55.9 + 2.00*TW + 0.65*BP - 0.50*PD - 0.65*TW*PD - 0.07*TW*BP \quad \ldots.(3)$$

3.3.1 Interactive effect of teeter water and pulp density

From Table 4 and equations 2 and 3, it was found that the co-efficient of the interactive effect of pulp density and teeter water is significant on the U/F product yield and Fe-grade compared to other parameters. From Fig. 6 it is found that the yield of the overflow increases at higher teeter water flow (18 lpm) and low pulp density (30%) because the elutriating effect seems to be more at higher teeter water flow than the lower TW. As the pulp density increases the negative effect of teeter water on the yield of the underflow reduces. The combined effect of these two variables could be balanced at high pulp density and teeter water flow, and low bed pressure.

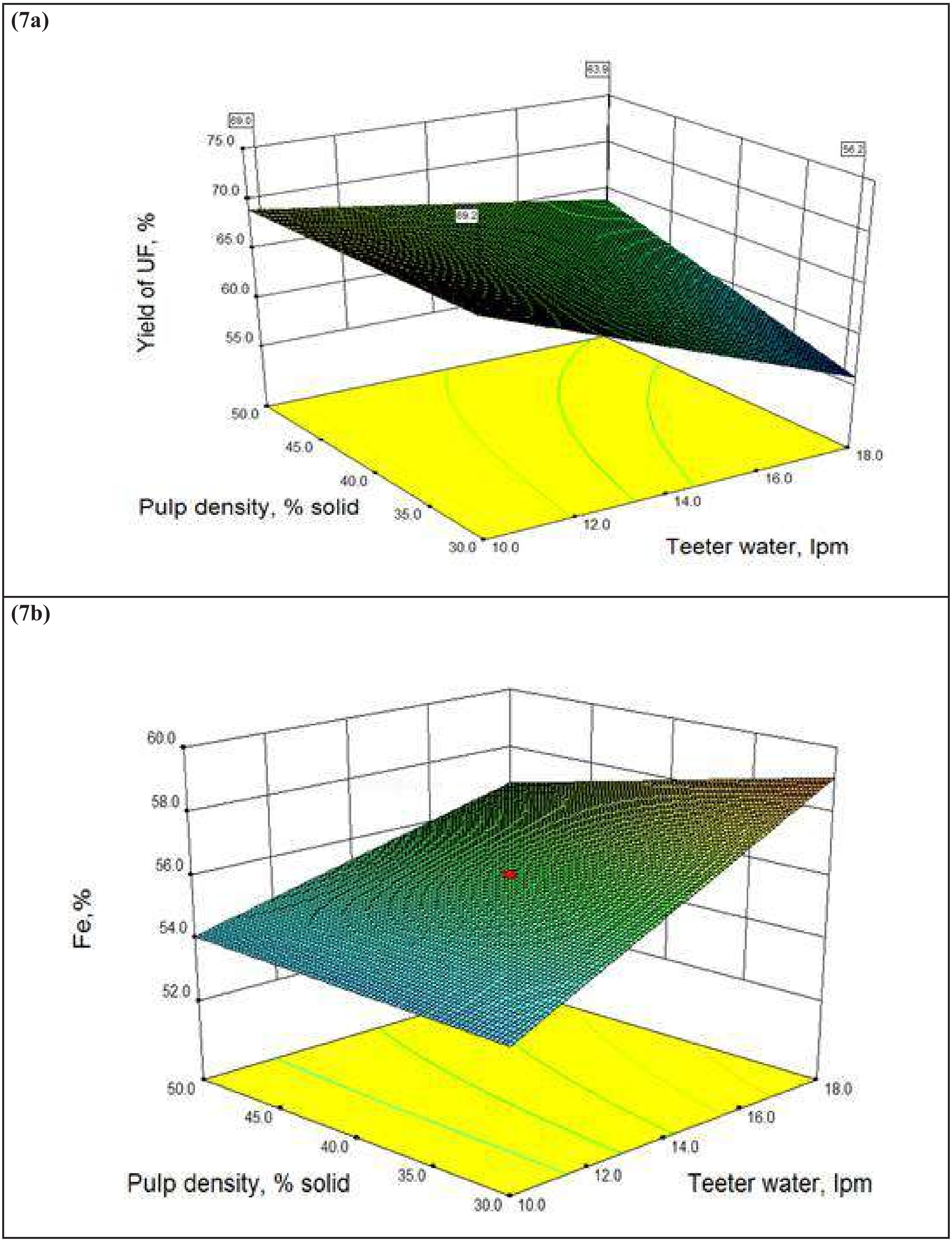

Fig. 7: Interaction effect of teeter water and pulp density on (a) underflow of FDS and (b) Fe-grade.

3.3.2 Interaction effect of teeter water and bed pressure

The interactive effect of teeter water flow rate and bed pressure is shown in Fig. 8. The role of teeter water flow rate and bed pressure on the suspension density is inversely proportional to the bed voidage. The increased teeter water flow dilates the bed and increases the viodage, whereas the bed pressure reduces the voidage and makes the bed more compact [15-16]. Thus, increased bed pressure increases the density of the medium produced during the separation. Between the two opposite effects, water flow rate has been found to be more dominating as shown in Table 4. With increasing the teeter water flow rate and bed pressure, the yield of the overflow increases. As a result, the Fe- content of the U/F increases with reduced mass. Therefore, the separation performance of FDS depend significantly on the selection of the operating conditions.

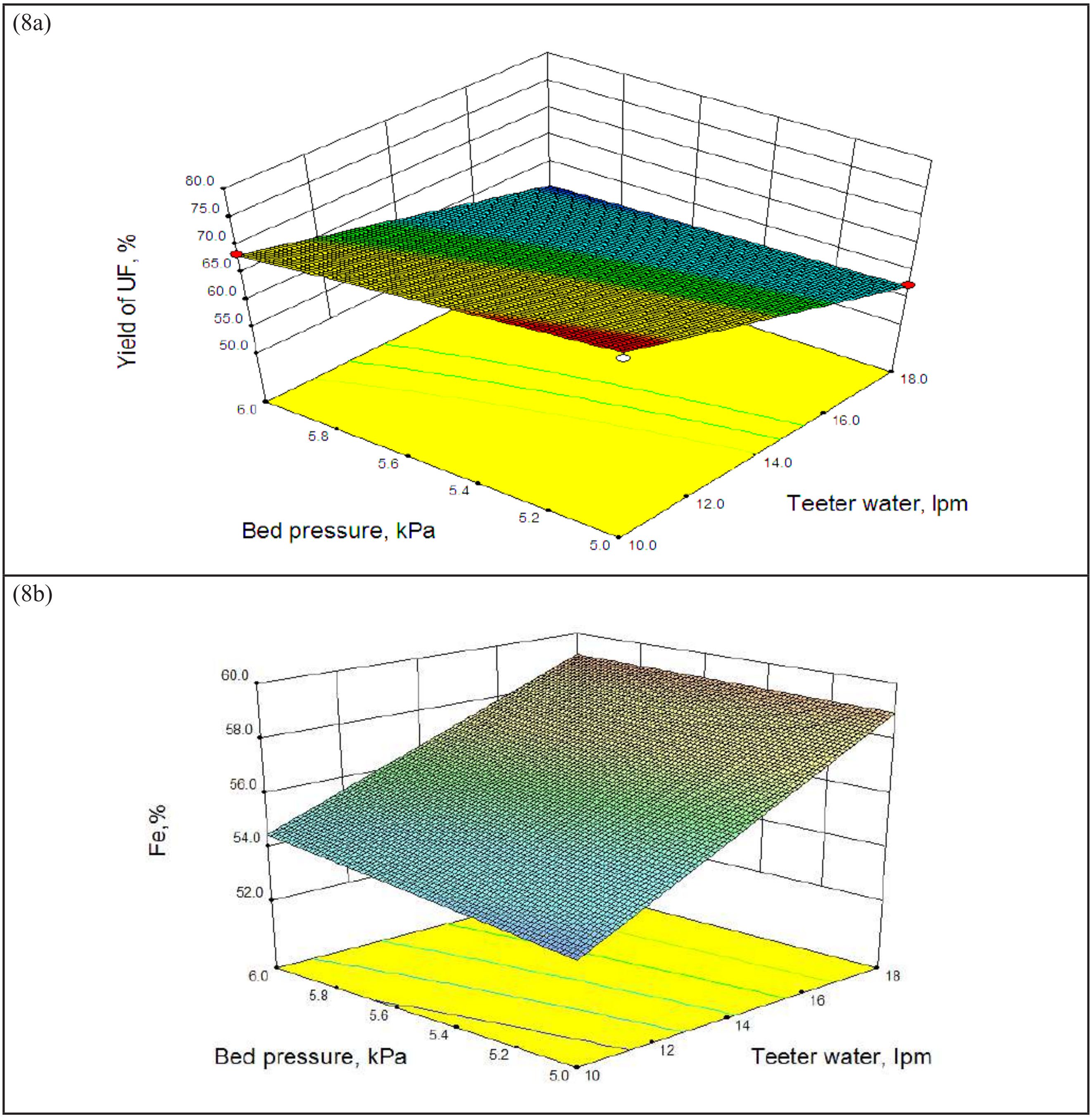

Fig.8: Interaction effect of teeter water and bed pressure on yield of (a) underflow of FDS and (b) Fe-grade of products.

3.3.3 Effect of Bed Pressure and Pulp Density

The interaction effect of bed pressure and pulp density on underflow product is shown in Fig. 9. At low bed pressure, the autogenous media could not develop and the FDS behaves like an elutriator. The fine particles are carried out of the fluidized bed by the upward flow of the fluid. The high bed pressure increases the density of the autogenous heavy media developed inside the chamber. With the increase of the pulp density increases the distribution of feed particles in the slurry; thereby increases the effect of hinder settling. With increasing the bed pressure from 5 to 6 kPa, and pulp density of 30 to 50 % solids, yield to underflow increases. The effect was found to be more dominant with the pulp density because the increase in the suspension density decreases the void density, which in turn compresses the bed. Therefore, the effective separation was found at the level of 30% PD, BP of 6kPa and teeter water flow rate of 18 lpm.

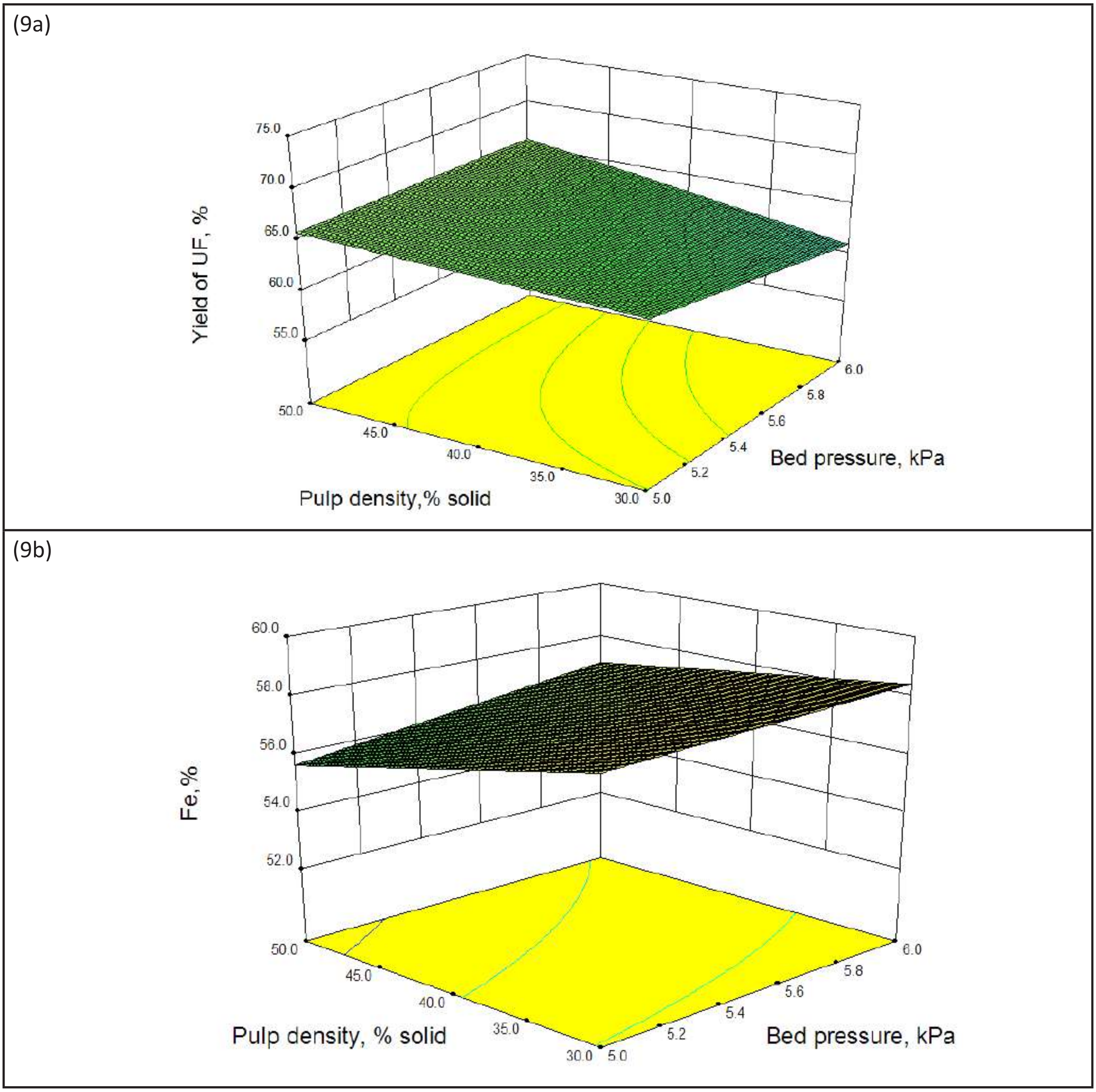

Fig.9: Interaction effect of bed pressure and pulp density on (a) underflow of FDS and (b) Fe-grade.

3.4 Processing of underflow of Floatex Density Separator

As the major iron-bearing mineral in the dumped sample was hematite, having a minor amount of martite, there is a possibility for further improvement of the quality of the product to make it useable for pellet feed. The underflow obtained from FDS was ground to -150µm. It was found from the particle size distribution (PSD) of the groundmass of underflow that the weight percent of 106µm fraction is about 54.6% and -10µm fraction is about 17.4% out of 64.7% product weight. The ultrafine particles are detrimental to the separation process, and thus, reduce the efficiency. It was discarded using hydrocyclone before subjecting to the magnetic separation for Fe enrichment. The result of desliming of -150µm ground product of FDS underflow using hydrocyclone is given in Table 5.

Table 5: Results of desliming at different pressures

Conditions	Product	Wt%	WRO	% Fe	Fe Recovery, %
10 psi VF= 14mm, Apex= 6.5mm	U/F	85.8	55.3	60.29	65.6
	O/F	14.2	9.1	44.9	8.1
12 psi VF= 14mm, Apex= 6.5mm	U/F	89.9	57.9	59.45	67.9
	O/F	10.1	6.5	45.2	5.8
14psi, VF= 14mm, Apex= 6.5mm	U/F	93.4	60.1	58.96	70.0
	O/F	6.6	4.3	44.46	3.7

The diameter of the vortex finder and apex opening was kept constant based on the earlier experience and from reported literature [17]. The effect of feed inlet pressure on the yield of the underflow and grade is shown in Fig. 10. From these figures it can be seen that yield to underflow is increasing with pressure and the grade of underflow is decreasing. This is due to the increase of the centrifugal forces generated by spin which forces the coarser particles to move towards the wall of the cyclone. The 10psi feed pressure was found to be suitable to remove the ultrafines in overflow with 44.9% Fe content as indicated in Table 5. The yield of underflow is 55.3% with respect to the original feed, with an assay value of 60.29% Fe and Fe recovery of 65.6%. This de-slimed material was used as feed for the wet high intensity magnetic separation (WHIMS).

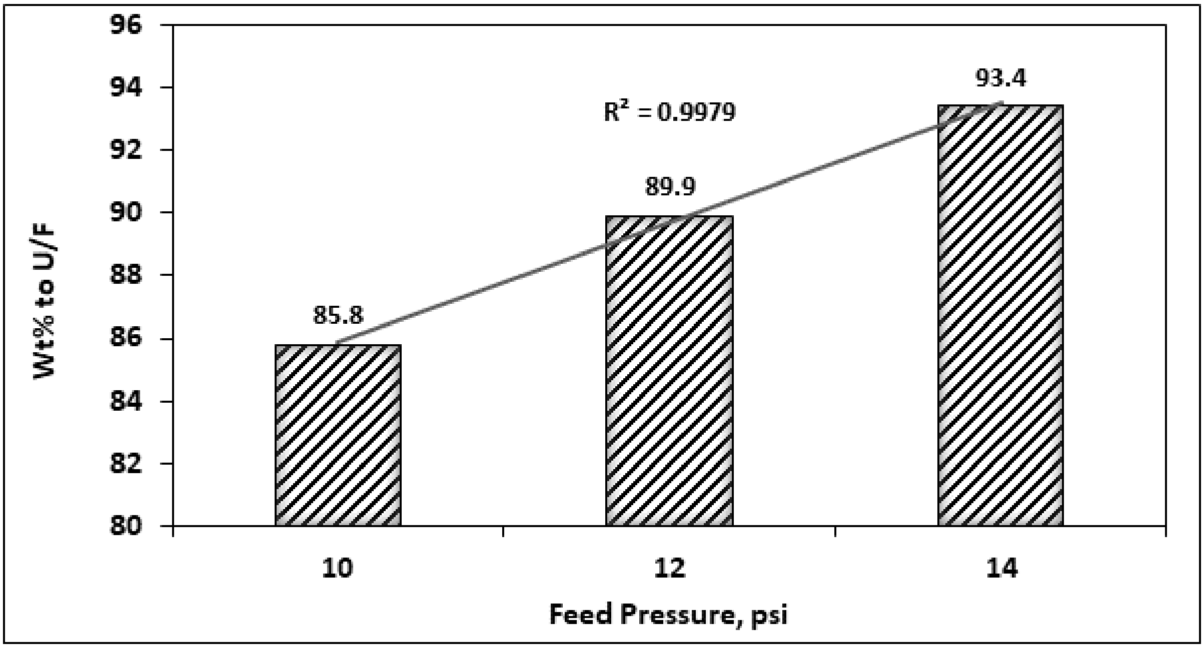

Fig.10: Effect of feed inlet pressure on underflow wt%.

3.4.1 Processing of FDS-Underflow of by WHIMS

The underflow obtained from the hydrocycloning of the ground mass of FDS-U/F having grade 60.29% Fe was fed to the high intensity magnetic separation (WHIMS). While conducting the experiments, the pulp density of 10% solid and the matrix gap of 0.5mm were kept constant. The current intensity varied from 2A to 4A. As the magnetic intensity is directly proportional to the current intensity, it changes the magnetic field intensity. The effect of magnetic intensity on the yield of concentrate and grade is shown in Fig. 11. It is observed that the yield of magnetic product was less at low magnetic field intensity as the highly susceptible (ferromagnetic) materials having high Fe-content are attracted. At high magnetic intensity, the yield of concentrate is high with a lower grade than that of concentrate at lower magnetic intensity. The condition with 3amp current (1.0 T magnetic intensity) seems to be optimum condition where the product yield is reasonable with an optimum grade of concentrate. The product weight% is 44.5% with 62.1% Fe content, and 37.8% yield with 63.4% Fe content.

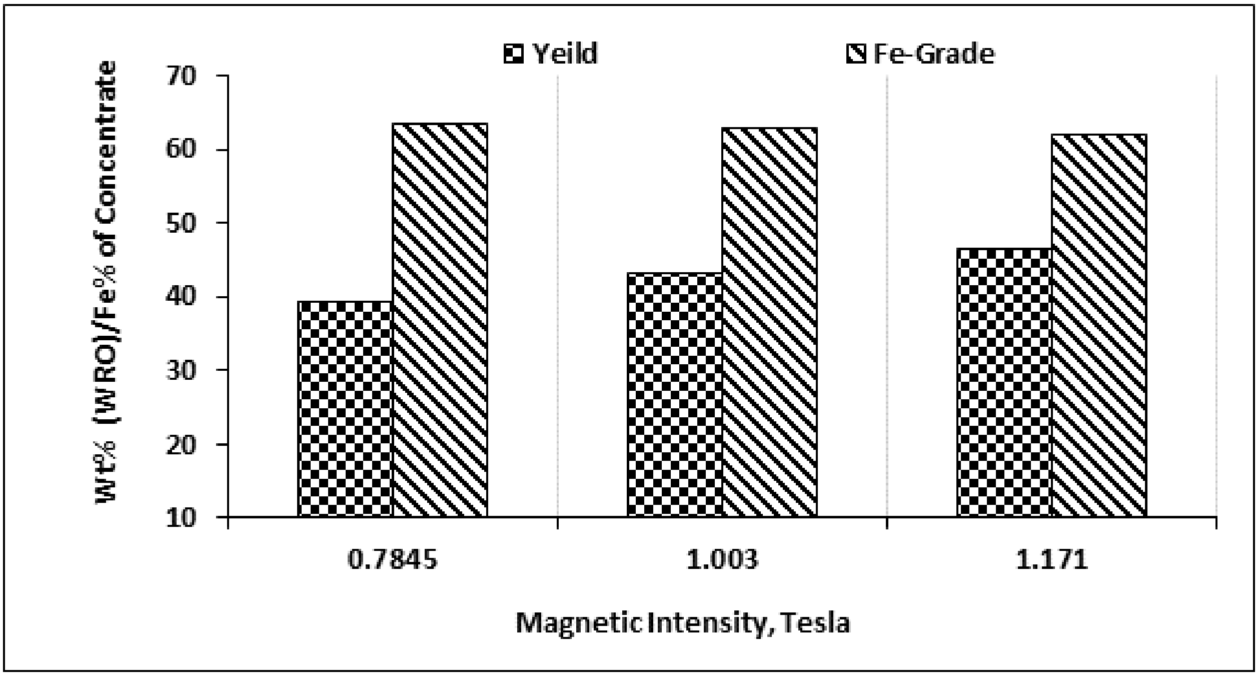

Fig.11: Effect of Magnetic intensity on concentrate yield and grade.

4. **CONCLUSIONS**

The present investigation highlights the response of the low-grade iron ore dumps having 49.62% Fe, 6.96% SiO_2, 9.94% Al_2O_3 and 7.65% LOI using a floatex density separator as a gravity concentrator at the initial stage of processing, and its metallurgical performance has been studied using a statistical design of experiments. In the sample, presence of main iron-bearing mineral phases like hematite, goethite, and a small amount of martite favours the separation efficiency of FDS. It has been found that the teeter water flow is more prevailing than the other variables like pulp density and bed pressure in the present investigation. The high teeter water flow keeps the bed suspension and moves the lighter density particles to the overflow steam as a reject. The high bed pressure of the slurry may not be effective for separation.

Because of the presence of some interlocked particles in the sample, Fe-content of the FDS underflow could be improved up to 58.2% with a yield of 64.4%. Further size reduction of the underflow product to 150µm improves the liberation of gangue minerals and subsequent hydrocycloning produces a product with an assay of 60.3% Fe with a mass of 55.3%. Further enrichment of Fe-grade by magnetic separation produces pellet grade feed. Thus, processing of dumped low grade iron ore towards the production of value-added product has an enormous impact on the environment and conservation of the resources.

ACKNOWLEDGMENTS

The authors would like to extend their sincere thanks to the Ministry of Steel for funding the research work (GAP 0224).

DECLARATION OF COMPETING INTEREST

The authors declare that they have no known competing financial interests or personal relationships that could have appeared to influence the work reported in this research article.

5. REFERENCES

1. Tripathy, S.K.; Mallick, M.K., Singh, V., Murthy, Y.R., Preliminary studies on teeter bed separator for separation of manganese fines. Powder Technol, 239, 284–289, 2013.
2. Carpenter, J.L.; Iveson, S.M.; Galvin, K.P., Ultrafine desliming using REFLUX (TM) classifier subjected to centrifugal G forces. Miner. Eng., 134, 372–380, 2019.
3. Ozcan, Ö.; Ergun, S.L., Performance of teetered bed separator for non-coal applications. Sep. Sci. Technol. 52, 1486–1495, 2017.
4. C. Raghukumar, Sunil Kumar Tripathy, S. Mohana, Beneficiation of Indian High Alumina Iron Ore Fines – A Case Study, International Journal of Mining Engineering and Mineral Processing, 1(2): 94-100, 2012.
5. Raghu Kumar, Sunil Tripathy and D.S. Rao, Characterisation and pre-concentration of chromite values from plant tailings using Floatex Density Separator, Journal of Minerals & Materials Characterization & Engineering, Vol. 8, No.5, 367-378, 2009.
6. T. Umadevi, Abhishek Kumar, A Umashanker, Rameshwar Sah & K. Marutiram (2021) Performance evaluation of a laboratory floatex density separator and its comparison with a spiral concentrator, Mineral Processing and Extractive Metallurgy, 130:2, 118-125, DOI: 10.1080/25726641, 2019.
7. Galvin, K.P., Pratten, S.J., Nicol, S.K., Dense medium separation using teetered bed separator. Minerals Engineering, 12 (9), 1069–1081, 1999.
8. Floatex Density Separator by Floatex, web link: http://www.floatex.co.uk/wp-content/uploads/2019/08/Floatex-Density-Separator.pdf**.**
9. Raghu Kumar, C., Singh, R.R., Venugopalan, O.K., Murry, V.S. and Kumar, S.S., Effect of teetering pulp density in Floatex Density separator- A Case Study' Proceedings of the International Seminar on Mineral Processing Technology - Chennai, India, 564 – 567, 2006.
10. Chandrakala K., G. K., Rao, S. Mohan and Rao, N. D., Predicting the chromite mineral upgradation in Floatex Density separator using hindered settling models' ISIJ International, Vol. 46, No. 7, 966–973, 2006.
11. Murthy, N., Basavaraj, K., Assessing the performance of a Floatex Density Separator for the recovery of Iron from low-grade Australian iron ore fines – A Case Study' XXVI International Mineral Processing Congress (IMPC), 03612-03621, 2012.
12. Xing, Y.; Gui, X.;Wang, Y.; Cao, Y.; Zhang, Y., Optimization of teetered bed separator using pulsed water. Int. J. Coal Prep. Util. 36, 283–292, 2015.
13. Zhu, X., Liu, J., Cao, Chao, Dong, Y. and Tao, W., Numerical Studies on Teeter Bed Separator for Particle Separation, Energies, 2020, 13, 2025; doi:10.3390/en13082025.
14. Ghatage, S.V., Khan, S.M.; Peng, Z., Doroodchi, E.; Moghtaderi, B., Padhiyar, N., Joshi, J.B., Evans, G.M., Mitra, S, Settling/rising of a foreign particle in solid-liquid fluidized beds: Application of dynamic mesh technique. Chem. Eng. Sci. 170, 139–153, 2017.
15. Xia, Y.K., CFD Simulation of fine particle gravity separation in hindered-settling bed separators. Chem. Prod. Process. Model, 2, 1–21, 2007.
16. Bharath N, Swapnil Urankar, Venkatesh, L K, Ramkumar, Aditya, Dua, R., Effect of particle drag on performance of a Conical Base Classifier' International Journal on Theoretical and Applied Research in Mechanical Engineering, Vol 3, Issue-3, 2014.
17. Ghatage, S.V., Sathe, M.J., Doroodchi, E., Joshi, J.B. and Evans, G.M, Effect of turbulence on particle and bubble slip velocity. Chem. Eng. Sci., 100, 120–136, 2013.
18. Yanxia Xu, Xingfu Song, Ze Sun, Bo Tang, Ping Li, Jianguo Yu, Numerical investigation of the effect of the ratio of the vortex-finder diameter to the spigot diameter on the steady-stat of the air core in a hydrocyclone, Industrial & Engineering Chemistry Research, 52(15):5470–5478, 2013.

Preparation of Manuscripts

1. Manuscripts should be sent in MS Word and pdf format.
2. Text should be 12 pt Times New Roman, double-spaced, left justified, A4 sized paper with wide margin.
3. All pages should be numbered consecutively, beginning with page 1, the title page.
4. Tables and figures should be numbered serially. Figures should have legends if applicable.
5. Tables and figures will be placed near their first mention in the text; all tables and figures must be referred to in the manuscript.
6. The following information must be included:
    - Title of the article;
    - Name(s) and initial(s) of author(s)
    - Affiliation(s) of author(s);
    - Name, address, telephone, mobile number and e-mail address of the corresponding author.
    - **Abstract:** Each article should include a brief abstract of 250 words, thatshould highlight the objectives, methods, results, and conclusions of the paper.
    - **Keywords:** To identify the subjects under which the article may be indexed, 6-10 key words should be provided.
    - **References:** In the text, references to the literature should be presented within square bracket indicating the reference number [1]
    - **Paper:**

      [1] J. Singh, A. Kumar: Investigation of structural, morphological and electrochemical properties of mesoporous La_2CuCoO_6 rods fabricated by facile hydrothermal route. Int. J. Miner. Metall. Mater. 27: 987–995, 2020
    - **Book:**

      [2] J.D. Verhoeven: Fundamentals of physical metallurgy, 1st Edition, New York: Wiley, New York, pp. 55-61, 1975
    - **Online document**

      [3] Cory Mitchell: Fractal Indicator Definition and Applications. Technical analysis basic education. Available via https://www.investopedia.com/terms/f/fractal.asp, Retrieved 3 August 2020
    - **Illustrations :** These include photographs, drawings and line art includes graphs, flowcharts, diagrams etcwhich can be reproduced without losing any clarity. Figure legends or captions should follow the order in which they appear in the manuscript, be numbered with Arabic numerals and should not contain a text repeated. The preferred file formats for images and line art are TIF/TIFF and JPG. For good image quality, scanned black & white photographs should be provided as 300 ppi TIFF files and line art should be provided as 600 ppi TIFF files.
    - **Color Figures :** The authors should accept the obligation of bearing the expenses of colour images in the printed version of the journal while no charge is required for their appearance in the electronic version of the journal. Colour illustrations should be provided as scanned TIFF files at a minimum of 300 ppi with a 24-bit colour depth.
    - **Mathematical Equations :** Mathematical equations, suitably numbered, should be inserted in the text through "Equation editor" of MS word as per the example

$$P(e) = \frac{1}{2}\left[1 - erf\left(\frac{K}{2\sqrt{2}}\right)\right]$$

    - Symbols, Abbreviations, Units, etc.: It is mandatory to define the symbols and acronyms at first mention within the text and also in titles and abstracts. The authors are requested to follow internationally accepted rules for nomenclature, abbreviations, symbols and units.
    - **Computer Code:** Pseudo algorithms, as presented below, with appropriate reference should be submitted.

```
❖ Title  : To compute power spectral density and corresponding frequency
  Input  : Time domain data X(t)
  Output : P
  ■ Read the signal X(t)
  ■ Crop the signal and get the length N
  ■ Supply sampling frequency, $f_s$
  ■ Do fast Fourier transformation of the signal
        Xk = fft(X(1:N), $f_s$);
  ■ Compute power spectral density and corresponding frequency by
        P = Xk.*conj(Xk) / N;
        f = fs*(1:$f_s$)/N;
```

NML PUBLICATIONS

CSIR-National Metallurgical Laboratory (NML) has recently published the following Scientific & Technical books. The year of publication and the price fixed has been shown in the parenthesis respectively. The request for procurement of publication is to be made to the Director, CSIR-National Metallurgical Laboratory, Jamshedpur - 831 007, India (e-mail : director@nmlindia.org) along with the Bank Draft in Favour of Director, NML Jamshedpur, payable at State Bank of India, NML Branch (Code No. 3329) Jamshedpur, India.

1. ***Electronic Waste*** (Eds. R. Singh, A. Das, K.K. Bhattacharyya and N.G. Goswami)	(2010)	(Rs. 950/-, US $100)
2. ***Remaining Life Assessment of Aged Components in Thermal Power Plants and Petrochemical Industries*** (Eds. A.K. Ray, S. Chaudhuri, N.G. Goswami and R.N. Ghosh)	(2008)	(Rs. 950/-, US $100)
3. ***Agglomeration and Charaterization of Iron Bearing Raw Materials*** (Eds. D. Bandyopadhyay, M.C. Goswami, N.G. Goswami and G.K. Mandal)	(2008)	(Rs. 800/-, US $100)
4. ***Extraction of Non-ferrous Metals and their Recycling*** (Eds. R.K. Jana, Abhilash and N.G. Goswami)	(2008)	(Rs. 800/-, US $100)
5. ***Proceedings of the National Workshop on Coal Processing in Hindi*** (Eds. : R. Singh, R.P. Bhagat, (Eds. : R. Singh, R.P. Bhagat, Avimanyu Das, K.K. Bhattacharyya, P.N. Mishra and N.G. Goswami)	(2007)	(Rs. 700/-, US $90)
6. ***Processing of Iron ore*** (Eds. R. Singh, Avimanyu Das and N.G. Goswami)	(2007)	(Rs. 800/-, US $100)
7. ***Special Metal Casting and Forming Processes*** (Eds. K.L. Sahoo, G.K. Mandal, N.G. Goswami and Sukomal Ghosh)	(2007)	(Rs. 800/-, US $100)
8. ***Advanced Gravity Sepration*** (Eds. : R. Singh, A. Das and N.G. Goswami)	(2007)	(Rs. 600/-, US$ 70)
9. ***Synergy of R&D and Marketing*** (Eds. : P.N. Chaudhury, N.V. Satyanarayana, A.Seshu Kumar & N.G. Goswami)	(2003)	(Rs. 800/-, US$ 100)
10. ***Metallurgy in India - A retrospective*** (Eds. : P. Ramachandra Rao and N.G. Goswami)	(2001)	(Rs. 1500/-, US$110)
11. ***Recent Trends in Structural Integrity Assessment*** (Eds. : V.R. Ranaganath, S. Tarafder and Aruna Bahadur)	(2001)	(Rs. 850/-, US$ 100)
12. ***Processing of Fines*** (Eds. : P. Bhattacaryya, R. Singh & N.G. Goswami)	(2000)	(Rs. 1200/-, US$ 115)
13. ***Non Ferrous Metals and Materials*** (Eds. : D.M. Chakrabarti, R.K. Jana, V. Kumar B.D. Pandey & N.G. Goswami)	(2000)	(Rs. 700/-, US$ 100)
14. ***Non Ferrous Extractive Metallurgy in the New Millennium*** (Eds. : P. Ramachandra Rao, Rakesh Kumar, S. Srikanth & N.G. Goswami)	(1999)	(Rs. 1200/-, US$ 115)
15. ***Environmental & Waste Management in Iron & Steel Industries*** (Eds. : A. Bandopadhyay, N.G. Goswami & P. Ramachandra Rao)	(1999)	(Rs. 800/-, US$ 100)
16. ***Fly Ash Utilisation for Value Added Products*** (Eds. : B. Chatterjee, K.K. Singh & N.G. Goswami)	(1999)	(Rs. 600/-, US$ 80)
17. ***Materials Characterization Techniques — Principles and Applications*** (Eds. : G. Sridhar, S. Ghosh Chowdhury & N.G. Goswami)	(1999)	(Rs. 1000/-, US$ 110)
18. ***Environmental & Waste Management in Non-Ferrous Industries*** (Eds. : A. Bandopadhyay, N.G. Goswami & P. Ramachandra Rao)	(1998)	(Rs. 700/-, US$ 100)
19. ***Modern Methods of Chemical Analysis for Minerals, Metals Refractory Materials & Environmental Pollutants*** (Eds. : S.C. Srivastava, K.K. Padhi, L.P. Pandey & N.G. Goswami)	(1998)	(Rs. 300/-, US$ 30)
20. ***Composite Materials*** (Eds. : R.R. Bhat, S. Ghosh & C.S.S. Krishnan)	(1998)	(Rs. 500/-, US$ 70)
21. ***Nondestructive Evaluation of Materials*** (Eds. : A. Mitra, N. Parida, D.K. Bhattacharya & (N.G. Goswami)	(1997)	(Rs. 800/-, US$ 100)
22. ***Ferro-Alloys Industreis in the Liberalised Economy*** (Eds. : A.K. Vaish, S.D. Singh, N.G. Goswami & P. Ramachandra Rao)	(1997)	(Rs. 600/-, US$ 80)
23. ***Processing of Fines*** (Eds. : P. Bhattacaryya, R. Singh, K.V. Rao and N.G. Goswami)	(1997)	(Rs. 1000/-, US$ 110)
24. ***Failure Analysis*** (Eds. : S.R. Singh, N. Parida, D.K. Bhattacharya & N.G. Goswami)	(1997)	(Rs. 800/-, US$ 100)
25. ***Computer Applications in Materials & Metallurgical Engineering*** (Eds. : R.N. Ghosh, S. Tarafder & N.G. Goswami)	(1996)	(Rs. 700/-, US$ 100)
26. ***Transport Phenomena in Metallurgical Processes*** (Eds. : S. Prakash & P. Ramachandra Rao)	(1996)	(Rs. 850/-, US$ 100)
27. ***Environmental & Waste Management in Metallugical Industries*** (Eds. : A. Bandopadhyay, N.G. Goswami & P. Ramachandra Rao)	(1996)	(Rs. 700/-, US$ 100)
28. ***Modern Methods of Chemical Analysis for Minerals, Metals, Refractory Materials & Ferro-alloys*** (Eds. : S.C. Srivastava, L.P. Pandey & N.G. Goswami)	(1996)	(Rs. 650/-, US$ 70)
29. ***Boiler Corrosion*** (Eds. : I. Chattoraj, I. Singh, S.K. Narang, D.D.N. Singh & N.G. Goswami)	(1995)	(Rs. 500/-, US$ 70)
30. ***Alternative Charge Materials for Electric Arc & Induction Furnaces*** (Eds. K.N. Gupta, K.K. Mishra, K.K. Singh, A.K. Vaish, S.D. Singh, D. Bandopadhyay & N.G. Goswami)	(1994)	(Rs. 500/-, US$ 70)

ISSN 0974-1267 (Online)
ISSN 0972-4257 (Print)

Published by
CSIR-National Metallurgical Laboratory
Jamshedpur - 831007, Jharkhand, India
www.nmlindia.org